TU Delft

Delft University of Technology

Document Version
Final published version

Citation (APA)
Yuan, Y. (2026). *In Search of Closure: Multiple Scattering Mechanisms in Synthetic Aperture Radar Interferometry*. [Dissertation (TU Delft), Delft University of Technology]. https://doi.org/10.4233/uuid:8d7bdda5-b9dc-49e3-adc1-81f4fb1ba610

Important note
To cite this publication, please use the final published version (if applicable).
Please check the document version above.

Copyright
In case the licence states “Dutch Copyright Act (Article 25fa)”, this publication was made available Green Open Access via the TU Delft Institutional Repository pursuant to Dutch Copyright Act (Article 25fa, the Taverne amendment). This provision does not affect copyright ownership.
Unless copyright is transferred by contract or statute, it remains with the copyright holder.

Sharing and reuse
Other than for strictly personal use, it is not permitted to download, forward or distribute the text or part of it, without the consent of the author(s) and/or copyright holder(s), unless the work is under an open content license such as Creative Commons.

Takedown policy
Please contact us and provide details if you believe this document breaches copyrights.
We will remove access to the work immediately and investigate your claim.

This work is downloaded from Delft University of Technology.

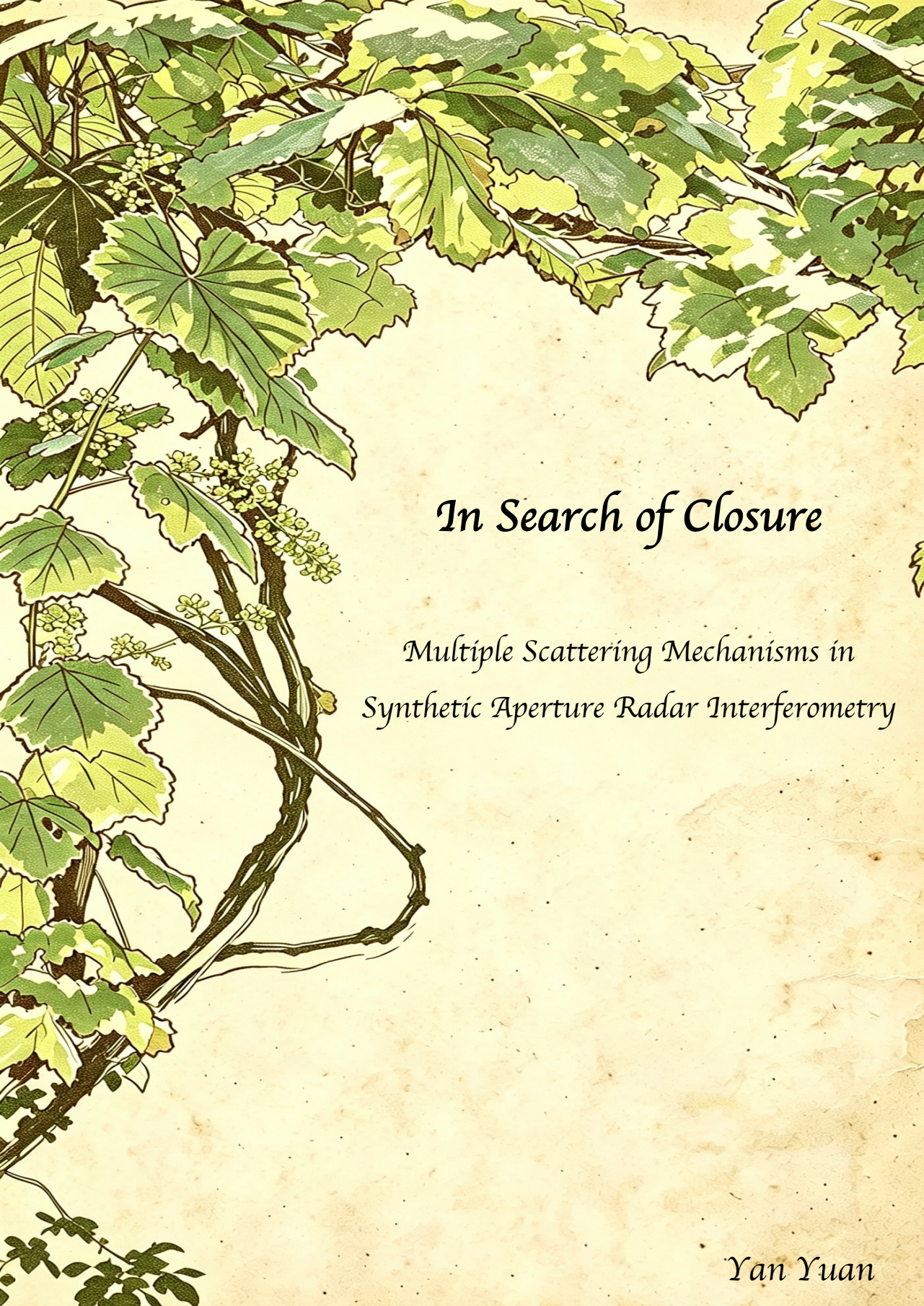

In Search of Closure

Multiple Scattering Mechanisms in Synthetic Aperture Radar Interferometry

Yan Yuan

IN SEARCH OF CLOSURE

MULTIPLE SCATTERING MECHANISMS IN SYNTHETIC APERTURE RADAR INTERFEROMETRY

IN SEARCH OF CLOSURE

MULTIPLE SCATTERING MECHANISMS IN SYNTHETIC APERTURE RADAR INTERFEROMETRY

Dissertation

for the purpose of obtaining the degree of doctor
at Delft University of Technology,
by the authority of the Rector Magnificus,
Prof. dr. ir. H. Bijl,
chair of the Board for Doctorates,
to be defended publicly on
Friday 25 September 2026 at 12:30

by

Yan YUAN

This dissertation has been approved by the promotors.

Composition of the doctoral committee:

Rector Magnificus,	chairperson
Prof. dr. ir. F. Lopez Dekker,	Delft University of Technology, *promotor*
Prof. dr. ir. R.F. Hanssen,	Delft University of Technology, *promotor*
Independent members:	
Prof. dr. ir. S.C. Steele-Dunne,	Delft University of Technology
Prof. dr. A. Hooper,	University of Leeds, UK
Prof. dr. J.M. López-Sanchez,	Universidad de Alicante, Spain
Prof. dr. L.M.H. Ulander,	Chalmers University of Technology, Sweden
Dr. F. De Zan,	delta phi remote sensing GmbH, Germany
Prof. dr. ir. H.W.J. Russchenberg,	Delft University of Technology, reserve member

Keywords: Synthetic aperture radar, synthetic aperture radar interferometry, repeat-pass interferometry, interferometric synthetic aperture radar closure phases, statistics, modelling

Printed by: Ridderprint

Cover design: Yan Yuan, Songlin Li

Copyright © 2026 by Y. Yuan

ISBN 978-94-6518-437-1

An electronic version of this dissertation is available at
http://repository.tudelft.nl/.

十年饮冰, 难凉热血

Decades of drinking ice, yet the passion remains unextinguished.

— 梁启超 (Liang Qichao)

CONTENTS

Summary xi

Samenvatting xiii

1 Introduction 1
- 1.1 Motivation . . . 1
- 1.2 Background . . . 2
- 1.3 Research questions . . . 2
- 1.4 Dissertation outline . . . 3

2 From SAR to InSAR closure phases 5
- 2.1 Synthetic Aperture Radar . . . 5
  - 2.1.1 Frequencies . . . 6
  - 2.1.2 Resolution . . . 8
  - 2.1.3 Measurements . . . 9
  - 2.1.4 Speckle . . . 10
- 2.2 SAR interferometry . . . 10
  - 2.2.1 Configurations . . . 11
  - 2.2.2 Processing . . . 11
  - 2.2.3 Measurements . . . 14
  - 2.2.4 Height of ambiguity . . . 15
- 2.3 InSAR closure phase . . . 15
  - 2.3.1 Non-zero closure phases . . . 16
  - 2.3.2 Noise-induced closure phases . . . 17
  - 2.3.3 Geophysical closure phases . . . 18
  - 2.3.4 Modeling . . . 19

3 Data and Processing 23
- 3.1 Research area . . . 23
- 3.2 Data . . . 23
  - 3.2.1 Sentinel-1 data . . . 24
  - 3.2.2 Geophysical data . . . 25
- 3.3 Adaptive multilooking . . . 27
  - 3.3.1 Mathematical representation of re-multilooking . . . 28
  - 3.3.2 Classification . . . 29
  - 3.3.3 Multilooking . . . 30
  - 3.3.4 Geophysical labeling . . . 30

3.4 Significance test . . . 30
3.4.1 Equivalent number of looks . . . 30
3.4.2 Numerical model . . . 31
3.4.3 Significance ratio . . . 34

4 Closure phases and their significance **37**
4.1 Closure phase examples and their significance . . . 37
4.2 Seasonal mean closure phases . . . 39
4.3 Spatiotemporal mean closure phases . . . 41

5 Explainable closure phases **45**
5.1 Correlation analysis between closure phase observations and known mechanisms . . . 45
5.1.1 Soil moisture variation induced closure phases . . . 46
5.1.2 Volume scattering induced closure phases . . . 50
5.2 Variance in closure phases . . . 54
5.2.1 Explainable variance . . . 54
5.2.2 Unexplained variance . . . 56

6 Vegetation dynamics related closure phases **61**
6.1 Research area . . . 61
6.2 Data . . . 62
6.3 Data processing . . . 64
6.4 Observations . . . 65
6.4.1 Observations over corn fields . . . 65
6.4.2 Observations over citrus fields . . . 66
6.4.3 Observations over greenhouses . . . 67
6.4.4 Discussion . . . 68
6.5 Existing models verification . . . 69
6.5.1 Existing soil moisture model . . . 69
6.5.2 Existing interferometric model for volume scattering . . . 70
6.6 Vegetation growth model . . . 70
6.6.1 Equivalent-medium propagation model . . . 71
6.6.2 Skewed motion model . . . 75
6.7 A composite model . . . 79
6.7.1 Backscatter representation using a water cloud model . . . 81
6.7.2 Generalized simulation under simplifications . . . 82
6.7.3 No decorrelation case . . . 83
6.7.4 Effect of decorrelation . . . 86
6.7.5 Discussion . . . 88

7 Conclusions and recommendations **89**
7.1 Conclusions . . . 89
7.2 Contributions . . . 92
7.3 Recommendations . . . 92

Acknowledgements **95**

Bibliography **99**

List of Publications **105**

SUMMARY

The concept of closure phases is introduced in Interferometric Synthetic Aperture Radar (InSAR) as a circular summation of three multilooked interferometric phases. Since the beginning of InSAR theory, the interferometric phase is considered conservative, in other words, the expected value of the interferometric phases is redundant, given their circular summation, the closure phase, is equal to zero. In the 2010s, approximately two decades after the widely recognized crucial role of InSAR technique in monitoring Earth's surface change, real data examples showing non-zero closure phases are reported. The wide existence of non-zero closure phases challenges the validity of the implicit phase consistency assumption, and thus fosters extensive discussion within the InSAR community regarding its origin, where the main debate lies in whether there is a geophysical signal within the quantity or it is purely phase noise. Not long after the first report of the non-zero closure phases, following up research clearly points out the non-zero quantity stems from a combination of phase noise and geophysical signal. The evident existence of geophysical components in closure phases stimulates the development of new InSAR stack processing strategies to minimize their effect in estimating geometric changes. Meanwhile, researchers started exploring the possible application of this new quantity could offer, and main efforts have been devoted in building interferometric soil moisture models and retrieving soil moisture from interferometric phases.

Since the coexistence of a geophysical component and phase noise is acknowledged, predicting the contribution of the phase noise and subsequently quantifying the significance of the geophysical closure phase help justify its non-negligibility and assess the feasibility of further investigating the underlying scattering mechanisms. Following this rationale, this research begins by characterizing the significance of closure phases through a statistical approach. The analysis is conducted over a large spatiotemporal scale using Sentinel-1 acquisitions, thereby providing a general perspective on the prevalence of significant closure phases.

With the aid of the current analytical understanding of the geophysical origins of closure phases, soil moisture variations, and volumetric scattering in combination with perpendicular baselines, we investigate the correlation between closure phases and these geophysical factors. Combined with the statistical significance, this approach allows us to quantify the explainable variance in the observations. The results indicate that a substantial portion of the observed signals remains unexplained by existing models, highlighting the limitations of current knowledge in explaining the observed signals.

The correlation between the unexplained variance in the observed closure phase and land use provides additional insights into their potential physical origins, particularly the high correlation with agriculture fields. This finding motivates a focused investigation into the geophysical closure phases related to vegetation. To this end, we selected croplands in southern Spain to examine vegetation-induced closure phases by qualitatively comparing Sentinel-1 observations with vegetation parameters, such as crop cal-

endar and Leaf Area Index (LAI). The analysis reveals a clear signal associated with vegetation development. We proposed two models: one accounting for variations in vegetation water content and another considering line-of-sight (LoS) motion introduced by vegetation growth. Both models offer plausible explanations for the observed signatures and extend the analytical understanding of the individual scattering mechanisms contributing to geophysical closure phases. Building on these insights, we develop a composite model to integrate as many known mechanisms as possible, including soil moisture variations, ground surface scattering, and vegetation water content changes. Although the model predictions demonstrate an improved understanding and provide a partial analytical representation of the relevant processes, we remain in search of closure regarding the origins of geophysical closure phases. Future physical modeling efforts should therefore aim to capture the coupled effects arising from multiple scattering mechanisms.

Overall, this dissertation presents the prevalence of statistically significant closure phases, quantifies the extent to which the observed signals can be explained by current knowledge, identifies clear closure phase signatures associated with vegetation development, provides analytical representations of vegetation-related scattering mechanisms, integrates known processes within a composite analytical framework, and highlights that the coupled effects of multiple scattering mechanisms should be considered in future studies.

SAMENVATTING

Het concept van sluitfasen (closure phases) wordt in Interferometric Synthetic Aperture Radar (InSAR) geïntroduceerd als een circulaire sommatie van drie gemultilookte interferometrische fasen. Sinds het begin van de InSAR-theorie wordt de interferometrische fase als conservatief beschouwd; met andere woorden, de verwachtingswaarde van de interferometrische fasen is redundant, aangezien hun circulaire sommatie, de sluitfase, gelijk is aan nul. In de jaren 10, ongeveer twee decennia nadat de cruciale rol van de InSAR-techniek bij het monitoren van veranderingen aan het aardoppervlak algemeen werd erkend, werden voorbeelden uit echte data gerapporteerd waarin niet-nul sluitfasen werden waargenomen. Het wijdverbreide voorkomen van niet-nul sluitfasen stelt de geldigheid van de impliciete aanname van faseconsistentie ter discussie en leidt daarmee tot uitgebreide discussie binnen de InSAR-gemeenschap over de oorsprong ervan, waarbij het belangrijkste debat zich richt op de vraag of de grootheid een geofysisch signaal bevat of uitsluitend uit fasenruis bestaat. Niet lang na de eerste rapportage van niet-nul sluitfasen wees vervolgonderzoek duidelijk uit dat de niet-nul waardes voortkomen uit een combinatie van fasenruis en een geofysisch signaal. Het duidelijke bestaan van geofysische componenten in sluitfasen stimuleerde de ontwikkeling van nieuwe InSAR-stackverwerkingsstrategieën om hun effect bij het schatten van geometrische veranderingen te minimaliseren. Tegelijkertijd begonnen onderzoekers de mogelijke toepassingen van deze nieuwe grootheid te verkennen, waarbij de belangrijkste inspanningen waren gericht op het opstellen van interferometrische bodemvochtmodellen en het afleiden van bodemvocht uit interferometrische fasen.

Sinds het naast elkaar bestaan van een geofysische component en fasenruis is erkend, helpt het voorspellen van de bijdrage van de fasenruis en het vervolgens kwantificeren van de significantie van de geofysische sluitfase om de niet-verwaarloosbaarheid ervan te onderbouwen en de haalbaarheid van verder onderzoek naar de onderliggende verstrooiingsmechanismen te beoordelen. Vanuit deze redenering begint dit onderzoek met het karakteriseren van de significantie van sluitfasen door middel van een statistische benadering. De analyse wordt uitgevoerd op grote ruimtelijke en temporele schaal met behulp van Sentinel-1-acquisities, waarmee een algemeen beeld wordt verkregen van het voorkomen van significante sluitfasen.

Met behulp van het huidige analytische inzicht in de geofysische oorsprong van sluitfasen, bodemvochtvariaties en volumetrische verstrooiing in combinatie met loodrechte basislijnen, onderzoeken we de correlatie tussen sluitfasen en deze geofysische factoren. In combinatie met de statistische significantie stelt deze benadering ons in staat om de verklaarbare variantie in de waarnemingen te kwantificeren. De resultaten laten zien dat een aanzienlijk deel van de waargenomen signalen niet kan worden verklaard door bestaande modellen, wat de beperkingen van de huidige kennis bij het verklaren van de waargenomen signalen benadrukt.

De correlatie tussen de onverklaarde variantie in de waargenomen sluitfase en het

landgebruik biedt aanvullende inzichten in de mogelijke fysische oorsprong ervan, met name de sterke correlatie met landbouwpercelen. Deze bevinding motiveert een gerichte studie naar de geofysische sluitfasen die verband houden met vegetatie. Hiervoor selecteerden we akkerland in Zuid-Spanje om door vegetatie geïnduceerde sluitfasen te onderzoeken door Sentinel-1-waarnemingen kwalitatief te vergelijken met vegetatieparameters, zoals de gewaskalender en de Leaf Area Index (LAI). De analyse onthult een duidelijk signaal dat verband houdt met de ontwikkeling van vegetatie. We stelden twee modellen voor: één dat rekening houdt met variaties in het watergehalte van de vegetatie en één dat rekening houdt met beweging in de zichtlijn (line-of-sight, LoS) die door vegetatiegroei wordt geïntroduceerd. Beide modellen bieden plausibele verklaringen voor de waargenomen kenmerken en breiden het analytische inzicht in de individuele verstrooiingsmechanismen die bijdragen aan geofysische sluitfasen uit. Voortbouwend op deze inzichten ontwikkelen we een samengesteld model om zoveel mogelijk bekende mechanismen te integreren, waaronder variaties in bodemvocht, verstrooiing aan het grondoppervlak en veranderingen in het watergehalte van de vegetatie. Hoewel de modelvoorspellingen een verbeterd begrip laten zien en een gedeeltelijke analytische representatie van de relevante processen bieden, zijn we nog steeds op zoek naar een sluitende verklaring voor de oorsprong van geofysische sluitfasen. Toekomstige fysische modelleringsinspanningen zouden zich daarom moeten richten op het beschrijven van de gekoppelde effecten die voortkomen uit meerdere verstrooiingsmechanismen.

Dit proefschrift laat het voorkomen van statistisch significante sluitfasen zien, kwantificeert het de mate waarin de waargenomen signalen kunnen worden verklaard door de huidige kennis, identificeert duidelijke sluitfasesignaturen die verband houden met de ontwikkeling van vegetatie, biedt analytische representaties van vegetatiegerelateerde verstrooiingsmechanismen, integreert bekende processen binnen een samengesteld analytisch raamwerk, en benadrukt dat de gekoppelde effecten van meerdere verstrooiingsmechanismen in toekomstige studies moeten worden meegenomen.

1

INTRODUCTION

1.1. MOTIVATION

Synthetic Aperture Radar (SAR) interferometry (InSAR) has been widely recognized as one of the most important technologies for monitoring Earth's surface changes. Its applications span a broad range of research domains, including topographic mapping, natural hazard monitoring (e.g., landslides and earthquakes), volcano surveillance, detection of subsidence and investigation of uplift caused by groundwater or oil extraction, and analysis of glacier dynamics. A key assumption underlying the use of InSAR technique is phase consistency, which, in this context, is based on a geometric interpretation of the interferometric phase, such as differential range delays associated with topography, surface motion or atmospheric propagation, and systematic phase errors introduced by radar or processing. Under this assumption, the expected values of three interferometric phases are redundant, given that their sum, the closure phase, is equal to zero. However, closure phases, constructed from the circular summation of three multilooked interferometric phases, frequently deviate from zero. These non-conservative closure phases challenge the validity of the implicit phase consistency assumption. Current literature indicates that phase noise, together with multiple geophysical variations, jointly contribute to the occurrence of non-zero closure phases. While the contribution of phase noise can be quantified through numerical simulation, the geophysical component remains largely unexplored. A better understanding of the scattering mechanisms associated with these geophysical variations will improve the accuracy of InSAR applications, such as deformation analysis, by enabling their explicit treatment in SAR stack processing. In addition, a comprehensive understanding of geophysical origins of closure phases could lead to novel approaches for exploring Earth's surface and subsurface dynamics, complementing traditional radar observables like backscatter and interferometric coherence.

1

1.2. BACKGROUND

Recent studies have presented numerous real data examples of non-zero closure phases. Because such non-conservative closure phases challenge the long-standing assumption of phase consistency in InSAR, they have prompted extensive discussion within the community about their origins [1–8] and stimulated the development of strategies to mitigate their impact on InSAR applications, such as deformation time series analysis [5, 9, 10]. Nevertheless, despite these efforts, substantial knowledge gaps concerning non-zero closure phases persist. Regarding their geophysical origins, non-zero closure phases have been attributed to variations in the dielectric properties of the medium, volume scattering in combination with perpendicular baseline, and asymmetric differential motion, in which the displacements of scatterers within a resolution cell are unevenly distributed [1, 2, 6, 8]. Among the proposed geophysical origins, only two models have been developed, each addressing the contributions of soil moisture variation and volume scattering, respectively. In efforts to mitigate non-zero closure phases' effects on the geometric interpretation of interferometric phases over distributed areas, most strategies have been developed without a thorough understanding of the underlying scattering mechanisms. Therefore, the nature of non-zero closure phases remains largely unexplored, hindering the possibility of fully exploiting interferometric phases and limiting the opportunities they may offer for future Earth observation technologies.

1.3. RESEARCH QUESTIONS

This dissertation is designed to address existing research gaps and contribute to a more comprehensive understanding of the origins of closure phases. Specifically, we focus on three main aspects. First, most previous investigations have been limited to local scales, and a comprehensive, systematic statistical characterization of closure phases across broader spatial and temporal scales remains lacking. Second, the processes responsible for non-zero closure phases remain poorly understood, and a quantitative understanding of the relative contributions of each known mechanism is necessary. Third, in terms of modeling closure phases, significant efforts have been devoted to understanding their relationship with soil moisture variations, while other contributing physical processes remain largely unexplored [2, 4, 6–8, 11, 12]. Accordingly, we frame the research questions as follows to address each of the aspects:

Question 1: *How prevalent are statistically significant non-zero closure phases?*

Assessing the statistical significance of observed closure phases helps to confirm the presence of a geophysical component beyond phase noise, particularly when conducting systematic analyses over large spatiotemporal scales. Analyzing data over a large spatial scale ensures coverage of diverse geophysical conditions, while a long temporal scale analysis captures the dynamic variations in the observed signals. Ideally, we aim to separate the phase noise contribution from the observations. Since this is practically challenging, we address this question by quantitatively evaluating phase noise through Monte Carlo numerical simulations. The confirmation of widespread non-zero closure phases of geophysical origin has two key implications: first, they represent a signal that can be exploited, and, second, a factor that must be accounted for when interpreting deformation signals.

Question 2: *To what extent do current models explain the observed closure phases?*

Quantifying the explainable signals within current understanding across large spatiotemporal scales provides insights into the extent to which existing models can account for the observed signals under different geophysical conditions. At the same time, assessing the unexplained signals and examining how their proportion varies spatiotemporally can help reveal the limitations of current models and anticipate possible sources of these signals. To address this research question, we quantify the explainable signals by assessing the correlation between observed closure phases and geophysical variables, which can be translated into closure phases using existing analytical models.

Question 3: *What are possible explanations for the unexplained signals in closure phases?*

Examining the signatures of closure phase observations in regions exhibiting a high proportion of unexplained variance provides insights into additional mechanisms that are not fully captured by current models. To address this research question, we investigate the spatiotemporal behavior of the observed closure phase signals in these regions, qualitatively interpret them using geophysical measurements, and analytically relate their signatures to geophysical variations not yet accounted for in existing models.

These three research questions are sequentially related and are therefore addressed individually in this dissertation, with specific analyses conducted to answer each one.

1.4. DISSERTATION OUTLINE

In this dissertation, we examine closure phases at multiple scales to investigate their statistical properties and to explore the origins of the unexplained signals they contain. In Chapter 2, we begin with a concise overview of radar observables from the fundamentals of SAR to the concept of InSAR closure phase. Chapter 3 then details the selected datasets and the processing steps undertaken to reveal and interpret the closure phase signatures. For the large-scale study, we focus on the statistical behavior of closure phases, demonstrate the widespread presence of geophysical components, examine their characteristics under various environmental conditions, and explore interpretations for signals that are not taken into account by existing models. In Chapter 4, we systematically elaborate the statistical significance of closure phases by analyzing their spatiotemporal patterns in a broad area. In Chapter 5, we apply established analytical models that account for soil moisture variations and volume scattering mechanisms [1, 2, 11] to quantify the portion of closure phases that can be explained, while also highlighting residual signals that are not yet captured by current models. These large-scale analyses provide a foundational understanding that motivates a more detailed investigation at the local scale, aimed at uncovering the underlying mechanisms that contribute to geophysical closure phases. In Chapter 6, we focus on vegetated regions that exhibit substantial deviations from conservative closure phases and develop models to interpret the observed signals. Additionally, by incorporating existing soil moisture and surface scattering models, we construct a composite model that accounts for contributions from vegetation growth, ground surface scattering, and soil moisture variations. Lastly, in Chapter 7, we conclude the work and give recommendations on future study.

2

FROM SAR TO INSAR CLOSURE PHASES

2.1. SYNTHETIC APERTURE RADAR

Synthetic aperture radar (SAR) is an imaging technique that provides high resolution observations regardless of weather conditions. A SAR system enables fine-resolution imaging by mounting a radar with a partially side-looking geometry on a moving platform, such as an aircraft or spacecraft, where the platform motion is exploited to synthesize a large aperture. Compared to airborne SAR, satellite-based SAR provides a more effective solution for large-scale and long-term Earth observations, primarily due to its global coverage, geometric stability, and long-term data availability [13]. The geometry of a satellite-based side-looking SAR system is illustrated in Figure 2.1. As the platform moves in the azimuth direction, the relative position of the radar antenna with respect to the target changes over time. The radar transmits radio pulses at a high pulse repetition frequency, such that each target is successively illuminated and the corresponding echoes are recorded. The successive echo waveforms received at different antenna positions are coherently detected, stored, and processed to form the synthetic aperture. Phase information in the returned echoes, together with time-delay information, is then used to generate a high-resolution image of the illuminated surface [14].

Figure 2.2 presents a comparison between a Sentinel-2 optical image and a Sentinel-1 SAR image, both acquired over Qingdao, China, on December 8, 2019, illustrating the differences in surface representation between optical and radar imaging techniques. Although the images were not acquired at the exact same time, the comparison clearly demonstrates the all-weather capability of SAR, as clouds that obscure much of the optical image are entirely absent from the SAR image. Additionally, bright regions in the SAR image highlight urban areas, which are less distinguishable in the optical image due to limited contrast. Furthermore, the SAR image exhibits bright targets over the water surface, corresponding to ships, owing to their strong microwave reflections. Although the optical images are often heavily affected by atmospheric conditions, they provide

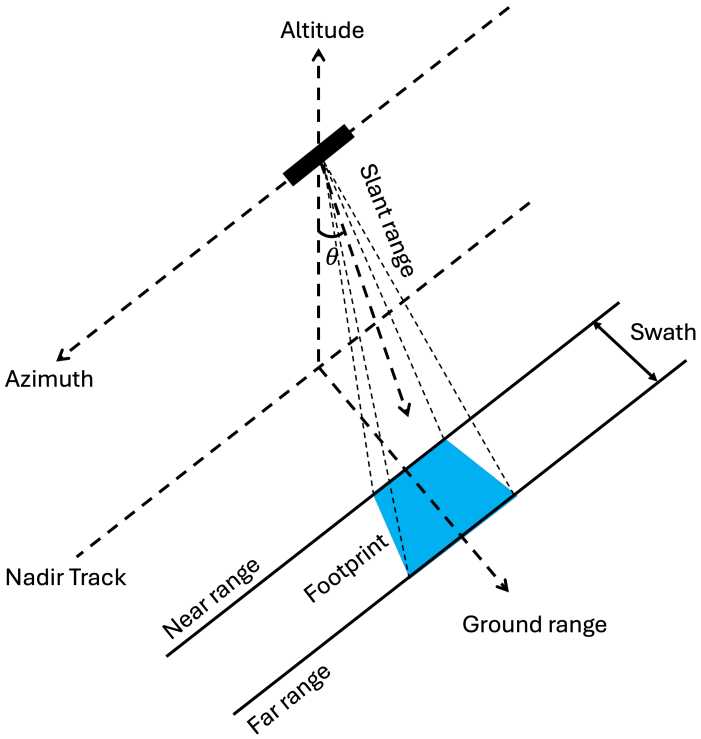

Figure 2.1: Geometry of SAR mounted on a spacecraft.

intuitive information that directly relates to geophysical phenomena. For example, the Leaf Area Index (LAI), which characterizes canopy structure, can be derived from rectified reflectances [15] and is used in this project as a geophysical dataset to aid in the interpretation of SAR observables.

2.1.1. FREQUENCIES

Earth observation SAR system commonly operates within a frequency range of 0.3 GHz to 12 GHz, corresponding to wavelengths from 1 m to 8 mm. Longer-wavelength SAR systems can penetrate clouds and provide all-weather imaging. However, as the wavelength decreases, the system becomes more sensitive to atmospheric scattering, and the signals can be significantly attenuated by clouds and precipitation [16, 17]. The different wavelengths of SAR are categorized into bands with letter designations, as summarized in Table 2.1. Depending on their physical properties, radar bands differ in how they interact with surfaces and how deeply they penetrate various media, making each band suitable for specific applications.

Among the various SAR frequency bands, X-band satellite missions, such TerraSAR-X, provide high-resolution imaging of the Earth's surface even under cloudy conditions with little or no precipitation [17]. Since X-band has a low penetration into vegetation,

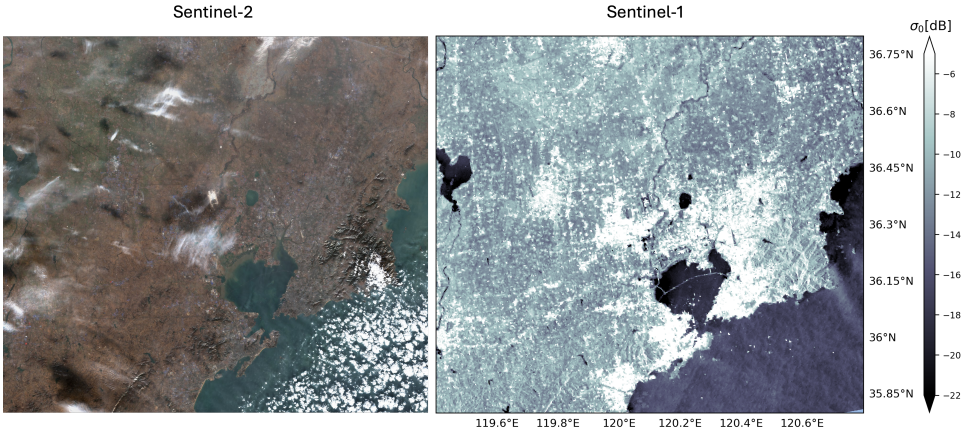

Figure 2.2: Sentinel-2 optical image vs co-polarized (VV) 300 m resolution Sentinel-1 radar backscatter over Qingdao, China on December 8, 2019.

it can be used for land-use mapping and monitoring of canopy structure. In this dissertation, we use Sentinel-1 C-band observations, which provide the systematic acquisitions and data availability required. C-band SAR has a low to moderate penetration into vegetation and subsurface. Due to additional scattering effects, the layer of returned C-band signal from the target scene is less well-determined. It is widely used for mapping applications and for change detection over land, ice and ocean. The use of S-band for Earth observation has increased with missions such as NISAR. Its lower frequency allows to penetrate through clouds and light vegetation canopies, therefore, extending C-band applications to areas with higher vegetation density. The first spaceborne SAR satellite, Seasat, was an L-band system [18]. With a wavelength of about 23 cm, L-band signals penetrate deeply through vegetation and soil, interacting with large brunches and tree trunks. This penetration capability enables the use L-band SAR to measure surface deformation in vegetated terrain, assess soil moisture, and distinguish crop types. The recently launched Biomass mission carries a P-band SAR to map global forest aboveground biomass [19]. Owing to its low frequency, P-band offers high penetration capability through vegetation and ground cover, making it particularly suitable for applications such as biomass mapping, subsurface imaging, and archaeological surveys.

A comparison of co-polarized (VV) SAR backscatter observations, denoted as σ_0, acquired at different frequencies over the same location in the Black Forest, Germany and at the same hour, is shown in Figure 2.3. On the left is the Sentinel-1 C-band observation, σ_0, on the right is the SAOCOM-1 L-band observation, shown as $\sigma_0 + 5$ for visualization purpose. The C-band image appears brighter, indicating stronger backscatter but also a higher noise level. The long wavelength of L-band interacts more with the internal structure of vegetation, allowing for a clearer distinction between forests and cropland. However, the C-band radar primarily captures signals from the canopy layer, making it more difficult to differentiate between dense forests and agricultural fields. This comparison highlights the frequency-dependent sensitivity of SAR backscatter to vegetation

Table 2.1: SAR bands.

Band	Frequency	Wavelength	Applications
X	8 - 12 GHz	3.8 - 2.4 cm	High resolution land use monitoring.
C	4 - 8 GHz	7.5 - 3.8 cm	Global mapping, change detection over land, ice, and ocean.
S	2 - 4 GHz	15 - 7.5 cm	Increasing use for SAR-based Earth observation and agriculture monitoring.
L	1 - 2 GHz	30 - 15 cm	Geophysical monitoring, biomass mapping, deformation monitoring, soil moisture detection.
P	0.3 - 1 GHz	100 - 30 cm	Biomass mapping and archaeology surveys.

characteristics.

2.1.2. RESOLUTION

The spatial resolution of the radar defines the minimum separation between distinguishable measurements. The actual sensor resolution has two dimensions, range resolution and azimuth resolution. In slant range direction, the resolution is given by the inverse of pulse bandwidth B_p as

$$\delta r_{\text{slant}} = \frac{c}{2 \cdot B_p}, \tag{2.1}$$

where $\frac{c}{2}$ is the two-way speed of light. When projecting to the ground range, the resolution is associated with the local incident angle

$$\delta r_{\text{ground}} = \frac{c}{2 \cdot B_p \cdot \sin(\theta_i - \alpha)}, \tag{2.2}$$

where θ_i is the normal incident angle, and α represents the local slope. Therefore, the range resolution is independent of the height of the sensor platform. In azimuth direction, the azimuth resolution of a real aperture radar is directly related to the ratio of the sensor wavelength to the antenna length

$$\delta a_r = \frac{\lambda r_0}{L_a}, \tag{2.3}$$

where λ is the wavelength, r_0 is the slant range, and L_a is the antenna length [20]. For a given wavelength, the longer the antenna, the higher the spatial resolution.

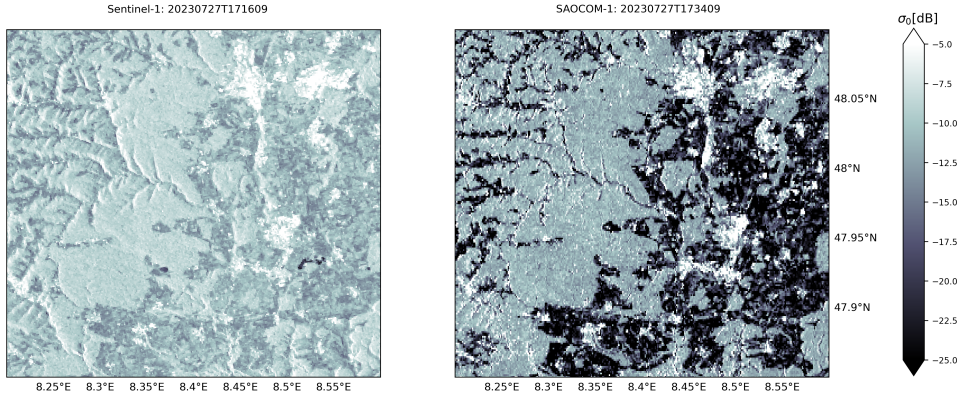

Figure 2.3: Co-polarized (VV) 100 m resolution backscatter observations over Black Forest, Germany 20230727 by Sentinel-1 (left, σ_0) and SAOCOM-1 (right, $\sigma_0 + 5$) respectively.

In SAR system, where the radar is mounted on a moving platform, each ground target exhibits a different relative speed with respect to the antenna, resulting in a distinct Doppler shift for each one. This Doppler shift allows the system to distinguish between targets located at the same range but different azimuth positions. If the target scene remains stationary as the SAR passes overhead, a synthetic aperture can be formed with a beamwidth of $\frac{L_a}{2r_0}$, resulting in an azimuth resolution of

$$\delta a = \frac{L_a}{2}, \tag{2.4}$$

which is the theoretical azimuth resolution of a stripmap SAR system, where the antenna stays in a fixed position during acquisition. For other acquisition modes, such as Terrain Observation by Progressive Scans (TOPSAR), in which the radar beam is steered during the acquisition[21], the azimuth resolution is approximately given by the ratio of the local projection of the satellite velocity, v_{ground}, to the processed Doppler bandwidth, B_{proc}, as expressed by

$$\delta a \approx \frac{v_{\text{ground}}}{B_{\text{proc}}}. \tag{2.5}$$

Compared to the real aperture radar, SAR achieves high-resolution imaging using relatively small physical antennas by synthesizing a larger effective aperture.

2.1.3. MEASUREMENTS

After SAR focusing, the lowest level product of a SAR system is a Single Look Complex (SLC) image. In a SAR image, the data of every resolution cell has a unique range and azimuth coordinate, each of the complex-valued measurement can be written in the form

$$P(m,n) = A(m,n)e^{j\phi(m,n)}, \tag{2.6}$$

where A is the amplitude which represents the square root of the intensity of the radar reflection from the corresponding resolution cell, j is the imaginary unit, and ϕ is the

phase of the received radar signal. The SLC phase can be expressed as the sum of four components

$$\phi(m,n) = \phi^{\text{range}} + \phi^{\text{atmo}} + \phi^{\text{scat}} + \phi^{\text{noise}}, \tag{2.7}$$

where the range dependent phase ϕ^{range} corresponds to the distance between the antenna and the effective phase center of the target, the atmospheric phase delay ϕ^{atmo} results from signal propagation through the atmosphere, the scattering phase ϕ^{scat} represents the interaction of the signal with the properties of the target, and phase noise ϕ^{noise} includes random errors due to thermal noise and other system uncertainties.

2.1.4. SPECKLE

Due to the finite resolution, signals received within each resolution cell originate from a distribution of scatterers. The random constructive and destructive interference of the multiple scattering returns leads to speckle. Since the scatterers vary across resolution cells, the resulting speckle patterns appear as bright and dark dots in a SAR image. Speckle, as an inherent noise, degrades the quality of a SAR image and complicates its interpretation. To improve the analysis and interpretation of SAR observations, speckle reduction is desirable. Since the speckle is randomly distributed in space, it is typically reduced through mutilooking or spatial filtering.

2.2. SAR INTERFEROMETRY

By multiplying one complex-valued SAR image with the complex conjugate of another, information about the imaged objects can be extracted from the resulting interferometric phase, which encodes surface displacement, atmospheric effects, and other contributions, and from the normalized interferometric correlation, commonly referred to as coherence, which reflects the similarity between acquisitions and indicates data quality. To produce a meaningful interferometric product, the two images must differ in at least one aspect, referred to as the baseline, which can be either temporal or spatial. In general, interferometry can be conducted in two distinct configurations: single-pass interferometry, which collects data simultaneously using multiple antennas, and repeat-pass interferometry, which acquires images with a single sensor at different times. Based on the assumption that all interferometric phases can be explained geometrically, SAR interferometry has been widely used in geodesy for monitoring surface deformation and mapping digital elevation.

Figure 2.4 shows an example of Sentinel-1 interferometric SAR observations after InSAR processing over southern France. With the flat Earth and topographic phases removed, the interferometric phase image on the left primarily represents an atmospheric phase screen, with potential deformation signals obscured by atmospheric effects. On the right, the coherence magnitude reflects the correlation between two acquisitions separated by a 6-day temporal baseline. High coherence values are typically observed in urban areas, where the build-up structures exhibit greater temporal phase stability compared with most natural targets.

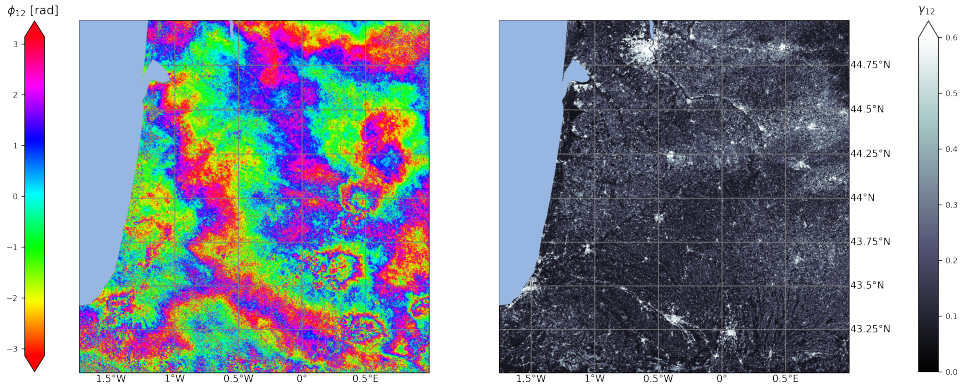

Figure 2.4: Co-polarized (VV) 200 m resolution interferometric phase (left) and corresponding coherence (left) over southern France with Sentinel-1 acquisitions on 20170710 and 20170716.

2.2.1. CONFIGURATIONS

With different SAR sensor configurations, single-pass interferometry can be categorized as Along Track Interferometry (ATI) and Cross-Track Interferometry (XTI). In an ATI configuration, antennas are separated in the along-track direction, the resulting interferograms provide highly sensitive measurements of the line-of-sight (LoS) velocity. This type of interferometry is mainly used to detect moving ground target and to study ocean surface currents [22]. In an XTI configuration, the antennas are separated in the across-track direction. The phase difference in the cross-track interferogram contains information about the angle at which the radar echo was received. By combining this phase difference with distance information, the three-dimensional position of each image pixel can be determined. This technique is commonly used to generate a digital elevation model (DEM).

In repeat-pass interferometry, the two images are acquired at different times, leading to two possible sources of phase shift: terrain altitude and terrain motion. For space-borne SAR, the repeat cycle of the satellite is not identical, resulting in a slight across-track shift in its orbits. This shift introduces sensitivity to height, which is often undesirable in applications such as monitoring land deformation between acquisitions. As this study uses Sentinel-1, our interferometric observations are obtained via repeat-pass interferometry, and the effect of orbit shifts is analyzed through baselines.

2.2.2. PROCESSING

The process of producing interferograms from two SLC images differs across software and applications. In general, it consists of six steps, as shown in the diagram in Figure 2.5: co-registration, interferogram generation, phase flattening, multilooking, phase unwrapping, and geocoding. Although a complete InSAR processing chain after interferogram formation is not required for this project, since it primarily addresses geometrical phases while our focus is on the geophysical component of the interferometric phase, we briefly discuss each step for completeness, emphasizing those most relevant for this study.

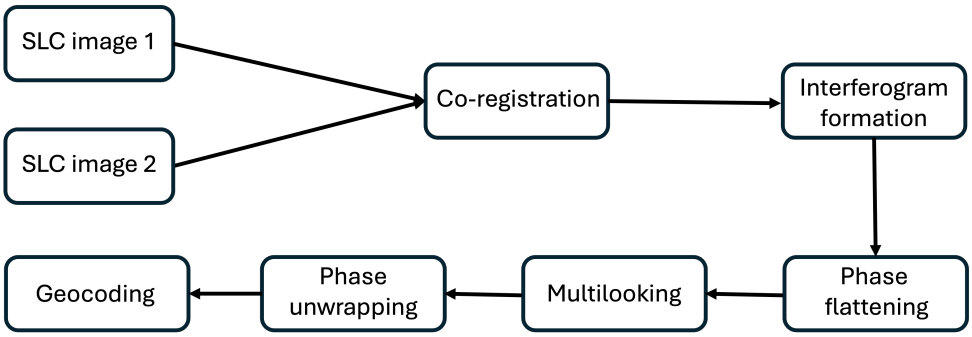

Figure 2.5: General inSAR processing diagram.

CO-REGISTRATION

Since two SAR images are required to form an interferogram, they must be co-registered to match the pixels in both images with the same area on the ground. This means that the sampling grids of the two images need to be aligned. Typically, one image is assigned as the reference, and the other image is resampled onto the reference grid. Co-registration is an essential step for accurately determining phase differences. Poor co-registration can severely reduce the interferometric coherence [23] and, as a result, lead to incorrect phase estimates.

INTERFEROGRAM FORMATION

After aligning the two SLCs images, the interferogram is generated by performing a cross-multiplication of corresponding pixels from two images. Mathematically, each pixel of the interferogram can be expressed as

$$\begin{aligned} I(m,n) &= P_1(m,n)P_2^*(m,n) \\ &= A_1(m,n)A_2(m,n)e^{j(\phi_1(m,n)-\phi_2(m,n))}, \end{aligned} \tag{2.8}$$

where $\phi_1(m,n)-\phi_2(m,n)$ represents the interferometric phase of a pixel at coordinate (m,n). This interferometric phase term consists of four components: the phase contribution due to geometry differences, the phase contribution due to differences in scattering, the phase contribution due to differences in atmosphere, and the sum of phase noise from both pixels. Most interferometric phase components can be addressed during InSAR processing, leaving the atmospheric, deformation, and scattering phases. Among these, correcting for atmospheric effects has long been one of the greatest challenges in achieving reliable deformation phase [24]. In this dissertation, we form closure phases from interferometric phase triplets, which are immune to geometric contributions and therefore circumvent this issue, providing direct insight into the scattering phase.

PHASE FLATTENING

After interferogram generation, the variability of the interferometric phase can be reduced by compensating for predictable phase contributions, this progress is known as flattening. The most well-known deterministic phase contributions are the flat Earth

phase and the topographic phase. Because SAR images are acquired in the slant-range direction, a flat Earth phase arises from the distance difference between objects at the same height as the radar signal propagated from near to far range. This phenomenon produces periodic interference fringes, which obscure the phase variations caused by topographic changes, and add complexity for subsequent processing [25]. The topography phase is caused by the surface height variations relative to a reference surface. In this study, this phase component is calculated and removed using a combination of a Digital Elevation Model (DEM) and baseline data.

MULTILOOKING

Multilooking is a crucial process used to reduce phase noise, thereby improving the estimates from interferometric phase [26], while also producing a product with a desirable resolution. In general, there are two main multilooking strategies. The first is the standard box-car multilooking, which applies a moving-average window to simply average adjacent pixels. The second is adaptive multilooking, which selects candidate pixels based on their statistical properties [27] or associated geophysical conditions. Both methods operate under the assumption that the multilooked pixels belong to a statistically homogeneous region [23].

Since the main objectives of this study involve extensive statistical analysis and quantification of phase contributions from distinct scattering mechanisms, an appropriate multilooking strategy is essential. To investigate the statistics of closure phases, substantial multilooking is required to ensure a sufficient number of independent samples (i.e., a high equivalent number of looks) for the analysis. Moreover, given the large research area, kilometer-scale resolution is preferred over meter-scale resolution to improve computational efficiency and visualization clarity. From the perspective of phase product representativeness, the commonly used box-car multilooking method carries a high risk of mixing scatterers from different scattering families. To address this issue, we adopt an adaptive multilooking strategy, which averages only pixels assumed to be realizations of the same random distribution, thereby reducing the risk of mixing different scattering families and producing higher-quality phase products that are more representative of statistically homogeneous regions.

PHASE UNWRAPPING

The interferometric phase is wrapped modulo 2π and ranges from $-\pi$ to π. As a result, differences in range are mapped to the same interval, making the measured range distance ambiguous by multiples of the wavelength. Phase unwrapping is the process of resolving phase ambiguity using prior knowledge or assumptions [28]. The most common assumption in InSAR application is that the unwrapped phase fields varies slowly, such that the phase difference between neighboring pixels remains less than half a wave cycle [29]. Depending on the number of images used to solve the 2π ambiguities, different methodologies are applied.

GEOCODING

The original SAR measurements are acquired in radar geometry, defined by the flight direction of the platform (azimuth) and the line-of-sight direction of the radar (slant range). Because the raw data precisely define an object's position and movement by

relating received echo signals directly to radial distance and angular position, all signal processing steps are carried out in radar coordinate. Processing raw signals in a geographic coordinate system would introduce unnecessary complexity and potential errors, therefore, geocoding is applied as a secondary step after the main radar processing. This step reprojects the interferogram into the desired geographic coordinates. Aligning geocoded interferograms with a reference system consistent with certain geophysical maps enables easier comparison and analysis between InSAR observations and local geophysical variations. In this dissertation, the geophysical datasets, such as soil moisture data, land use map and weather records, are all provided in geographic coordinates. Therefore, geocoding is needed to locate the relevant geophysical datasets, match them with our radar observables, and help interpret the observed signatures.

2.2.3. MEASUREMENTS

Interferometric SAR provides two key measurements: interferometric phase and coherence. Given two co-registered SLCs images, $i_1 = A_1 e^{j\phi_1}$ and $i_2 = A_2 e^{j\phi_2}$, and extending the notation from (2.8), the interferogram I_{12} can be written as

$$\begin{aligned} I_{12} &= i_1 i_2^* \\ &= A_1 A_2 e^{j(\phi_1 - \phi_2)} \\ &= |I_{12}| e^{j\phi_{12}}, \end{aligned} \tag{2.9}$$

where ϕ_{12} represents the interferometric phase, and $|I_{12}|$ denotes the amplitude of the interferogram. Meanwhile, the normalized interferometric correlation (complex coherence) can be written as

$$\gamma_{12} = \frac{E[i_1 i_2^*]}{\sqrt{E[|i_1|^2]E[|i_2|^2]}}. \tag{2.10}$$

It is typically estimated using sample coherence, given by

$$\hat{\gamma}_{12} = \frac{\sum_{m,n} P_1(m,n) \cdot P_2^*(m,n)}{\sqrt{\sum_{m,n} |P_1(m,n)|^2} \sqrt{\sum_{m,n} |P_2(m,n)|^2}}, \tag{2.11}$$

where $P_i(m,n) = A_i(m,n) e^{j\phi_i(m,n)}$. However, this is a biased estimator, with the bias depending on the true coherence. It tends to overestimate low coherence, and the bias decreases as the number of independent samples increases [23]. The amplitude of the complex coherence is an indicator of the interferometric phase quality, ranging from 0 for completely independent images to 1 when $i_2 = C i_1$, where C is a constant complex number. In this case, coherence is preserved as long as all scatterers within a resolution cell undergo the same phase change.

In general, accurate phase measurements require either high coherence or the averaging of a sufficiently large number of samples. However, several mechanisms can lead to signal decorrelaton, resulting in a loss of coherence [30]. Categorizing these mechanisms into four main factors, the coherence can be expressed as

$$\gamma = \gamma_{\text{noise}} \gamma_{\text{system}} \gamma_{\text{temporal}} \gamma_{\text{spatial}}. \tag{2.12}$$

γ_{noise} represents the decorrelation caused by thermal noise in the radar instrument. System decorrelation, γ_{system}, is related to the imperfection in radar systems and processing, including co-registration and resampling errors. Temporal decorrelation, γ_{temporal}, results from changes in observed objects over time, such as soil moisture variations, vegetation growth and ice melting. Spatial decorrelation, γ_{spatial}, can be further categorized into geometric decorrelation and volume decorrelation, and can therefore be written as

$$\gamma_{\text{spatial}} = \gamma_{\text{geo}}\gamma_{\text{vol}}. \tag{2.13}$$

Geometric decorrelation, γ_{geo}, mainly arises from differences in viewing geometry between the images, such as the baseline caused by non-identical satellite positions and the geometric distortions due to variations in slope orientation relative to the satellite [31]. Volume decorrelation, γ_{vol}, is caused by multiple scatterers within a resolution cell having different interferometric phases, which introduces phase uncertainty. In this study, when exploring the scattering mechanisms responsible for closure phases, we focus primarily on geophysical variations. Therefore, among all decorrelation terms, we address temporal decorrelation arising from geophysical changes in observed objects, as well as volume decorrelation.

2.2.4. HEIGHT OF AMBIGUITY

The height of ambiguity (HoA) represents the height difference that generates a 2π interferometric phase change after flattening, defining the maximum unambiguous measurable elevation change. It is inversely proportional to the perpendicular baseline $B_\perp$, and given by

$$h_{\text{amb}} = \frac{\lambda R \sin\theta_i}{2B_\perp}, \tag{2.14}$$

where R is the one-way slant range [32]. The HoA is commonly used to indicate the sensitivity of an interferometer to topographic height. A smaller HoA increases sensitivity to small elevation differences and to spatial decorrelation, making it suitable for detecting small height changes but less effective at resolving large topographic variations. Conversely, a larger HoA is less sensitive to small variations and decorrelation but enables resolving large, abrupt height differences. Since HoA is inversely proportional to the perpendicular baseline, increasing the baseline improves the accuracy of resolving topographic features, as phase noise corresponds to smaller height noise, though at the expense of higher sensitivity to decorrelation [33, 34]. Although this study does not address geometric variations directly, the HoA is used to construct perpendicular baseline triplets for investigating the contribution of volume scattering mechanisms to closure phases.

2.3. INSAR CLOSURE PHASE

Closure phases are defined as the phases of the product of three interferograms formed by circularly interfering three SAR images, i_1, i_2 and i_3 [35]. The three interferograms are computed from all pairwise combinations of the three acquisitions. Mathematically, the so-called closure phase is expressed as the phase of

$$I_{12}I_{23}I_{31} = |I_{12}||I_{23}||I_{31}|e^{j(\phi_{12}+\phi_{23}+\phi_{31})}, \tag{2.15}$$

so that

$$\Phi_{123} = \phi_{12} + \phi_{23} + \phi_{31}. \tag{2.16}$$

In practice, closure phases are formed using multilooked interferograms. A schematic illustration of constructing InSAR closure phases from three SAR acquisitions is shown in Figure 2.6.

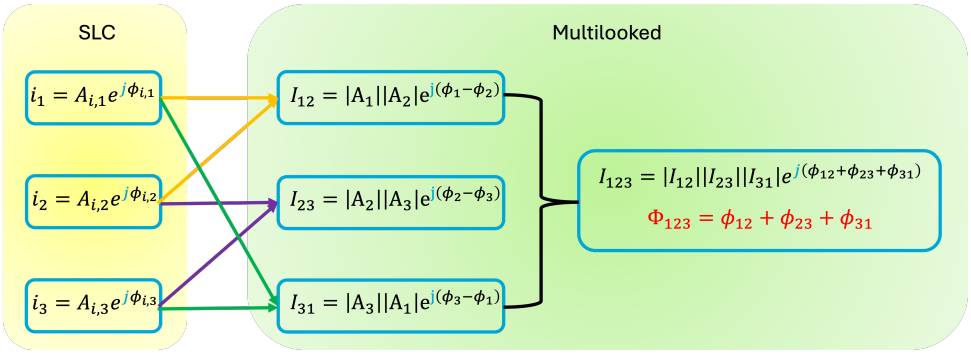

Figure 2.6: Formation of InSAR closure phases, mathematical representation

2.3.1. NON-ZERO CLOSURE PHASES

At the pixel level, without multilooking the complex-valued interferograms, this quantity is always equal to zero by mathematical construction. When closure phases are computed from spatially averaged (multilooked) interferograms, the assumption of spatial ergodicity allows the multilooked interferogram to be treated as an estimate of its expected value. Within this framework, non-zero closure phases emerge, comprising both residual phase noise after multilooking and a geophysical component associated with scattering mechanisms.

Figure 2.7 presents examples of Sentinel-1 co-polarized (VV) closure phase (upper panel) and radar backscatter (lower panel) observations at 200m resolution, derived from January acquisitions over various locations, including the Netherlands, Denmark and France (from left to right). Above each image, the acquisition dates of the SAR images are presented in the year/month/day format. Some regions exhibit noisy patterns, for example, the bottom-left corner of the observation over France shows saturated random noise within the assigned dynamic range of $-20°$ to $20°$. However, the majority of these closure phase observations deviate significantly from zero, with many showing a predominantly positive signature during this period. With the aid of the backscatter observations in the lower panel, the closure phase signatures can be related to underlying geophysical conditions. In the Netherlands, the observed area is mostly cropland, while water bodies and urban regions stand out with very low and high backscatter, which correspond to noisy and near-zero closure phases, respectively, whereas the croplands are associated with regions of positive closure phases. The area in Denmark also contains extensive cropland. However, the low backscatter regions associated with noisy closure phases are not water bodies but densely vegetated areas, such as forests. From the example over France, it is difficult to derive information correlating with land use because a

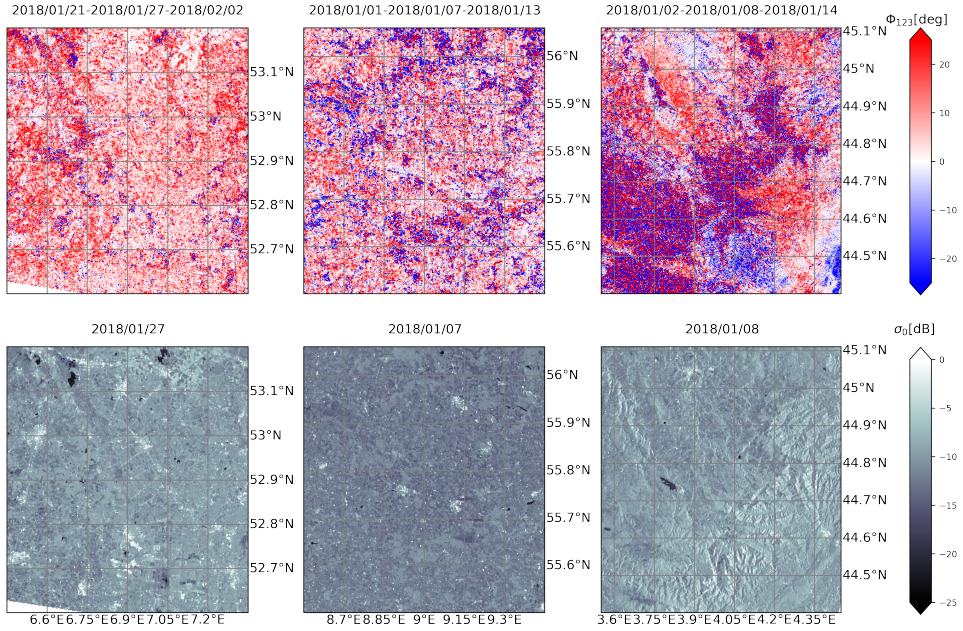

Figure 2.7: Sentinel-1 co-polarized (VV) 200 m resolution closure phase (upper panel) and radar backscatter (lower panel) observations in various locations, from left to right, the regions shown are the Netherlands, Denmark, and France, respectively.

large region exhibits highly noisy closure phases. However, this pattern does not persist, as it is caused by day-to-day variations in weather.

All geometrical effects, which do not account for variations in the scattering properties of the objects and affect independently in each image, cancel out within the phase triplets. When we interfere data involving contributions from different scatterer families, each exhibiting distinct behaviors in interferometric phase alone or in both interferometric phase and intensity, the nullity in the expected value of closure phases breaks [1]. Therefore, the presupposition that one can replace distributed scatterers with an equivalent persistent one is no longer valid.

2.3.2. NOISE-INDUCED CLOSURE PHASES

The introduction of the concept of InSAR closure phases, and its non-zero magnitudes in observations challenges the implicit phase consistency assumption in InSAR. When the concept was introduced in InSAR, people took two different positions regarding the origin of the phase inconsistency. For example, some studies claim that phase inconsistencies are purely due to phase noise, explaining these inconsistencies in terms of the statistical properties of pixels within the multilooking window [36]. In contrast, other research firmly rejects the noise-only statement and shows real data examples of phase inconsistencies with geophysical origins [2] [1] [6] [37].

To provide quantitative evidence for the presence of geophysical non-zero closure

phases, we statistically assess their contribution through numerical simulations. By assuming a circular Gaussian-distributed homogeneous speckle and describing the correlation between images with a covariance matrix that uses the three observed coherence values as inputs, one can estimate the standard deviation of closure phase arising purely from decorrelation phase noise. The estimated standard deviation is used as a normalization factor for the closure phase observations. Statistics of the normalized closure phases, measured by deviations from a Gaussian distribution, provide an indication of the existence of a geophysical component. A detailed description of the numerical model is presented in Section 3.4.

2.3.3. GEOPHYSICAL CLOSURE PHASES

We can model the contribution of two scattering mechanisms, each with their distinct phase behaviour by assuming that they contribute with a and $be^{j\phi}$ to the complex valued scattering coefficient:

$$\begin{aligned} i_1 &= a + be^{j\phi_1} \\ i_2 &= a + be^{j\phi_2} \\ i_3 &= a + be^{j\phi_3}. \end{aligned} \tag{2.17}$$

Since a common phase term cancels out without affecting the value of the closure phases, we assume that one scattering mechanism, a, has no phase component. Assuming the scattering mechanisms are independent of each other, $E[ab^*] = 0$, the corresponding multilooked interferograms can be written as

$$\begin{aligned} E[I_{12}] &= E[|a|^2] + E[|b|^2]e^{j(\phi_1-\phi_2)} \\ E[I_{23}] &= E[|a|^2] + E[|b|^2]e^{j(\phi_2-\phi_3)} \\ E[I_{13}] &= E[|a|^2] + E[|b|^2]e^{j(\phi_1-\phi_3)}, \end{aligned} \tag{2.18}$$

where $E[|a|^2] \neq 0$ and $E[|b|^2 \neq 0]$, indicating that we have two distinct scattering mechanisms, and $\phi_1 \neq \phi_2 \neq \phi_3$, reflecting the three different images. Except for the case in which $E[|a|^2] = E[|b|^2]$, the resulting closure phase Φ_{123} will always deviate from zero [1] [3]. In a more general scenario of two scattering mechanisms, where both interferometric phase and intensity vary independently, the intensity component increases the effect of phase inconsistency and non-zero closure phase is persistent.

The introduced theory for two distinct scattering mechanisms can be further extended to the general case of multiple scattering mechanisms. For n sets of independent scattering mechanisms, each characterized by a real covariance matrix C_i, the multiple scattering covariance matrices can be written as

$$C = \sum_{i=1}^{n} \Delta_i^* C_i \Delta_i, \tag{2.19}$$

where i stands for the different scattering mechanism, Δ_i represents diagonal matrices with pure phase terms, describing the phase of the scattering mechanism [1]. A typical

extension of (2.19) results from considering a volumetric object, and assuming that the interferometric properties vary continuously along the vertical axis, giving

$$C = \int_z \Delta(z)^* C(z) \Delta(z) dz. \tag{2.20}$$

In current literature, changes in dielectric properties of a medium including soil moisture variations, wet biomass accumulation and snow metamorphism, volume scattering in combination with perpendicular baselines, and differential skewed movements are recognized as three contributors to geophysical closure phases [1, 6, 8]. Analytical expressions have been developed for two mechanisms: one involves the variation in the propagation properties of dielectric media induced by soil moisture changes [2], and the other corresponds to volume scattering in the presence of perpendicular baselines [1].

2.3.4. MODELING

A SOIL MOISTURE MODEL

Since the soil moisture contribution to the SAR interferometric phase was first recognized with SEASAT [38], moisture-related signatures have been observed in InSAR images using various platforms [1, 2, 7, 11, 39]. Early studies attributed differential phase signatures to the geometric effect of vertical field expansion [38, 40]. This mechanical expansion hypothesis was later challenged, with the alternative explanation that soil moisture variations alter the dielectric properties of the medium, thereby affecting wave propagation and contributing to interferometric phase changes [41, 42]. Subsequently, Rabus *et al.* introduced a numerical model that explicitly accounts for soil moisture distribution and air-filled voids, further demonstrating that soil moisture variations influence the interferometric phase [43]. To analytically connect interferometric phase to dielectric variations induced by soil moisture changes, De Zan *et al.* developed an analytical soil moisture model, proposed an inversion algorithm based on coherence magnitudes, and extended the model to closure phase analysis [2, 11, 44].

Several assumptions are made to simplify the analytical representation of soil moisture variation in relation to the interferometric phase. First, the geometry is simplified to two dimensions, with the azimuth direction assumed to be orthogonal to the incident plane, as shown in Figure 2.8. Second, the soil is treated as a linear and isotropic medium, with scatterers having a constant permittivity ϵ at all depths. Third, the permeability μ is assumed to be identical in both air and soil.

Accepting these assumptions and neglecting the effect of surface scattering, an interferometric soil moisture model is developed. For a focused pixel at range r_0 and azimuth y_0, the model is expressed as an integral over the contributions of elementary scatters, each weighted by the appropriate propagation phase introduced by the soil

$$p(r_0, y_0) = \int_0^\infty \xi(z) e^{-j2k_z' z} dz, \tag{2.21}$$

where the scatterer distribution $\xi(z)$ can be seen as a realization of a stochastic process, characterized by the property

$$E[\xi(z)\xi^*(z_0)] = f(z)\delta(z - z_0), \tag{2.22}$$

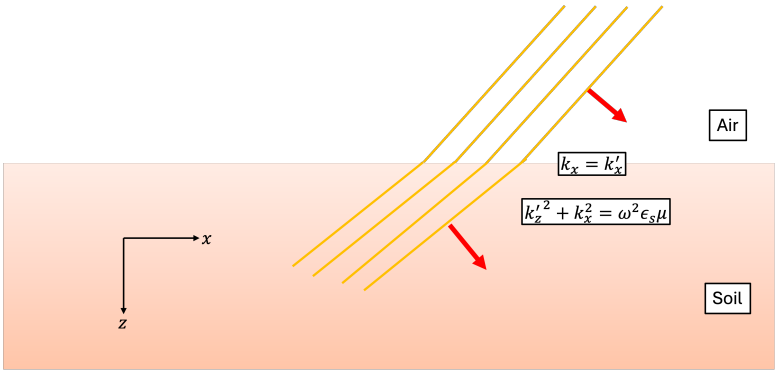

Figure 2.8: Geometry of plane wave incidence and refraction on a flat lossy medium [1].

and k'_z is the refracted vertical wavenumber in the soil, given by

$$k'_z(\epsilon_r) = \sqrt{\omega^2 \epsilon_0 \epsilon_r \mu - k_x^2}, \tag{2.23}$$

where $\omega = 2\pi f$, ϵ_0 is the permittivity of free-space, ϵ_r represents the dielectric constant of the medium, μ is the permeability of the medium, and

$$k_x = \frac{2\pi}{\lambda} \sin\theta_i \tag{2.24}$$

is the horizontal wavenumber in air, expressed as a function of the radar wavelength λ and the incident angle θ_i. The horizontal wavenumber satisfies the boundary condition at the air-soil interface, such that $k'_x = k_x$ [2]. Hence, assuming a vertical scattering profile $f(z)$, we can write the expected value of the multilooked interferogram, formed by two images with different vertical wavenumbers, as

$$\begin{aligned} I(\epsilon_{r1}, \epsilon_{r2}) &= E[p_1 p_2^*] \\ &= \int_0^\infty f(z) e^{-j2k'_{z1}z} (e^{-j2k'_{z2}z})^* dz \\ &= \int_0^\infty f(z) e^{-j2k'_{z1} + 2jk'^{*}_{z2} z} dz, \end{aligned} \tag{2.25}$$

where ϵ_{r1} and ϵ_{r2} are the dielectric constants of the soil, k'_{z1} and k'_{z2} are the vertical wavenumbers of each acquisition [2]. For a uniform vertical scattering profile, (2.25) can be further simplified as

$$I(\epsilon_{r1}, \epsilon_{r2}) = \frac{1}{2jk'_{z1} - 2jk'^{*}_{z2}}. \tag{2.26}$$

Thus, the soil moisture variation induced closure phases can be modeled as

$$\begin{aligned} \Phi_{123} &= \angle(I(\epsilon_{r1}, \epsilon_{r2}) I(\epsilon_{r2}, \epsilon_{r3}) I(\epsilon_{r3}, \epsilon_{r1})) \\ &= \angle\left(\frac{1}{j(k'_{z1} - k'^{*}_{z2})(k'_{z2} - k'^{*}_{z3})(k'_{z3} - k'^{*}_{z1})} \right). \end{aligned} \tag{2.27}$$

By feeding (2.27) with three simulated volumetric soil moisture values Θ, each ranging from 0.02 to $0.98 m^3 m^{-3}$, we predict the closure phases for all possible combinations of these three soil moisture components and visualize them in a scatter plot in Figure 2.9. This figure illustrates the ambiguity in closure phase magnitudes, showing that different

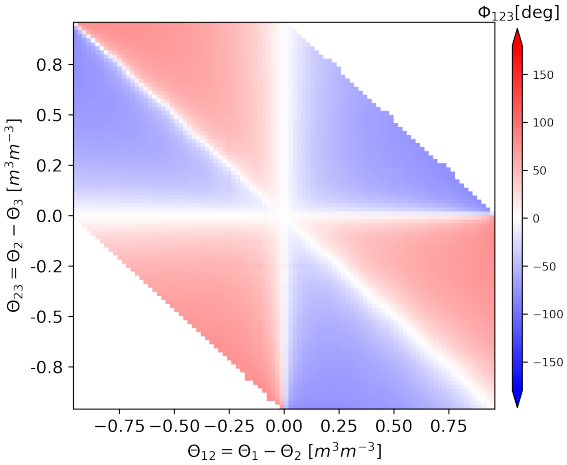

Figure 2.9: Predicted closure phase Φ_{123} for all possible combinations of simulated volumetric soil moisture values, each ranging from 0.02 to $0.98 m^3 m^{-3}$.

combinations of soil moisture values can result in the same closure phases. Specifically, a linearly decreasing soil moisture trend produces a negative closure phase, and circular permutations of the soil moisture sequence also yield negative closure phases. Conversely, a linearly increasing soil moisture trend produces a positive closure phase, and rotating the order of soil moisture values does not change the resulting closure phases.

Over non- and sparsely-vegetated areas, the temporal variation of the dielectric constant in the soil is identified as the main contributor to the closure phase [2, 11]. Using bare field campaign soil moisture measurements, the forward model was validated within a short time span of E-SAR L-band data. However, its validity diminished over longer time spans when seasonal vegetation cycles (e.g. withering and growth) or artificial activities (e.g. plowing) induce coherence loss in images [2].

Since the soil moisture variation induced interferometric phase introduces biases in deformation estimation, the InSAR community has devoted substantial efforts to model inversion to better quantify and account for its effects [2, 4, 11, 39, 45, 46]. An initial attempt at relative soil moisture inversion, based on this model, was performed using observational data, as current knowledge does not allow for absolute values. The validation showed that the approach provided reasonable moisture estimates [2]. However, as shown in Figure 2.9, inversion algorithms face ambiguity issues. The sign of the closure phase remains unchanged under any cyclical permutation of three soil moisture values [39]. An additional algorithm incorporating coherence magnitudes was developed to address this issue [11]. Nevertheless, the experimental data were specifically selected, and the dataset size was limited. Although coherence loss cannot be fully attributed to

soil moisture variations, and attempts to link soil moisture to closure phases reveal the model's incompleteness, this soil moisture model provides a foundation for developing geophysical interferometric models that incorporate multiple scattering mechanisms.

A VOLUMETRIC SCATTERING MODEL IN COMBINATION WITH PERPENDICULAR BASELINES

In addition to variable dielectric, geometrical volume scattering in combination with perpendicular baseline plays a role in closure phases over areas where there are scatterers at different heights and with a skewed vertical reflectivity profile. Considering only this mechanism, the expected value of the interferogram between two images, expressed as a function of the two-way differential vertical wavenumber

$$\kappa_z = \frac{2\pi}{h_{\text{amb}}}, \tag{2.28}$$

can be written as

$$I(\kappa_z) = \int f(z) e^{j\kappa_z z} dz, \tag{2.29}$$

where $f(z)$ is a real-valued scattering profile. The volume scattering-driven closure phases can be expressed as

$$\Phi_{123} = -\frac{1}{2} E[(z-\mu_z)^3] \kappa_{z1z2} \kappa_{z2z3} \kappa_{z3z1}, \tag{2.30}$$

where $\mu_z = E[z]$ and $E[(z-\mu_z)^3]$ are the 1st moment and the 3rd central moment of the scattering profile, respectively [1]. This result indicates that, even in the case of small baselines, non-zero closure phases can still arise due to the skewness of the scattering profile.

For the specific case of an exponential vertical profile, $f(z) = e^{-z}$, with the integral taken from zero to infinity, the expected value of the interferogram in (2.29) becomes

$$\begin{aligned} I(\kappa_z) &= \int_0^\infty e^{-z} e^{j\kappa_z z} dz \\ &= \frac{1}{1 - j\kappa_z}. \end{aligned} \tag{2.31}$$

Thus, the volume scattering induced closure phases can be predicted using a model equivalent to (2.27). Since the κ_z is real-valued in this case, (2.27) simplifies to:

$$\Phi_{123} = \angle \left(\frac{1}{(1 - j\kappa_{z1z2})(1 - j\kappa_{z2z3})(1 - j\kappa_{z3z1})} \right). \tag{2.32}$$

3

Data and Processing

3.1. Research area

As we aim to systematically analyze closure phases and explore their spatiotemporal statistical properties, selecting a sufficient large and diverse research area is essential. In addition, we use the Sentinel-1 dataset for this research, as it is the only satellite mission providing systematic and continuous SAR observations. Considering its 6-day revisit time, we selected a study area in Europe that is fully covered by this revisit cycle. After assessing variations in geophysical conditions, including land cover types, climate zones, and topography, we selected the Iberian Peninsula, covering approximately 600 000 square kilometers, as our study region. Considering the vegetation types and topography, this region contains forests in mountainous regions, extensive croplands in relatively flat regions, herbaceous vegetation in both dry and wetland environments, and shrubs mainly concentrate along the southeast coast. Regarding the climate zones associated with various weather conditions, and based on the Köppen-Geiger climate classification, this region primarily features four main climate types: cold semi-arid climate (BSk), warm-summer Mediterranean climate (Csb), hot-summer Mediterranean climate (Csa) and subtropical highland climate (Cfb). In Andorra, located in the northwest of the Iberian Peninsula, the climate transitions from warm-summer humid continental (Dfb) on the outer regions to subarctic (Dfc) and tundra (ET) towards the inner areas, forming a concentric pattern. Meanwhile, a small portion of the peninsula falls within cold desert (BWk) and Mediterranean-influenced warm-summer humid continental (Dsb) climate zones. Therefore, this region, with its diverse land cover types and varied climate zones, as shown in Figure 3.1, allows for investigating how local conditions influence the statistical attributes of the closure phase.

3.2. Data

To bridge SAR observations with geophysical variations in the target scene, we utilize both SAR data and geophysical datasets. As the systematic and continuous acquisitions of Sentinel-1 offer the opportunity for the investigation of SAR observations over a wide

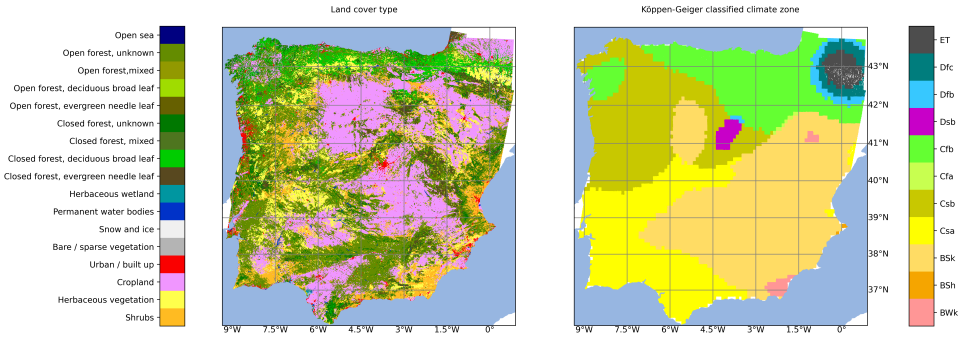

Figure 3.1: Resampled geophysical maps of research area: left is land cover map in 2017 [47] and right is Köppen-Geiger classified climate zone map [48].

area with consistent long-term coverage, we use data from the spaceborne Sentinel-1 C-band radar constellation, which offers a 6-day revisit time within the research area.

For geophysical data, we include a land cover map, a Köppen-Geiger classified climate zone map, soil texture maps, and hourly soil moisture products. The spatial and temporal resolutions of each dataset, along with their sources, are detailed in Table 3.1.

3.2.1. SENTINEL-1 DATA

The Sentinel-1 mission is a spaceborne SAR mission consisting of a constellation of two right-looking, sun-synchronous, polar orbiting satellites, operating at C-band with a center frequency of 5.405 GHz. The local time of the ascending node is around 18 : 00, and that of the descending node is around 06 : 00. A single Sentinel-1 satellite offers a repeat cycle of 12 days, while the constellation of two satellites reduces the revisit time to 6 days. Since orbit track spacing varies with latitude, the revisit rate is higher near the poles and the equator. For our study area, we used acquisitions from both satellites in 2017, achieving a 6-day temporal resolution, which was only possible when Sentinel-1A and Sentinel-1B were operational from April 2016 to December 2021. This 6-day revisit capability continues with Sentinel-1A and Sentinel-1C from December 2024 onward, and will eventually be provided by Sentinel-1C and Sentinel-1D.

Sentinel-1 can operate in dual-polarized mode, receiving in vertical and horizontal polarizations while transmitting in only one of these two polarizations. In general, over polar regions such as sea-ice zones, the system transmits in horizontal (H) polarization, generating co-polarized (HH) images and, optionally, also cross-polarized (HV) data. In other regions, Sentinel-1 provides observations in VV+VH or VV polarization. Sentinel-1 operates in four imaging modes: Stripmap (SM), Interferometric Wide Swath (IW), Extra Wide Swath (EW) and Wave (WV) mode. SM , IW and EW products are available in dual polarization (HH+HV or VV+VH), while WV operates in single polarization. In this dissertation, we selected dual polarization (VV+VH) acquisitions from IW mode, which is the primary mode for land observations, to cover our research area. IW mode captures images with a 250 km swath, consisting of three sub-swaths. Using TOPSAR (Terrain Observation with Progressive Scans SAR)[21], the resolution of a single-look pixel from IW

Table 3.1: Information for each date set.

Dataset	Temporal resolution	Spatial resolution	Source
Sentinel-1	6-day	5 m×20 m	European Union Copernicus programme
Land cover map	1-year	0.001°(≈ 111 m)	Copernicus Global Land Service (CGLS)
Climate zone map	-	0.1°(≈ 11.1 km)	Köppen-Geiger climate classification
Soil texture maps	-	250 m	International Soil Reference and Information Centre (ISRIC)
ERA5 volumetric soil moisture	1-hour	9 km	European Centre for Medium-Range Weather Forecasts (ECMWF)

mode acquisition is 5 m × 20 m.

In addition to ensuring full coverage of the research area with dual polarization images, we are also interested in observations acquired at different time, morning and afternoon, since daily geophysical patterns can vary significantly. Therefore, for each acquisition geometry, 6 a.m. (descending) and 6 p.m. (ascending), we processed four tracks of Sentinel-1 acquisitions to cover the research area. As introduced in the previous chapter, the formation of closure phases from SAR measurements requires InSAR processing as an intermediate step, with each stack of data requiring a reference image for co-registration. Because closure phase formation requires three consecutive acquisitions, generating all possible phase triplets using the first and last acquisitions from 2017 as the central images necessitates including scenes from the adjacent years. For each stack, we processed acquisitions from 2016-12-20 to 2018-01-10, selecting the last image of the stack as the reference. The Coordinated Universal Time (UTC) of each master date for each track stack is summarized in Table 3.2.

3.2.2. GEOPHYSICAL DATA

To maintain consistency with the timing of radar observations, we use geophysical datasets from the same year, 2017.

The land cover map provides vital information about the Earth's land use and cover patterns. The vegetation type information from the land cover map is essential for analyzing factors that influence radar signatures. That is because variations in the dielectric properties of the medium, which contribute to geophysical closure phases, are closely linked to vegetation type. Vegetation type directly affects vegetation phenology and,

Table 3.2: Information for each Sentinel-1 pass.

Pass	Geometry	Reference date and UTC time
008	descending	2018-01-06 06:11:23
052	descending	2018-01-03 06:35:11
081	descending	2018-01-05 06:18:47
154	descending	2018-01-04 06:27:55
001	ascending	2018-01-05 18:12:18
074	ascending	2018-01-04 18:19:59
103	ascending	2018-01-06 18:03:37
147	ascending	2018-01-03 18:28:53

consequently, the radar signal's interaction with the surface. The Copernicus Global Land Service (CGLS) provides a global dynamic land cover product, offering annual land cover information at a $0.001^\circ \times 0.001^\circ$ grid resolution according to the Land Cover Classification System (LCCS) scheme [47]. With an overall mapping accuracy just over 80% [49], this product provides 23 physical classes. Within our research region, 17 of these classes are present, as shown in Figure 3.1. Since the primary focus of the study is on statistical analysis, a detailed classification of land cover types is redundant, while the spatial extent of certain land cover types is important. Therefore, we concentrate only on the large scale vegetated regions, such as forests, cropland, herbaceous vegetation and shrubs.

The same type of vegetation can behave very differently under varying environmental conditions, for example, the weather patterns influence vegetation phenology, and thus alter radar signatures. As weather is highly dynamic, to further classify the vegetated areas based on weather patterns, we opt to use long-term averaged weather conditions—namely, climate, to further classify vegetated areas. The Köppen-Geiger climate classification map is a widely used reference across ecosystem and climate-related research. We use an updated version of the global climate classification map, gridded at $0.1^\circ \times 0.1^\circ$ resolution, derived using the Köppen-Geiger system and based on an extensive global dataset of long-term monthly precipitation and temperature records [48]. Following the same extensive spatial coverage criteria used for land cover types, we focus on the four main climate zones present within the research area: BSk, Csb, Csa, and Cfb.

In addition to the land cover and climate zone types, soil information is another key data source, since an interferometric model of soil moisture has been developed to explain closure phases variations, and one of the goals of this study is to quantify the effect of soil moisture on closure phase observations under various conditions. Implementing the interferometric soil moisture model requires two main soil properties: soil texture and soil moisture content.

Soil texture refers to the proportion of different soil mineral components, such as

sand, silt and clay. In the dielectric mixing model, which converts soil moisture to the the dielectric constant, the percentages of sand and clay in the soil are key inputs [50]. The International Soil Reference and Information Center (ISRIC) offers global gridded soil information through its SoilGrids products, which include global soil property maps at six standard depth intervals at a spatial resolution of 250 meters. Within our research region, we use the mean value maps of sand and clay content (in g/kg) at a depth of 0 to 5 cm, aligning with the typical penetration depth of C-band radar.

Compared to soil texture, soil moisture is highly dynamic. To enable a meaningful comparison between soil moisture variation and radar observables, it is necessary to align the acquisition times of both datasets as closely as possible. Since we have both 6 a.m. (morning) and 6 p.m. (afternoon) radar acquisitions, we require a soil moisture dataset with hourly high temporal resolution. In addition to this, considering the need for extensive spatial coverage, we opt to use the volumetric soil moisture product at a depth of $0-7$ cm from the hourly reanalysis land dataset provided by the European Center for Medium-Range Weather Forecast (ECMWF) [51]. Although this product provides hourly volumetric soil moisture with global coverage, its spatial resolution of 9 km is relatively coarse compared to radar observations. Therefore, we make the assumption that the coarse-resolution ERA5 soil moisture data is representative of a large area and that local heterogeneity in soil moisture variation is small. The uncertainty introduced by the discrepancy in spatial resolution is explicitly addressed in Section 5.2.2.

3.3. ADAPTIVE MULTILOOKING

The magnitude of the expected values of the closure phase and the interferometric coherence are tightly linked, with increasing mean closure phases necessarily leading to lower coherence and, therefore, increased phase noise. Consequently, regardless the magnitude of the mean closure phase, it always competes against the random closure phase contribution resulting from interferometric phase noise. Estimating closure phases in these conditions involves two key steps. Firstly, to minimize coherence loss due to temporal decorrelation, we used continuous 6-day revisit Sentinel-1 acquisitions to construct closure phases. Secondly, we applied extensive spatial averaging (multilooking) to reduce noise.

Aiming to average pixels from a statistically homogeneous region and obtain representative closure phase products, we adopt a three-step multilooking approach. Considering both the size of the research area, the entire Iberian Peninsula, and the effective number of samples within each multilooked cell, we opted to use a 1 km × 1 km multilooking window. The multilooking procedure with this window size involves:

1. multilooking single look inteferograms to a 20 m × 20 m grid [52] to reduce computational load,

2. classification of the multilooked data within 1 km × 1 km non-overlapping windows based on temporal statistics of multilooked amplitudes,

3. and averaging of 20 m × 20 m data points categorized as samples of the dominant class.

Each multilooked data point, representing the spatially averaged value of a set of single-look interferometric values, is referred to as a 'cell'. Each cell contains information about an interferometric phase, a real and positive-valued coherence, and an amplitude. Figure 3.2 provides a flowchart illustrating the multilooking steps.

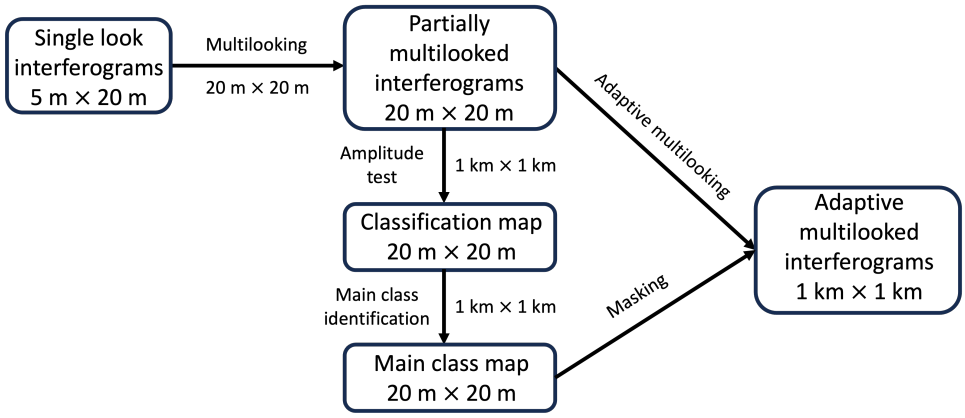

Figure 3.2: Diagram of three step multilooking data processing.

3.3.1. MATHEMATICAL REPRESENTATION OF RE-MULTILOOKING

Multilooking is performed on both complex-valued interferograms and intensities. The multilooked intensities are calibrated to represent the Normalized Radar Cross Section (NRCS) values. Using the notation consistent within the book, for a single pixel, we denote the amplitude as A, and the interferometric phase as $\phi_{12} = \phi_1 - \phi_2$. Correspondingly, the real and positive-valued coherence can be represented as $|\gamma_{12}|$. With these three quantities, we can construct the interferogram phasor as

$$I_{12} = |\gamma_{12}| A_1 A_2 e^{j(\phi_1 - \phi_2)}. \tag{3.1}$$

We then estimate the multilooked coherence as a sample average

$$\begin{aligned} \hat{\gamma}_{12} &= \frac{\sum_{i=1}^{N_p} I_{i,12}}{\sqrt{\sum_{i=1}^{N_p} |I_{i,11}|^2 \sum_{i=1}^{N_p} |I_{i,22}|^2}} \\ &= \frac{\sum_{i=1}^{N_p} \gamma_{i,12} A_{i,1} A_{i,2} e^{j(\phi_{i,1} - \phi_{i,2})}}{\sqrt{\sum_{i=1}^{N_p} A_{i,1}^2 \sum_{i=1}^{N_p} A_{i,2}^2}}. \end{aligned} \tag{3.2}$$

Here, N_p is the number of samples within a multilooking window. The multilooked interferometric phase is given by $\hat{\phi}_{12} = \angle(\hat{\gamma}_{12})$. In addition, the multilooked intensity is

$$\widehat{A^2} = \frac{\sum_{i=1}^{N_p} A_i^2}{N_p}. \tag{3.3}$$

3.3.2. CLASSIFICATION

Classification methods based on backscattering amplitudes of radar complex returns, A, have been shown to effectively preserve the physical meaning of phase signatures [53]. For a homogeneous area, the classical SAR generation model assumes SLC as a circular Gaussian distribution with variance σ_G^2. When considering the image amplitude, its distribution conforms to a Rayleigh distribution with a mean of

$$\mu_A = \sqrt{\frac{\pi}{2}}\sigma_G \tag{3.4}$$

and a variance of

$$\sigma_A^2 = \frac{4-\pi}{2}\sigma_G^2. \tag{3.5}$$

With N images, the mean amplitude for a pixel p can be computed as

$$\mu_{Ap} = \frac{1}{N}\sum_{i=1}^{N} A_{p,i}. \tag{3.6}$$

According to the central limit theorem, when N is a large number, the estimated μ_{Ap} is Gaussian distributed with mean

$$\mu_{\mu_{Ap}} = \sqrt{\frac{\pi}{2}}\sigma_G \tag{3.7}$$

and variance

$$\sigma_{\mu_{Ap}}^2 = \frac{4-\pi}{2N}\sigma_G^2. \tag{3.8}$$

According to the null hypothesis, where pixels are considered as realizations of the same random distribution, the expected value of their amplitudes over time (μ_A) can be standardized to follow a standard normal distribution with respect to the reference pixel:

$$\mu_A \sim N(\mu_{A_{\text{ref}}}, \frac{\sigma_{A_{\text{ref}}}^2}{N_i}), \tag{3.9}$$

where N_i is the number of images. The testing statistic, T_μ, can be defined as

$$T_\mu = \frac{(\mu_A - \mu_{A_{\text{ref}}})\sqrt{N_i}}{\sigma_{A_{\text{ref}}}}, \tag{3.10}$$

and the null hypothesis is rejected when

$$|T_\mu| > k_\alpha, \tag{3.11}$$

where α is the significance level and k_α is at the α percentile of the folded normal distribution [54]. Based on simulations over slightly multilooked (4-look) Rayleigh-distributed amplitudes, we set the significant level threshold to 0.975, resulting in approximately 80% classification accuracy under ideal conditions.

We applied this classification algorithm to a three-dimensional dataset with a spatial resolution of 20 m × 20 m, using 1 km × 1 km non-overlapping windows. For each window, we assigned labels to each class and identified the main class with the number of samples it contains. We then created a binary mask for each window to indicate the main class 20 m × 20 m cells.

3.3.3. MULTILOOKING

Using the main class map obtained from the classification step, we multilooked the intensities and the complex-valued interferograms of cells belonging to the main class within each 1 km × 1 km window. This multilooking process produces interferograms at a 1 km × 1 km grid, where each data point in the interferograms has an equivalent number of looks (ENL) related to the number of averaged cells.

3.3.4. GEOPHYSICAL LABELING

We assigned geophysical attributes to each multilooked cell to facilitate the analysis of closure phase statistics across sub-regions, which are categorized using geophysical maps, the land cover map [47], and the Köppen-Geiger classified climate map [48]. Following a procedure similar to multilooking, we first resampled the geophysical maps to align with the 20 m × 20 m SAR grid. Then, for each 1 km × 1 km cell, we determined the predominant geophysical type based on the majority type within each main class.

We selected forests, cropland, shrubs, and herbaceous vegetation as the four land cover types, which cover approximately 42%, 28%, 10%, and 9% of the entire research region, respectively. Each land cover type is further categorized into specific climate zones: cold semi-arid climate (BSk, 36%), warm-summer Mediterranean climate (Csb, 19%), hot-summer Mediterranean climate (Csa, 18%) and subtropical highland climate (Cfb, 14%). Analyzing observations within these categorized sub-regions allows us to investigate how local climate conditions may influence weather patterns and vegetation characteristics, thereby affecting closure phase signatures.

3.4. SIGNIFICANCE TEST

To assess whether the observed closure phase originates from a geophysical phenomenon (e.g. soil moisture variations), we performed a significance test based on the null hypothesis that closure phases caused by phase noise associated with the limited interferometric coherence. This significance test consists of two steps. First, we estimated the equivalent number of looks (ENL), denoted as N_l. Second, we calculated the standard deviation of closure phases caused by phase noise, considering the ENL and the estimated coherence for each interferometric pair. Using the threshold determined by the significance test results, we evaluated the significance of the geophysical component in closure phases.

3.4.1. EQUIVALENT NUMBER OF LOOKS

As oversampling introduces correlation among pixels in a SAR image, we estimated the ENL, N_l, to quantify the effective number of pixels within each multilooking area,

$$N_l = \frac{N_s}{R_{\mathrm{o,r}} R_{\mathrm{o,a}}}, \tag{3.12}$$

where N_s is the number of samples, $R_{\mathrm{o,r}}$ and $R_{\mathrm{o,a}}$ represent the oversampling ratio in the range and azimuth directions, respectively.

The oversampling ratio depends on system parameters, which can be expressed sep-

arately for each direction as

$$R_o = \frac{F_s}{\eta_e B}, \tag{3.13}$$

where F_s is the sampling frequency, η_e represents bandwidth efficiency, and B is the bandwidth. The bandwidth efficiency, η_e, is estimated using the formula

$$\eta_e = \frac{\left[\sum_{i=1}^{N_s} w_{1i}^2\right]^2}{\sum_{i=1}^{N_s} w_{1i}^4} \frac{\sum_{i=1}^{N_s} w_{0i}^4}{\left[\sum_{i=1}^{N_s} w_{0i}^2\right]^2}, \tag{3.14}$$

where w_{1i} represents discrete samples of the tapering window applied in SAR processing, typically a Hamming window. The term w_{0i} represents discrete samples of a rectangular window, and N_s is the number of samples[1].

Since the coefficient α_w that defines the Hamming window w_{1i} varies with subswath and direction, the number of samples in each direction is relevant for calculating the oversampling ratio. Assuming that pixels in the main class are clustered rather than sparsely distributed, we define the number of samples as the product of the number of samples in the range and azimuth directions. Therefore, we need to decompose the total number of samples into two components to calculate the oversampling ratio for each direction. To determine suitable factors for this decomposition, we conducted simulations of the 2D oversampling ratio, $R_{\text{tot}} = R_{\text{o,r}} R_{\text{o,a}}$, using varying numbers of samples in each direction. This exploration allows us to assess how different sample counts in the range and azimuth directions affect the magnitudes of R_{tot}. The simulation results depicted in Figure 3.3 suggest the oversampling ratio converges around sixteen samples. Therefore, we set the lower limit of the factorization to 16 and assigned this value to the range direction, considering the swath geometry where most pixels align along the azimuth direction. The derivation of ENL is illustrated in a flowchart in Figure 3.4.

3.4.2. NUMERICAL MODEL

Under the assumption that closure phases result from phase noise, we performed Monte-Carlo simulations using a numerical model to estimate the standard deviation of noise-originated closure phases σ. The numerical model takes the estimated ENL, and three real and positive-valued coherences ($\gamma_{s,12}$, $\gamma_{s,23}$ and $\gamma_{s,13}$), sampled uniformly from 0 to 1, as inputs. We generate white-noise vectors using ENL as the number of samples, while the interferometric coherences define the covariance matrix M_γ. The white noise is then transformed into correlated noise by applying the Cholesky decomposition of M_γ. Specifically, letting $M_\gamma = LL^H$, the correlated noise vector is obtained as

$$n_{\text{corr}} = L n_{\text{w}}. \tag{3.15}$$

To avoid repeating the procedure for every possible ENL combination, we perform the simulation using a fixed sample size of 2048. The numerical simulation produces a look-up table (LUT) for σ_n. We input observed coherence into the LUT to estimate corresponding σ_n and compute the standard deviation for each multilooked area by scaling

[1] The authors would like to thank Dr. Francesco De Zan for providing the methodology used to estimate bandwidth efficiency.

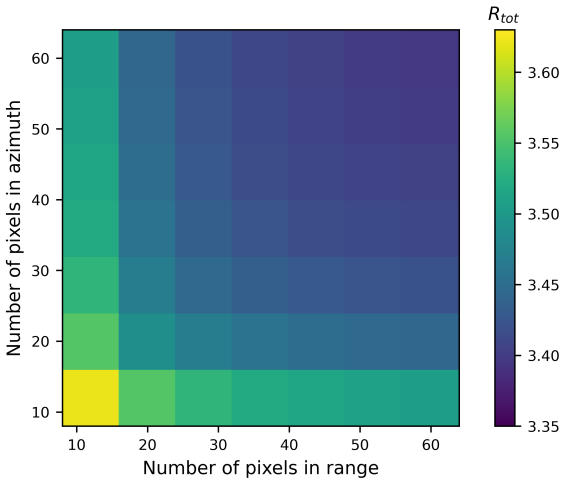

Figure 3.3: Simulated 2D oversampling ratio R_{tot} with different number of samples in range and azimuth directions.

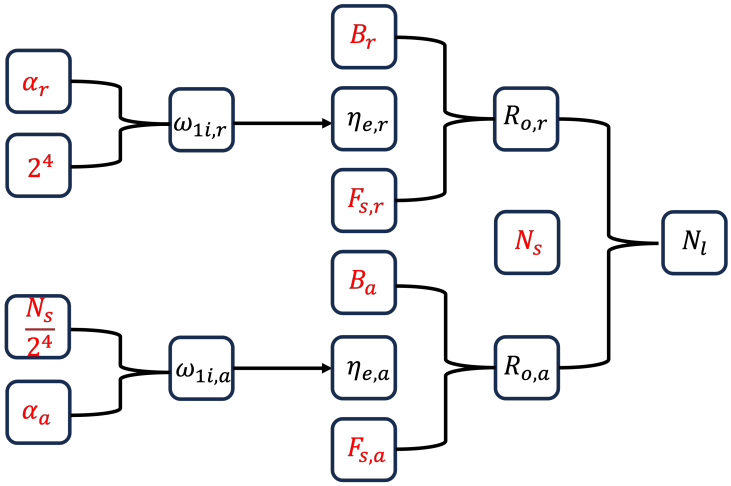

Figure 3.4: Flowchart of deriving Equivalent Number of Looks (ENL) with inputs system parameters (Hamming window coefficients α, bandwidth B and sampling frequence F_s) and assigned number of samples (2^4 and $\frac{N_s}{2^4}$) for range (subscript r) and azimuth (subscript a) direction respectively.

the model output σ_n with the corresponding ENL N_l as

$$\sigma = \sqrt{\frac{2048}{N_l}}\sigma_n. \tag{3.16}$$

Here we make the implicit assumption that the central limit theory can be applied, and that the variance scales with the inverse of the number of looks. As shown in Figure 3.5,

the estimated σ_n increases as coherence decreases and converges quickly as coherence increases. A flowchart of estimating the noise-originated standard deviation σ is visual-

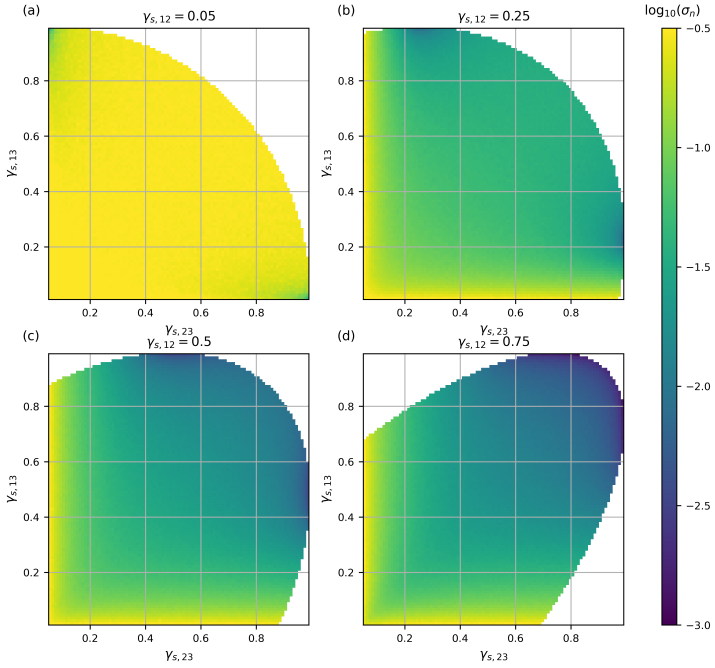

Figure 3.5: Logarithm scaled simulated standard deviation of noise-originated closure phase, $\log_{10}\sigma_n$, with the equivalent number of looks, equals to 2^{11} in different coherence scenarios: (a) $\gamma_{s,12} = 0.05$, (b) $\gamma_{s,12} = 0.25$, (c) $\gamma_{s,12} = 0.5$ and (d) $\gamma_{s,12} = 0.75$.

ized in Figure 3.6.

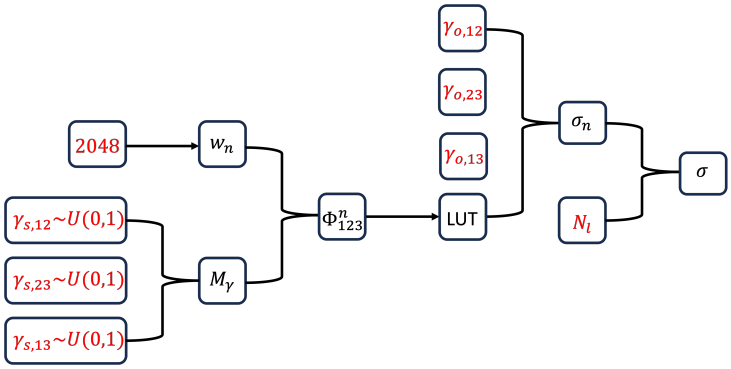

Figure 3.6: Flowchart of estimating the standard deviation of noise-originated closure phases using a numerical model with inputs coherence ($\gamma_{o,12}$, $\gamma_{o,23}$ and $\gamma_{o,13}$) and equivalent number of looks (N_l).

The performance of numerical models relates to the number of repeated simula-

tions. For both low and high coherence conditions, we apply the simulation with the same repetition and ENL parameters to inspect the variation of simulated results. As shown in Figure 3.7a and Figure 3.7b, although the changing of repetition times does not have a significant effect on the magnitude of σ_n, the sequence gets smoother with the increasing of N_l. Statistics of $\Delta\sigma_n$, which is the difference of the simulated results with different repetition times, are visualized to inspect the convergence in Figure 3.7c and Figure 3.7d. To balance computational runtime and ensure convergence of simulation results, we selected $N_r = 2^{10}$ for our model.

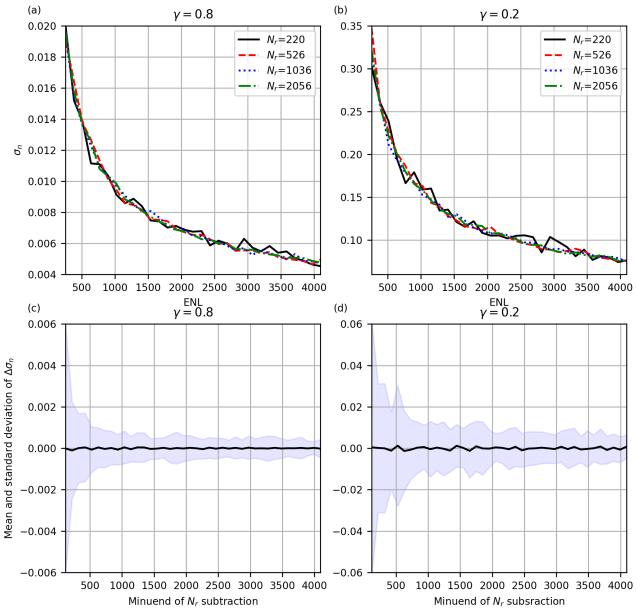

Figure 3.7: N_r selection: simulated σ_n with different N_r at a) high coherences, and b)low coherences, statistics of $\Delta\sigma_n$ at c) high coherences, and d) low coherences.

3.4.3. SIGNIFICANCE RATIO

Using the estimated standard deviation of noise-originated closure phases, σ_n, we introduced a measure of significance, the significance ratio R_Φ. This ratio is defined as the observed closure phases divided by the estimated standard deviation σ,

$$R_\Phi = \frac{\Phi_{123}}{\sigma}. \tag{3.17}$$

Under the noise-only null hypothesis, the significance ratio normalizes the distribution of closure phases to a standard normal distribution $N(0,1)$. Therefore, by assessing the

deviation of the significance ratio distribution from the standard normal distribution ($|R_\Phi| > 1.96$), we can statistically indicate the significance of geophysical closure phases.

Since a significance ratio of 1.96 corresponds to a 5% false alarm rate (false positives) in the noise-only scenario, when the fraction of identified samples with significant closure phases exceeds 5%, we consider the geophysical closure phases to be statistically significant. Without an estimation of the distribution of the geophysical closure phases, it is not possible to evaluate the false negative rate. In scenarios with low coherence and high phase noise, we can anticipate that the false negative rate can easily exceed the false positive rate. The survival rate minus 5% could be considered a conservative lower bound of the actual rate of cells with a geophysical closure phase.

4

CLOSURE PHASES AND THEIR SIGNIFICANCE

4.1. CLOSURE PHASE EXAMPLES AND THEIR SIGNIFICANCE

Before delving into the statistics of the closure phases, to illustrate their spatio-temporal variation, Figure 4.1 shows one closure phase example for each month during 2017 over the Iberian Peninsula, using VV-polarized morning (descending) acquisitions. These results are explicitly not obtained through temporal averaging, but directly represent individual closure phase observations. For each month, we chose dates with complete observations from four Sentinel-1 tracks. Among these dates, we selected the nearest acquisition dates, with a one-day time lag from west to east, to generate a closure phase map encompassing the entire research area.

The visualized closure phases exhibit relatively large dynamic ranges, spanning from -15° to 15°. Meanwhile, their spatial patterns reveal a connection to local geophysical condition variations. For instance, the Cantabrian and Pyrenees mountain ranges along the northern edge of the peninsula consistently exhibit noisy closure phases, due to low coherence resulting from complex local factors such as biomass and weather conditions. A temporal pattern is also evident, as the magnitude of the closure phases transitions from mainly positive in winter (left column) to predominantly negative in autumn (right column), potentially reflecting seasonal variations in local conditions. Additionally, in some examples, including those from February, June, and November, the edges of the swaths are discernible due to day-to-day weather variations, such as rain events [45]. This weather-related pattern is also reflected in regions occasionally exhibiting high absolute closure phase magnitudes. In contrast, examples from March and September, which show consistent spatial patterns across the area, suggest more stable local conditions.

Figure 4.2 shows the significant ratio, Φ_{123}/σ, corresponding to the closure phases in Figure 4.1. These significance ratios convey three main messages.

1. Visually noisy areas, such as mountain ranges, exhibit a low significance ratio mag-

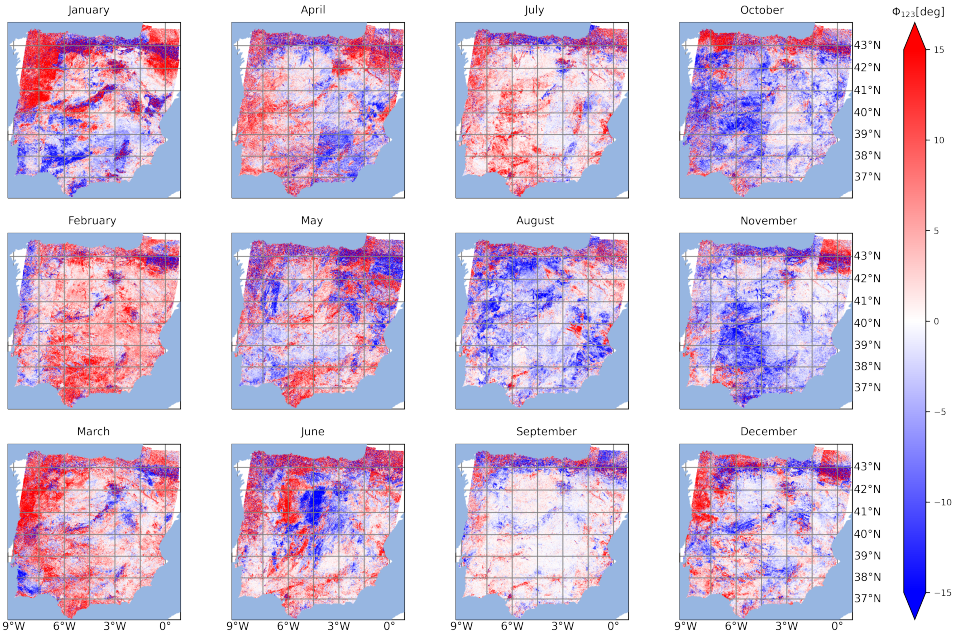

Figure 4.1: Individual closure phase examples for each month in 2017 constructed using 4 tracks of 6 a.m. (descending) VV polarized acquisitions, selected as the nearest in date to ensure full coverage of the Iberian Peninsula.

nitude due to the high phase noise level associated with low interferometric coherence over those areas.

2. Small closure phases in absolute terms are often large (> 2) in relative terms. In other words, the signal-to-noise of our closure phases remains high, even when the magnitude of the signal is small.

3. Some discontinuities at track edges are more pronounced in the significance ratio than in the closure phases themselves, for example, in September. This pattern shows that day-to-day variations affect not only the magnitude of closure phases but also the associated noise levels.

Figure 4.3 shows the corresponding three coherence values in an RGB composite (coh12=R, coh23=G, coh13=B) for each of the shown closure phase observations. This false color image effectively illustrates the variations between acquisitions. As expected, the red and green components, representing coherence between consecutive acquisitions, dominate most of the images. However, blue tones are also observed in some cases, such as in February and October, indicating a recovery of coherence over a 12-day interval. This behavior may be related to precipitation occurring between the acquisitions. Similar to the closure phase and significance ratio results, swath boundaries are also visible in the coherence RGB composite images, as adjacent swaths are acquired at different dates.

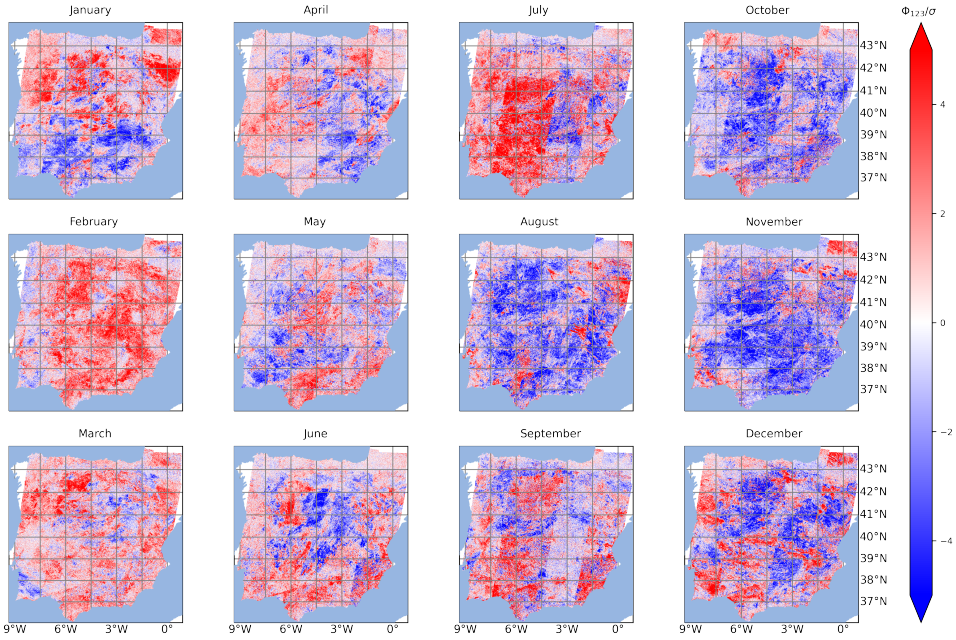

Figure 4.2: Individual significance ratio examples (correspond to Fig. 4.1) for each month in 2017 constructed using 4 tracks of 6 a.m. (descending) VV polarized acquisitions, selected as the nearest in date to ensure full coverage of the Iberian Peninsula.

4.2. SEASONAL MEAN CLOSURE PHASES

Figure 4.4 shows season-averaged closure phases for morning (a-b) and afternoon (c-d) tracks. Logically, temporal averaging leads to smaller closure phase values with spatial features apparently driven by land cover type and consistent across track boundaries. Positive mean closure phases predominate in spring and summer, while autumn shows mainly negative values. These patterns align with the dry and rainy seasons, respectively [55]. In winter, high-altitude regions exhibit high noise levels, likely due to snow, whereas other areas display positive mean closure phases. The spatial pattern of mean closure phases remains consistent for both VV (a and c) and VH (b and d) polarizations, with larger magnitudes in the VH-polarized case. The morning and afternoon acquisitions show similar spatial patterns, with two exceptions: in winter, the morning observations exhibit mainly positive closure phases in the southern peninsula, and in autumn, the afternoon acquisition display larger negative closure phases in the southwest coastal areas. The calculated seasonal mean value over a series of closure phases behaves as a random variable, with a mean and variance that mainly depend on local conditions (such as land cover, season, and day-to-day weather variations). The observed discontinuities at track edges result from having different realizations of this random variable, and the remaining randomness can be assessed by analyzing regions with acquisitions from overlapping tracks. When the mean value is calculated using data from multiple years, the track edges are expected to be negligible unless an angle-of-incidence effect is

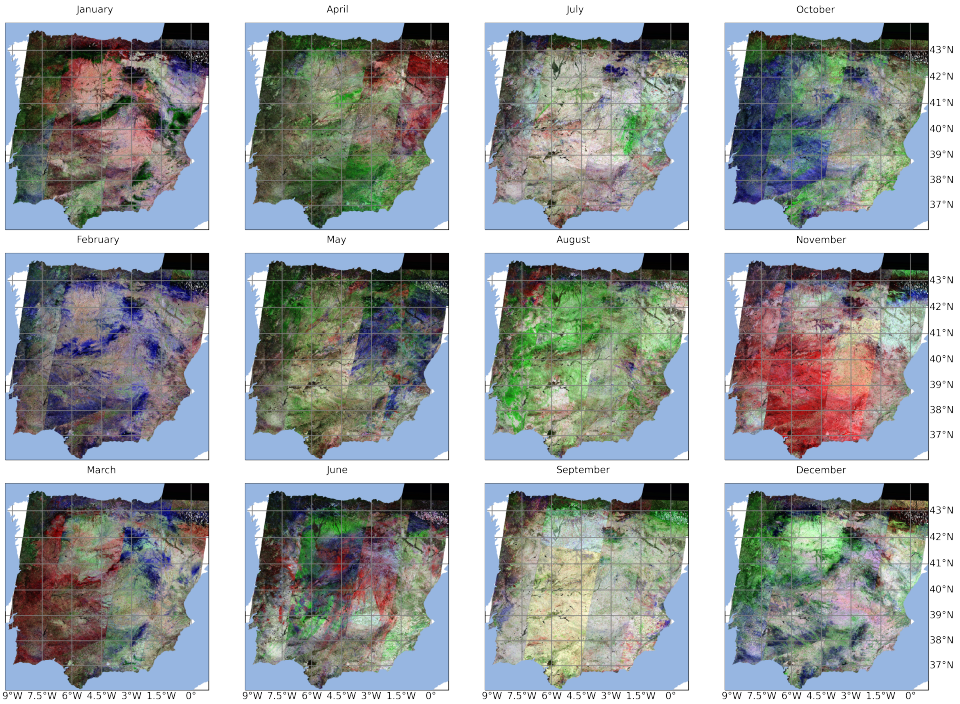

Figure 4.3: RGB composite (coh12=R, coh23=G, coh13=B) coherence examples (correspond to Fig. 4.1) for each month in 2017 constructed using 4 tracks of 6 a.m. (descending) VV polarized acquisitions, selected as the nearest in date to ensure full coverage of the Iberian Peninsula.

present.

We also present here the seasonal mean of soil moisture variation predicted closure phases in Figure 4.5. These predicted closure phases are calculated by feeding the soil moisture model (2.27) with the ERA5 hourly volumetric soil moisture measurements, corresponding to the SAR acquisition times of 6 a.m and 6 p.m for the descending and ascending passes, respectively. According to the results, the large-scale spatial patterns of the predicted closure phases show very limited resemblance to the observations. Despite this discrepancy, we observe some small-scale similarities. During the dry seasons, when the mean of observed closure phases are predominantly positive, the predicted closure phases show positive mean only in certain regions. In contrast, during the wet seasons, especially in autumn, the observed and predicted closure phases are more consistent, as negative mean values manifest across the entire study area in both cases. These results imply that, in certain periods and regions, soil moisture variation may not be the primary mechanism contributing to non-zero closure phases.

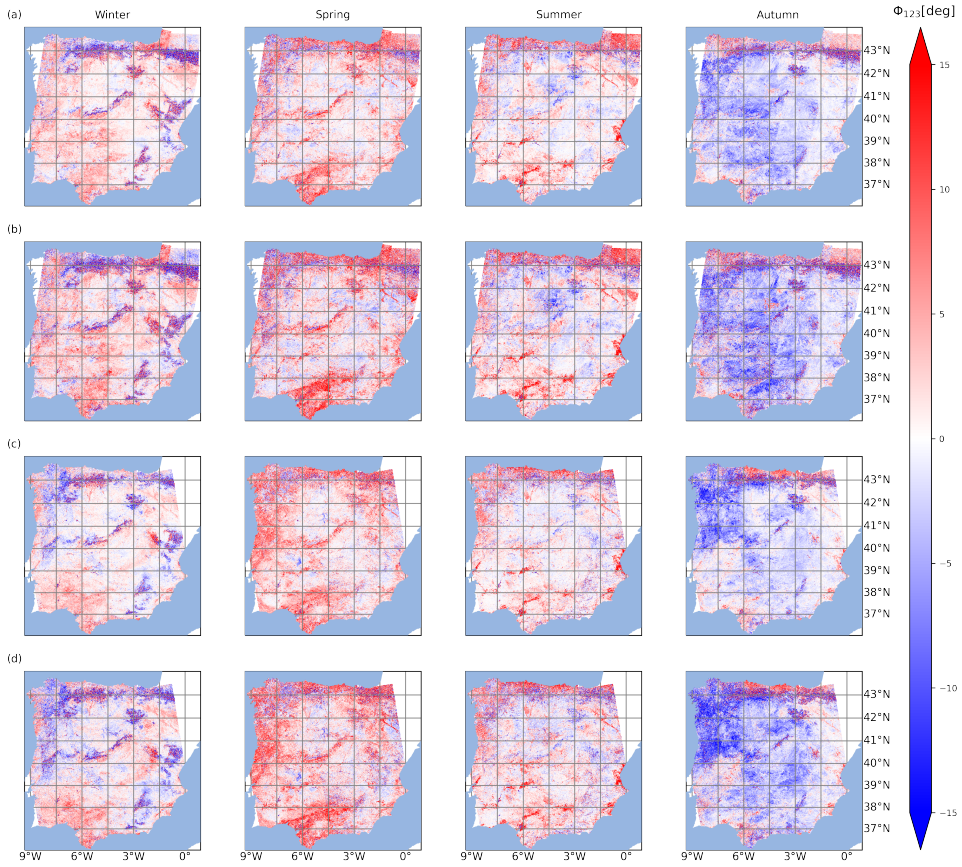

Figure 4.4: Seasonal mean of closure phases with (a) descending 6 a.m. VV polarized, (b) descending 6 a.m. VH polarized, (c) ascending 6 p.m. VV polarized and (d) ascending 6 p.m. VH polarized acquisitions.

4.3. SPATIOTEMPORAL MEAN CLOSURE PHASES

To study the temporal evolution of closure phases while minimizing phase noise, we compute spatial averages, along with the 10% and 90% percentiles, for cells exhibiting significant closure phases. For each epoch considered, we calculate these statistics over the four closest acquisitions in time to ensure complete area coverage. As the VV and VH observations exhibit similar behavior, we include only results for VV-polarized data to highlight the differences between morning and afternoon observations. The left panel of Figure 4.6 visualizes the time series of spatial mean closure phases. Both sets of observations exhibit similar magnitude in spatial mean closure phases. However, we observe a broader closure phase distribution in the afternoon acquisitions in spring and summer. We attribute this to environmental conditions, such as wind, which reduces coherence and tends to be more dynamic in the afternoon than in the early morning during warm seasons [56]. The mean values start near-zero in winter, gradually increase to approx-

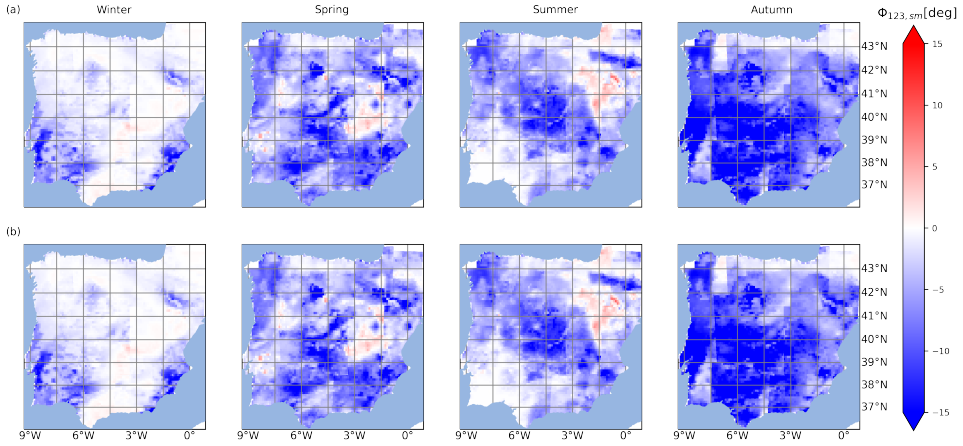

Figure 4.5: Seasonal mean of closure phases predicted by soil moisture variation using soil moisture measurements at the acquisition time correspond to (a) descending 6 a.m. and (b) ascending 6 p.m, respectively.

imately 8° by May, decrease to around −8° in early autumn, and then slightly increase back to near-zero by the end of the season. This temporal variation aligns with the sign changes in the temporal mean shown in Figure 4.4, where closure phases are mainly positive in spring and summer, negative in autumn, and mixed in winter. The right panel of Figure 4.6 shows the fraction of cells with significant closure phases, $|R_\Phi| > 1.96$, at each time stamp. At any given time, between 30% and 50% of the $7.5 \cdot 10^5$ cells evaluated exceed our significance threshold. As anticipated, lower coherence due to stronger temporal correlation during spring leads to a reduced rate of cells exceeding the significance threshold. In autumn, vegetation growth slows down or decays with decreasing temperature, scenes become more coherent, and more cells with significant closure phases are identified. From May to October, the morning acquisitions exhibit 5% more cells with significant closure phases. This signature provides additional confirmation of a more coherent scene in the early morning.

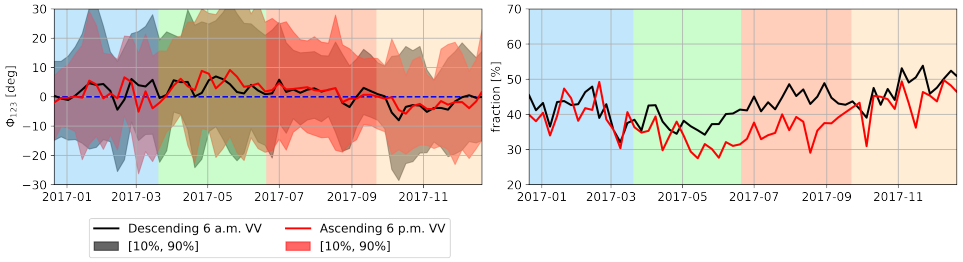

Figure 4.6: Spatial mean and percentiles of closure phase (left) and the fraction of cells with significant closure phases (right) in the entire research area. Background colors representing different seasons from left to right is winter, spring, summer, and autumn.

An information-richer scenario emerges when we consider these closure phase time series after averaging cells by land cover type and climate zone, as shown in Figure 4.7.

1. In forests, different climate zones do not appear to significantly affect the mean closure phases, possibly because the canopy conditions remain relatively stable, resulting in limited dielectric variation.

2. In croplands, which are artificially managed, the magnitudes of mean closure phases exhibit consistent patterns across different climate zones. In winter, croplands exhibit closure phases with narrow percentile bands, likely due to crop fields lying fallow after autumn harvest and being covered by bare soil instead of vegetation, which is generally more coherent. This also explains the higher survival fraction observed during autumn and winter.

3. Wild shrubs appear to be more sensitive to weather dynamics compared with forests and croplands, which are relatively resilient due to stable canopy conditions and artificial management, respectively. In the warm-summer Mediterranean (Csb) climate zone, their mean closure phases are consistently positive from the beginning of the year through to autumn. In contrast, in the subtropical highland (Cfb) climate zone, the mean closure phases vary over time, exhibiting a narrow distribution.

4. Herbaceous vegetation, unlike woody and branched vegetation types, has soft stems. In cold semi-arid (BSk) and Csb climate zones, the mean closure phases are positive in spring with low survival fractions. However, in hot-summer Mediterranean (Csa) and Cfb climate zones, the mean closure phases stay close to zero throughout the year. Meanwhile, in contrast to other vegetation, herbaceous vegetation shows a small difference in survival fraction between morning and afternoon acquisitions. These signatures imply that the branching structure of vegetation may play a role in its response to weather variations, potentially contributing to the noise level observed in the closure phases.

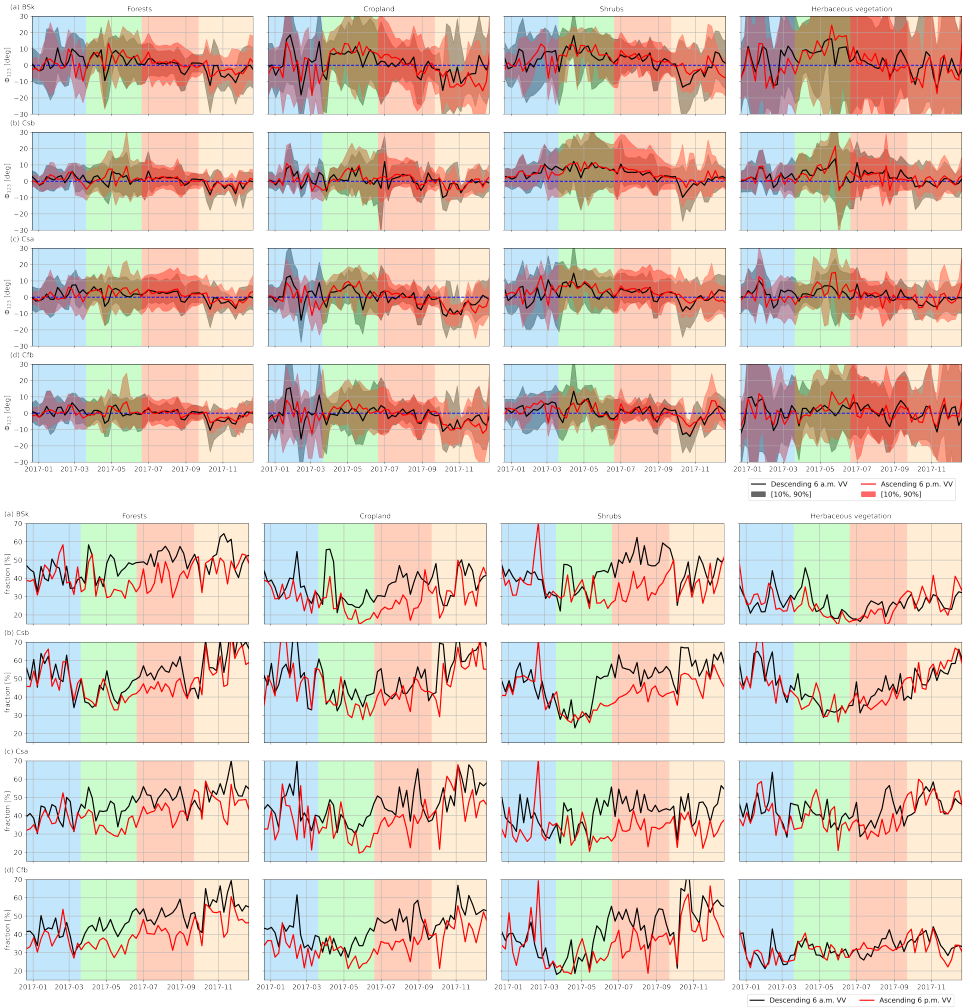

Figure 4.7: Upper panels: spatial mean and percentiles of closure phases in sub-regions categorized by land cover types and climate zones. Lower panels: fraction of cells with significant closure phases. In all both cases, the climate zones correspond to cold semi-arid (BSk) (a), warm-summer Mediterranean (Csb) (b), hot-summer Mediterranean (Csa) (c) and subtropical highland (Cfb) (d).

5

EXPLAINABLE CLOSURE PHASES

5.1. CORRELATION ANALYSIS BETWEEN CLOSURE PHASE OBSERVATIONS AND KNOWN MECHANISMS

To determine if the observed closure phases can be explained by specific mechanisms, we analyze the weighted Pearson correlation between the observed closure phases and two established mechanisms: soil moisture variation and volume scattering combined with perpendicular baselines [1, 2]. This weighted correlation test uses weights based on the estimated standard deviation from the numerical phase-noise model. For each sample in the dataset, the weight is

$$w_i = \frac{\frac{1}{\sigma_i}}{\sum_{i=0}^{N_c} \frac{1}{\sigma_i}}, \tag{5.1}$$

where N_c is the number of samples. In addition, as the correlation coefficients are affected by noise, and we have an estimation of the standard deviation of phase noise, we can compensate for this effect. Therefore, we estimate the correlation coefficient using

$$r = \frac{\text{cov}(x, y; w)}{\sqrt{(\text{cov}(x, x; w) - \sigma_{n,w}^2)\text{cov}(y, y; w)}}, \tag{5.2}$$

where $x = \Phi_{123,\text{obs}}$, $y = \Phi_{123,\text{mod}}$ represent the observed and modeled closure phases, respectively, $\text{cov}(x, y; w)$ is the weighted covariance, and

$$\sigma_{n,w}^2 = \frac{\sum_i w_i \sigma_i^2}{\sum_i w_i} \tag{5.3}$$

is the weighted phase noise variance [57]. The estimated correlation coefficient, r_P, is interpreted using the scale presented in Table 5.1.

Since whether or not two processes are correlated is independent of the method used to estimate the correlation coefficient, we use the p-value of the unweighted correlation

Table 5.1: The scale of Pearson correlation coefficient

Correlation coefficient r_P	**Indication**
$\|r_P\| < 0.2$	Very low correlation
$0.2 \leq \|r_P\| < 0.4$	Low correlation
$0.4 \leq \|r_P\| < 0.6$	Moderate correlation
$0.6 \leq \|r_P\| < 0.8$	High correlation
$0.8 \leq \|r_P\| \leq 1.0$	Very high correlation

as an inference for the estimated correlation coefficients for convenience. A lower p-value reflects a lower probability of obtaining test results at least as extreme as the result observed, assuming that the null hypothesis of no linear correlation is correct. We use a threshold p-value of 0.05, and compute the fraction of cells that survive this threshold. When more than 5% cells survive, we consider the estimated correlation coefficients trustworthy. For cells with relatively high correlation ($|r_P| > 0.65$) and low p-value, we present scatter plot examples comparing the observed closure phases with the modeled closure phases, along with the estimated slope and intercept. The correlation analysis for each considered mechanism is implemented as follows.

5.1.1. SOIL MOISTURE VARIATION INDUCED CLOSURE PHASES

We use the soil texture information, specifically the proportion of clay and sand particles, along with ERA5 hourly volumetric soil moisture measurements, as inputs to model the soil moisture variation induced closure phases (2.27). Both soil datasets are interpolated to match the grid of the SAR dataset, assuming that the coarse-resolution ERA5 soil moisture data is representative of a large area and that the heterogeneity in local soil moisture variation is negligible. This modeling approach combines a dielectric mixing model [50] with the interferometric soil moisture model [2].

Using the model output, we analyze the weighted Pearson correlation, r_P^{sm}, between the time series of observed and predicted closure phases. The resulting weighted correlation coefficients are presented in Figure 5.1. Apart from low correlation coefficients

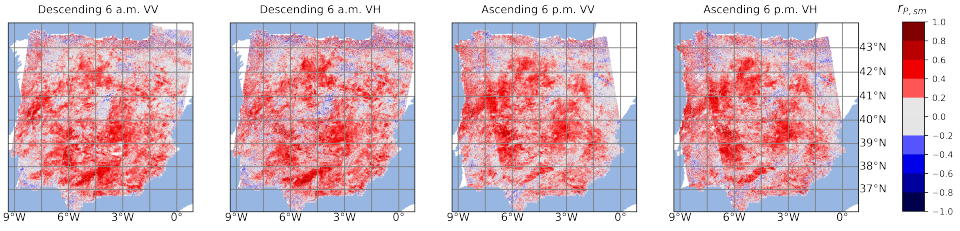

Figure 5.1: Weighted Pearson correlation coefficients between observed and soil moisture variation modeled closure phase time series.

($|r_{\mathrm{P,\,sm}}| < 0.20$) which are associated with high p-values, the remaining weighted correlation coefficients consistently exhibit low to moderate positive values across the peninsula, regardless of acquisition time and polarization. To some extent, the relatively low correlation coefficients can be explained by errors in the soil datasets, the limited spatial resolution of the ERA-5 soil moisture product, and the simplifications of the closure phases model. In general, we observe a good correlation during bare soil and low biomass periods, but a lower correlation in the presence of vegetation. Considering the fraction of samples that pass the 5% false alarm p-value masking across the entire research area, around 30% of closure phases cells show a significant linear correlation with soil moisture variation (34% in VV and 32% in VH at 6 a.m., 31% in VV and 29% in VH at 6 p.m.). Regardless of acquisition time, approximately 2% more cells exhibit significant correlation with soil moisture variation in the VV channel than in the VH channel. This difference likely reflects both the higher noise level in VH and the different sensitivities of the two channels to surface and volume scattering. In general, co-polarized signals have higher signal to noise ratio and are more sensitive to surface scattering, making VV a stronger indicator of soil moisture, whereas cross-polarized signals are noisier and more responsive to volume scattering, and therefore more sensitive to vegetation in vegetated areas.

As a complementary analysis, we estimate the parameters of a weighted linear regression, using the weights defined in (5.1). With the same notation as in (5.2), the slope of the weighted linear regression is computed as

$$P_{\mathrm{slope}} = \frac{\mathrm{cov}(\Phi_{123,\mathrm{obs}}, \Phi_{123,\mathrm{mod}}; w)}{\mathrm{cov}(\Phi_{123,\mathrm{mod}}, \Phi_{123,\mathrm{mod}}; w)}, \tag{5.4}$$

where $\Phi_{123,\mathrm{obs}}$ represents the closure phase observation, and $\Phi_{123,\mathrm{mod}}$ is the soil moisture variation predicted closure phases. Meanwhile, the intercept is derived by

$$P_{\mathrm{intercept}} = \overline{\Phi_{123,\mathrm{obs},w}} - \overline{\Phi_{123,\mathrm{mod},w}} P_{\mathrm{slope}}. \tag{5.5}$$

where $\overline{\Phi_{123,\mathrm{obs},w}}$ and $\overline{\Phi_{123,\mathrm{mod},w}}$ are weighted mean closure phases. The slope and intercept of the weighted linear regression, together with the previously computed weighted Pearson correlation coefficients, are illustrated in Figure 5.2. Correlation coefficients and slopes describe different attributes of two datasets, and therefore can take on any combination, such as a high slope with low correlation or a high correlation with a low slope. However, when using the same datasets, in which all points have the same noise level, regions with larger absolute slopes exhibit higher correlation coefficients. Therefore, the spatial pattern of the slope is consistent with that of the weighted Pearson correlation coefficients. If we assume that each geophysical component contributes independently to the closure phase and that the soil moisture model is complete, the slope would be expected to approach 1. However, as shown in Figure 5.2(a), the slope is largely suppressed, suggesting that the components in the closure phase model are not strictly additive. The intercept reflects a bias, indicating the presence of additional mechanisms not accounted for by the soil moisture model. Regions with higher intercept values generally coincide with areas of lower correlation. However, the spatial pattern of the intercept resembles that of the summer mean closure phases, shown in Figure 5.3, especially in vegetated areas. This similarity points to seasonal mechanisms, such as vegetation

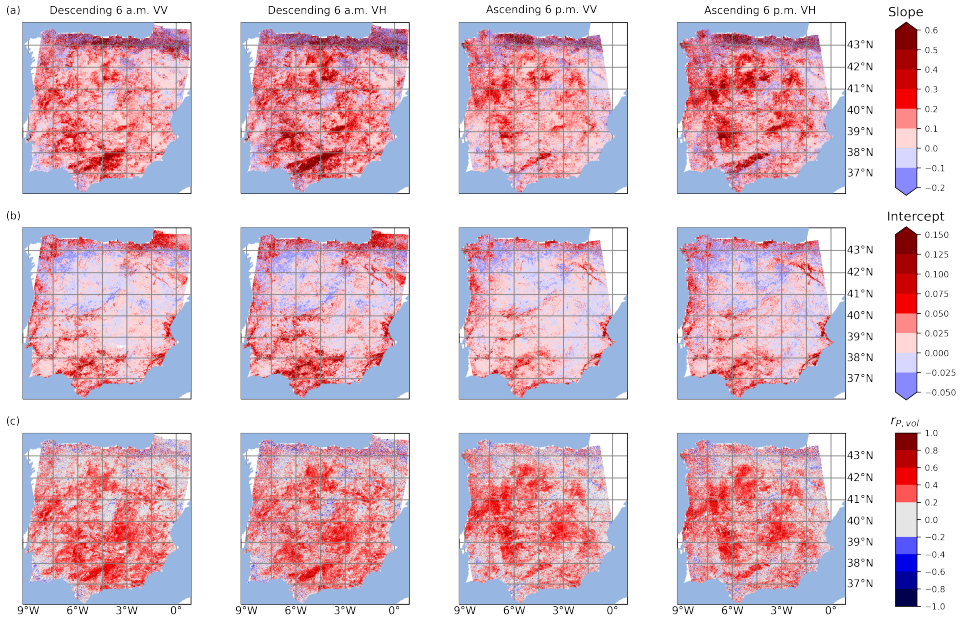

Figure 5.2: Weighted linear regression parameters (a) slope and (b) intercept, and (c) weighted Pearson correlation coefficients between observed and soil moisture variation modeled closure phase time series.

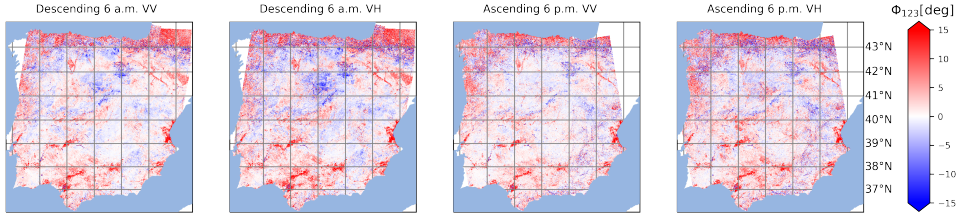

Figure 5.3: Summer mean of closure phases with (a) descending 6 a.m. VV polarized, (b) descending 6 a.m. VH polarized, (c) ascending 6 p.m. VV polarized and (d) ascending 6 p.m. VH polarized acquisitions.

growth during summer, that influence closure phases but are not explainable by soil moisture variations alone.

For sub-regions categorized by land cover type and climate zone, the distribution of correlation coefficients and the fraction of samples passing the p-value masking are detailed in Figure 5.4 and Table 5.2. The distribution of correlation coefficients further demonstrates the presence of a positive correlation, where mean values are consistently positive, with magnitudes around 0.20. Across all sub-regions, we observe similar correlation levels (≈ 0.2). This is even the case in forested areas, where no correlation is expected due to the dense above-ground biomass that largely suppresses surface scattering and, therefore, the soil-moisture-related contributions to the closure phase. The similar correlation levels in forests, as seen in other areas, are likely driven by two pos-

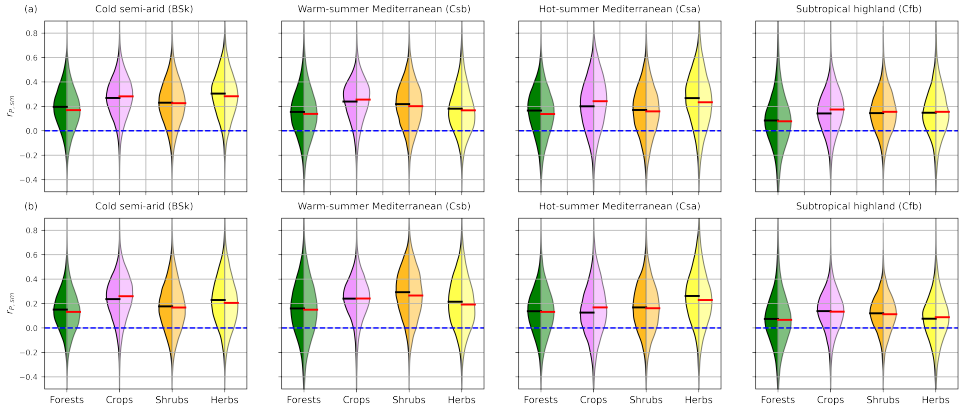

Figure 5.4: Weighted Pearson correlation coefficients between observed and soil moisture variation modeled closure phase time series in sub-regions categorized with land cover type and climate zone: (a) 6 a.m. descending acquisition VV (right) & VH (left) and (b) 6 p.m. ascending acquisition VV (right) & VH (left).

5

sible factors. First, both vegetation water content and soil moisture respond to environmental forcings such as temperature variations and precipitation. Second, there is a coupling effect between water content variations in the canopy and in the soil [58, 59]. In non-forest areas, the ranking of correlation varies by climate zone. For instance, croplands and herbaceous vegetation show the highest correlation in the cold semi-arid (BSk) climate zone, with a similar mean value of 0.30. In the subtropical highland (Cfb) climate zone, non-forest areas show comparable levels of linear correlation. These land-cover-related differences suggest that different vegetation types respond differently to weather dynamics. This statistical variation also appears in the fraction of grid cells passing the p-value filtering. In BSk, warm-summer Mediterranean (Csb), and Csa climate zones, over 20% of grid cells exhibit a statistically significant linear relationship with soil moisture variation. However, in the Cfb climate zone, located in the northern mountainous part of the peninsula, confidence in the estimated correlation is lower.

To provide further insight into how well the model predicts the observed closure phases, Figure 5.5 shows example scatter plots, with the predicted and observed closure phases in the horizontal and vertical axes, respectively. These examples correspond to high correlation cases for the different combinations of land cover and climate zone. Each subplot in the figure is annotated with the weighted Pearson correlation coefficient for VV and VH polarized data, and the corresponding p-values. In addition, we have overlaid a first-order weighted linear regression and the corresponding parameters. For each selected cell, the equivalent number of looks is around 10^3. Comparing correlation coefficients for the same point across different polarizations reveals that a very high linear correlation ($|r_P| > 0.8$) in one polarization does not necessarily correspond to a similar level of correlation in another polarization. Despite differences in the level of correlation, the estimated slopes are consistently positive and widely observed. The varying patterns in the scatter plots indicate that local climate and land use conditions affect closure phase behavior and its correlation with soil moisture variations.

Table 5.2: Weighted Pearson correlation between observed and soil moisture modeled closure phases: fraction surviving 0.05 p-value masking

Time	VV	VH	Climate	Forests	Croplands	Shrubs	Herbaceous vegetation
6 a.m.	✓	-	BSk	38%	47%	45%	56%
6 a.m.	-	✓	BSk	32%	51%	41%	47%
6 p.m.	✓	-	BSk	27%	40%	33%	41%
6 p.m.	-	✓	BSk	25%	44%	32%	35%
6 a.m.	✓	-	Csb	24%	44%	42%	27%
6 a.m.	-	✓	Csb	20%	42%	33%	20%
6 p.m.	✓	-	Csb	31%	40%	57%	37%
6 p.m.	-	✓	Csb	25%	39%	45%	26%
6 a.m.	✓	-	Csa	35%	36%	33%	51%
6 a.m.	-	✓	Csa	30%	41%	30%	38%
6 p.m.	✓	-	Csa	26%	29%	32%	49%
6 p.m.	-	✓	Csa	23%	31%	27%	32%
6 a.m.	✓	-	Cfb	14%	25%	23%	16%
6 a.m.	-	✓	Cfb	13%	30%	23%	15%
6 p.m.	✓	-	Cfb	12%	24%	16%	9%
6 p.m.	-	✓	Cfb	11%	23%	14%	9%

5.1.2. VOLUME SCATTERING INDUCED CLOSURE PHASES

We evaluate the potential relationship between volume scattering combined with varying perpendicular baselines and the observed closure phases, treating the third central moment of the scattering profile in (2.30) as a scaling factor. Because of this simplification, we do not expect an exact match between the predicted and observed closure phases, instead, we expect a correlation between them. We calculate the differential vertical wavenumber triplets, $\kappa_{123} = \kappa_{z1z2}\kappa_{z2z3}\kappa_{z3z1}$, to predict the closure phases induced by volume scattering. Each κ is a function of the perpendicular baseline $B_\perp$ within a resolution cell,

$$\kappa = \frac{4\pi B_\perp}{\lambda R \sin\theta_i}, \tag{5.6}$$

where $\lambda \approx 5.55$ cm is the wavelength of the Sentinel-1 signal, R represents the one-way range and θ_i is the incident angle.

We assess the weighted Pearson correlation coefficient, $r_{\mathrm{P,vol}}$, between the observed closure phase and modeled closure phases derived from the volume scattering mecha-

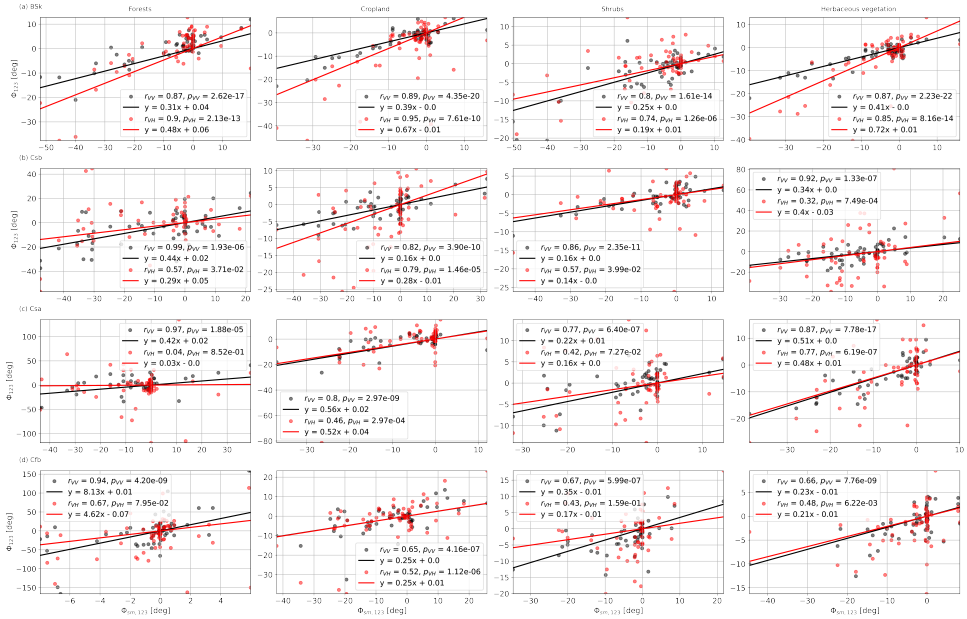

Figure 5.5: Examples in each subregion show relatively high correlation between closure phase observations and soil moisture variation modeled closure phases in (a) cold semi-arid (BSk), (b) warm-summer Mediterranean (Csb), (c) hot-summer Mediterranean (Csa) and (d) subtropical highland (Cfb).

nism using (2.30). As shown in Figure 5.6, the estimated correlation coefficients, $|r_{\mathrm{P,vol}}| < 0.40$, are low with varying signs. Instances of relatively high correlation can be attributed

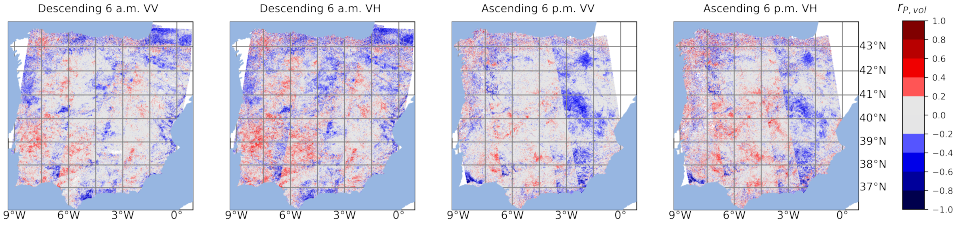

Figure 5.6: Weighted Pearson correlation coefficients between observed and vertical wavenumber variation modeled closure phase.

to spurious correlation between variations in perpendicular baseline and other geophysical changes, such as soil moisture variation, as shown in Figure 5.7. The distribution of estimated correlation coefficients in Figure 5.8 shows a normal distribution with a mean value near zero across all land cover types, suggesting that perpendicular baseline variations have minimal impact on closure phases. This is further supported by the fraction of grid cells passing the p-value threshold, as shown in Table 5.3. In cropland, the surviving fraction barely exceeds 5%, while in forests and shrubs regions, it is around 10%. This difference can be attributed to topography: crop fields are typically in flatter areas,

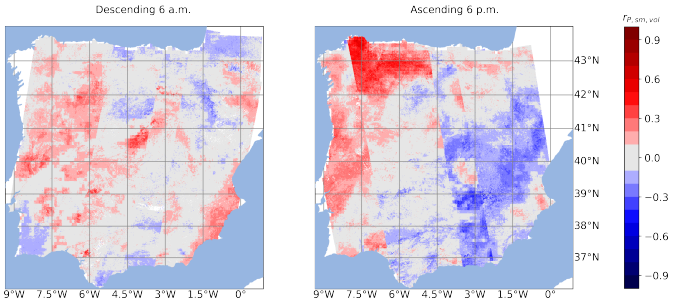

Figure 5.7: Weighted Pearson correlation coefficients between soil moisture variation and vertical wavenumber variation modeled closure phase.



Figure 5.8: Distribution of weighted Pearson correlation coefficients between observed and perpendicular baseline modeled closure phase time series: left half represents VV polarization and right half represents VH polarization.

Table 5.3: Weighted Pearson correlation between observed and perpendicular baseline modeled closure phases: Fraction surviving 0.05 p-value masking

Acquisition	Polarization	Total	Forests	Crops	Shrubs	Herbs
6 a.m.	VV	8%	10%	7%	12%	8%
6 a.m	VH	9%	10%	8%	12%	8%
6 p.m.	VV	8%	9%	6%	12%	7%
6 p.m.	VH	8%	9%	7%	12%	8%

whereas other vegetation types are more widely distributed. Since we do not observe significant number of grid cells passing the 5% false alarm threshold, we exclude further detailed analysis of this correlation coefficient.

Although the distribution of weighted Pearson correlation coefficients indicates the contribution from the volume scattering mechanism to geophysical closure phases is negligible, examples in Figure 5.9 illustrate cases of high linear correlations. In contrast to the consistent positive correlation with soil moisture variation, the sign of linear correlation coefficient varies when correlating the observed with the modeled closure phase using perpendicular baseline variation. We visualized scatter plot examples showing

Table 5.4: Example points exhibit very high weighted Pearson correlation between observed and volume scattering modeled closure phases

Acquisition	Land cover	Climate	Latitude	Longitude
6 a.m. (a)	Cropland	BSk	38.65°N	4.14°W
6 a.m. (b)	Herbaceous vegetation	BSk	38.66°N	4.14°W
6 p.m. (c)	Shrubs	BSk	38.66°N	4.13°W
6 p.m. (d)	Herbaceous vegetation	BSk	37.63°N	3.05°W
6 a.m. (e)	Herbaceous vegetation	Csb	42.74°N	6.22°W
6 a.m. (f)	Shrubs	BSk	36.84°N	3.01°W
6 p.m. (g)	Forests	Csa	37.63°N	6.47°W
6 p.m. (h)	Forests	Csa	37.27°N	4.27°W

both very high positive (upper panel) and very high negative (lower panel) correlations. Detailed information for each example cell with ENL around 10^3 is summarized in Table 5.4. According to the locations of cells with very high positive correlation, as shown in Figure 5.10, three of them (Figure 5.9 (a), (b), and (c)) are situated close to each other in a mining basin, where vegetation has been removed, and the land cover map misses to capture this artificial activity. The fourth point (Figure 5.9 (d)) and selected points with very high negative correlation are distributed in mountainous regions, except for cell (e), which is located in a different mining basin. This distribution in areas with complex topography, suggesting that the digital elevation model (DEM) is outdated, failing to include recent artificial activities and lacking the resolution to capture complex to-

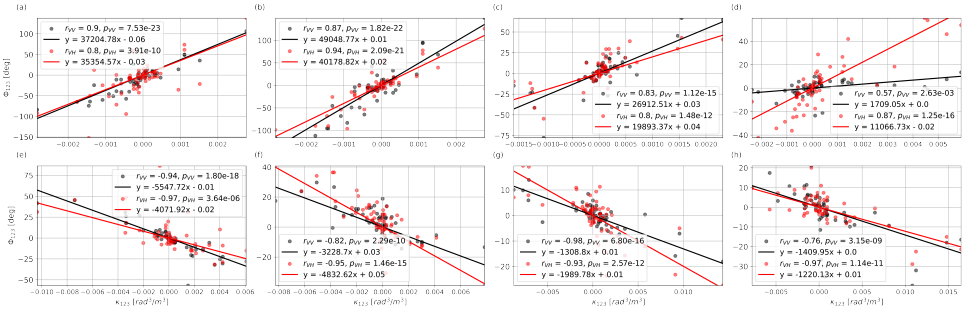

Figure 5.9: Time series which show very high correlation between closure phase observations and perpendicular baseline variation modeled closure phases: (a) positive 6 a.m. descending VV polarized, (b) positive 6 a.m. descending VH polarized, (c) positive 6 p.m. ascending VV polarized, (d) positive 6 p.m. ascending VH polarized, (e) negative 6 a.m. descending VV polarized, (f) negative 6 a.m. descending VH polarized, (g) negative 6 p.m. ascending VV polarized and (h) negative 6 p.m. ascending VH polarized acquisitions.

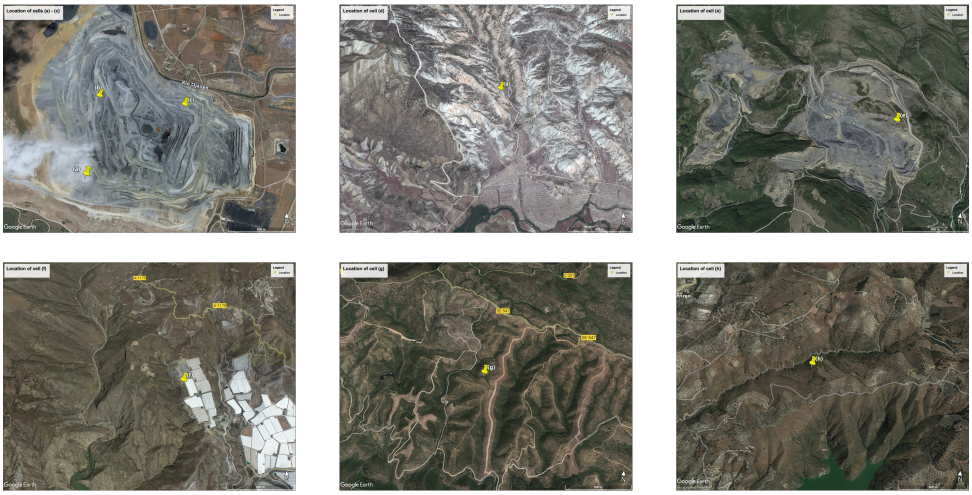

Figure 5.10: Google Earth Pro imagery showing the locations of example cells that exhibit high correlation with perpendicular baseline variations. First row from left to right: locations of cell (a)-(c), (d) and (e). second row from left to right: locations of cell (f), (g) and (h).

pography in mountainous regions. Therefore, the very high correlation between the closure phase and perpendicular baseline variations may emerge because the topographic phase is not completely removed by flattening in the data processing.

5.2. VARIANCE IN CLOSURE PHASES

5.2.1. EXPLAINABLE VARIANCE

Explainable variance allows us to quantify the contributions of different components to closure phases at a statistical level. We calculated the total standard deviation for a given dataset and analyzed the variance fractions from three components: phase noise, soil moisture variations, and volume scattering. By summing the explainable variance from these three components, we can quantify the total explainable variance in our observations, regardless of the correlation between each contributor.

Considering the phase noise component, our numerical model in section 3.4.2 provides the expected variance in closure phases due to phase noise. Using the noise-originated variance, σ^2, we can compute its fraction of the total variance, σ_t^2, using the error propagation law. Therefore, for each point in a dataset with N_c samples, the fraction is given by

$$r_n^2 = \frac{1}{\sigma_t^2} \frac{\sum_{i=0}^{N_c} (N_{l,i} \sigma_i^2)}{\sum_{i=0}^{N_c} N_{l,i}}, \tag{5.7}$$

where N_l is the ENL. Under the assumption that the ENL for each point in the time series is the same, and given the variance of a time series, σ_t^2, the computation of the explain-

able variance of the noise component, r_n^2, simplifies to

$$r_n^2 = \frac{1}{\sigma_t^2} \frac{\sum_{i=0}^{N_c} \sigma_i^2}{N_c}. \tag{5.8}$$

For geophysical components, we assess the corresponding explainable variance using the coefficient of determination (R-squared score), r^2, defined as the square of Pearson correlation, $r^2 = r_P^2$. Given the noise level of each sample, we applied the weighted Pearson correlation, as discussed in the previous subsection, to calculate the R-squared score.

We analyze the fraction of explainable variance for the closure phase by considering the following contributions:

1. phase noise contribution associated with the interferometric coherence estimates;
2. the fraction of the variance that we can explain by soil moisture variations, r_{sm}^2;
3. and the sum of known mechanisms $r_{\mathrm{n}}^2 + r_{\mathrm{sm}}^2 + r_{\mathrm{vol}}^2$.

We do not discuss separately the individual contribution associated with perpendicular baselines and volume scattering, as it is, in general, very small.

Figure 5.11 visualizes the total standard deviation (left column), along with these three explainable variance ratios. Most areas show a standard deviation below 10 degrees, except for mountainous and densely vegetated regions, where the coherence is low, with standard deviation exceeding 20 degrees. The noise component, r_n^2, indicates that interferometric coherence is generally lower at VH than at VV, as expected. Additionally, its spatial pattern reveals a link with land cover. For land covers linked to low coherence, such as mountainous or densely vegetated regions, the resulting phase noise explains most of the variance ($r_{\mathrm{n}}^2 \geq 0.7$). However, cropland regions often exhibit low explainable variance ($r_{\mathrm{n}}^2 < 0.2$). The explainable variance due to soil moisture variation, r_{sm}^2, varies with the time of the day. For morning acquisitions, more variance is explained in the south of the peninsula, which is situated in the hot-summer Mediterranean (Csa) and cold semi-arid (BSk) climate zones. In afternoon acquisitions, higher variance is explained around the northwest coast of the peninsula, located in the warm-summer Mediterranean (Csb) climate zone. The total explainable variance indicates that in high-variance regions, more than 70% of the variance can be attributed to phase noise. In other areas, the explainable variance ranges from 40% to 60%, depending on polarization and land cover types.

Figure 5.12 shows the distribution of each R-squared score component for the entire research region and sub-regions categorized by land cover type. Regarding the soil moisture variation mechanism, the mean values account for about 10% of the variance in closure phases time series. For different land cover types, soil moisture variation explains more signal in cropland, herbaceous vegetation, and shrubs than in forests. This signature again relates to the density of the above-ground biomass, with forests having the highest density, which attenuates more C-band signals. Overall, the highest level of signal explanation is found in forests, followed by herbaceous vegetation, shrubs and cropland, with differences in mean R-squared scores mainly driven by variations in the

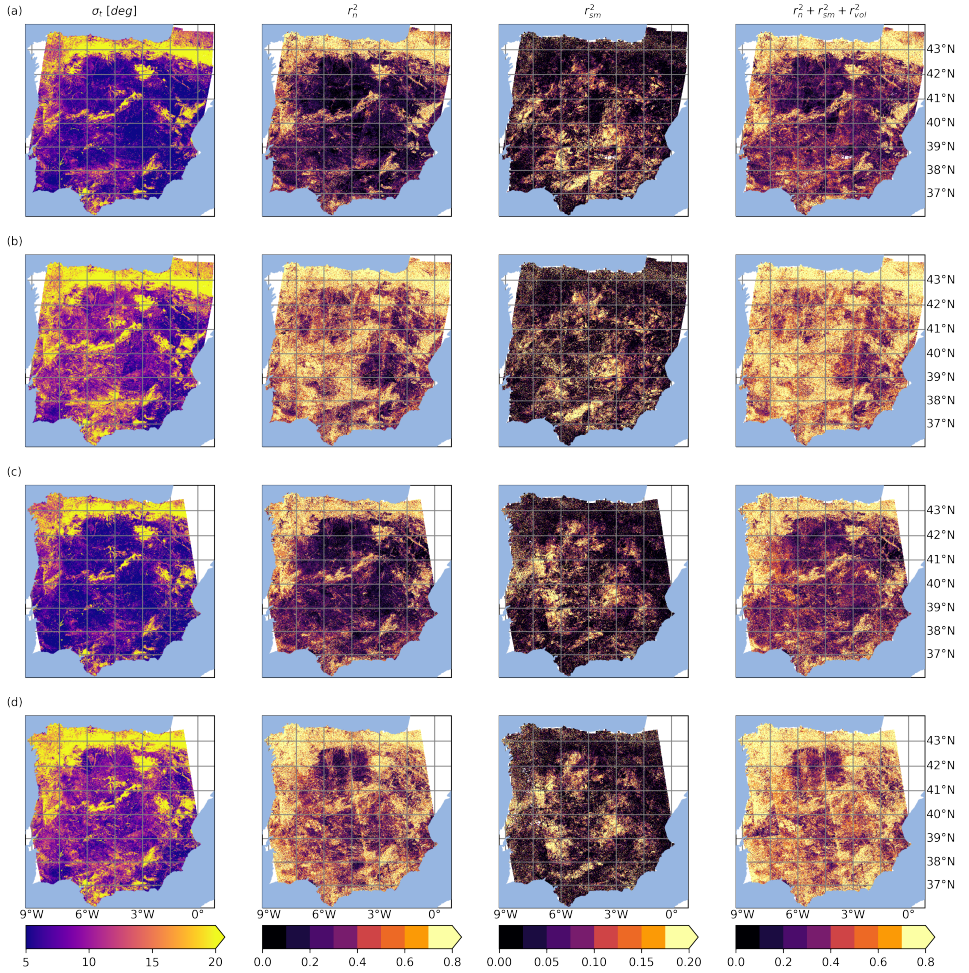

Figure 5.11: From left to right: temporal standard deviation σ_t, the explainable variance by phase noise r_n^2, by soil moisture variation r_{sm}^2 and by total known mechanisms $r_n^2 + r_{sm}^2 + r_{vol}^2$ with (a) 6 a.m. descending VV polarized, (b) 6 a.m. descending VH polarized, (c) 6 p.m. ascending VV polarized and (d) 6 p.m. ascending VH polarized acquisitions.

noise component. In conclusion, known mechanisms account for about 40% of the total variance, although most of the observed signal remain unexplained.

5.2.2. UNEXPLAINED VARIANCE

There are two main possible explanations for the low fraction, approximately 40%, of total explainable variance. One relates to errors in estimating the contributions of the considered mechanisms, while the other, more fundamental explanation involves additional, unaccounted-for sources contributing to the geophysical closure phases, particularly in areas with dense biomass.

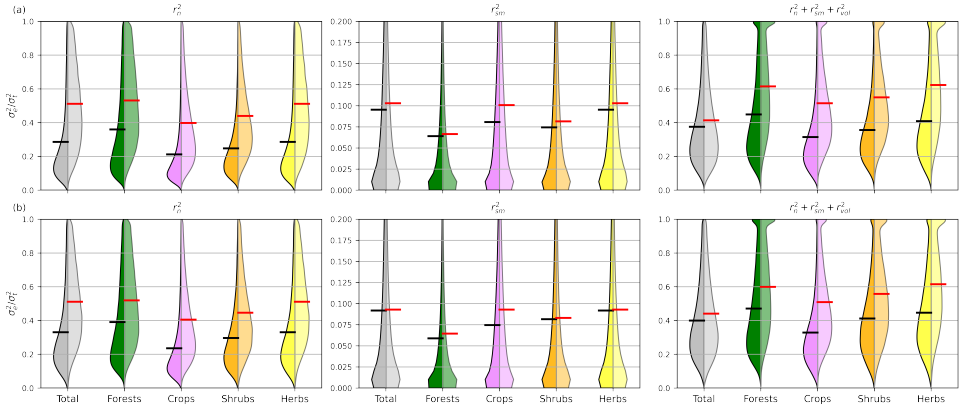

Figure 5.12: The distribution of R-squared score, σ_e^2/σ_t^2, with (a) 6 a.m. descending VV (left) and VH (right) polarized and (b) 6 p.m. ascending VV (left) and VH (right) polarized acquisitions.

ESTIMATION ERROR

Considering estimation errors, this category can be further classified into three types: underestimation of phase noise, oversimplification of geophysical models, and the limited representativeness of correlation coefficients. Firstly, phase noise, estimated using the numerical model with coherence as a primary input, may be underestimated, particularly in regions of very low coherence, where coherence itself tends to be overestimated [23]. Secondly, in modeling closure phases from geophysical variations, we acknowledge the inherent incompleteness of the geophysical models and further simplified their implementation for practical reasons. For modeling the contribution from the soil moisture variation mechanism, we treated the soil as a uniform dielectric medium and used coarse-resolution soil moisture measurements, with limited representativity at 1 km × 1 km resolution and significant uncertainties, especially at local scales, as model inputs. We estimated the error introduced by this approach using the first-order second-moment method, assuming a soil moisture product error standard deviation of 0.019 [60]. The resulting distribution of the error in the predicted closure phases has a mean of 3.44 degrees and a standard deviation of 26.36 degrees. Although this bias contributes little to the explainable variance, a higher-resolution soil moisture product that better matches the resolution of the SAR dataset and a more comprehensive model have strong potential to improve the accuracy of estimating the contribution of soil moisture variation to the observed closure phases. For modeling the contribution of volumetric scattering in combination with the perpendicular baseline, we assumed a constant unknown vertical scattering profile in time, considering only the variation introduced by changes in the perpendicular baseline. Although we confirmed that the contribution of this component is minimal, a more comprehensive implementation of the model incorporating non-constant scattering coefficient statistics would likely improve estimation accuracy. Thirdly, the Pearson correlation analysis is conducted under the assumption that the model fully captures the relevant processes and evaluates only the linear relationship between the modeled and observed closure phases, thereby overlooking both the in-

completeness of the model and potential coupling effects among multiple contributing sources.

POTENTIAL NEW GEOPHYSICAL PROCESSES

Regarding the more fundamental contributor to the low explainable variance, unaccounted geophysical sources contributing to the closure phases, we selected two cropland sites located in the cold semi-arid (BSk) and the Mediterranean (Csa) climate zones, respectively, where the unexplained variance exceeds 0.8, and conducted case studies. For the selected regions, we use afternoon co-polarized observations and visualize the mean and percentiles of both the observed and soil moisture variation predicted closure phases in Figure 5.13. In these time series, the closure phases predicted from soil

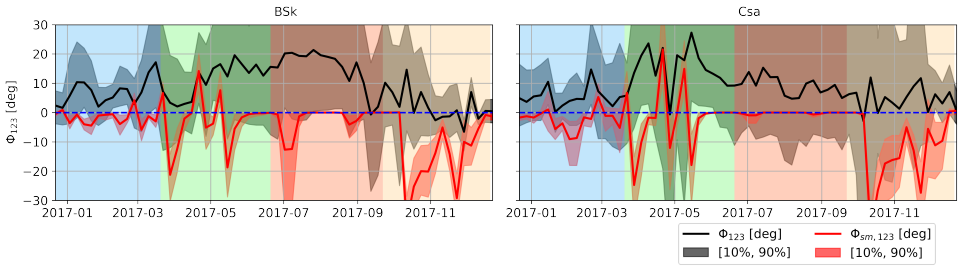

Figure 5.13: Spatial mean and percentiles of observed and soil moisture variation predicted closure phases time series examples for selected cropland sites in the BSk and Csa climate zones, respectively, where the unexplained variance exceeds 0.8.

moisture variations do not resemble the observed closure phases throughout the year, in some cases, the model even predicts closure phases with opposite signs. This discrepancy is particularly pronounced during late spring and summer, where both croplands show positive mean closure phases around 15° from May to September. This period generally coincides with the peak of vegetation growth, suggesting that biomass evolution may be the dominant component within a resolution cell.

To better illustrate unexplained signals exhibiting seasonal behavior, we processed a three-year data stack over a smaller region, focusing on corn fields near Santa Amalia, Spain, where the annual mean closure phases are consistently positive, as shown in Fig. 5.14. For cells exhibiting statistically significant closure phases across the entire field, the corresponding three-year closure phase time series for this corn field are presented in Fig. 5.15. This example clearly indicates that seasonal effects can be more effectively examined in spatially homogeneous areas. Consequently, it is challenging to isolate seasonal signals from time series covering large regions with mixed geophysical conditions.

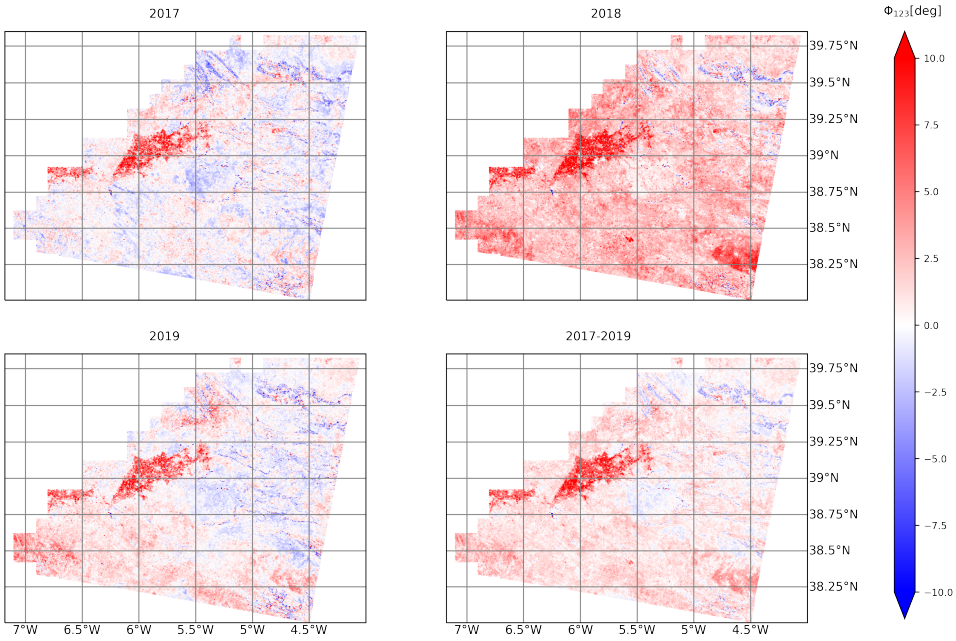

Figure 5.14: Mean closure phases in 2017, 2018, 2019, and from 2017 to 2019.

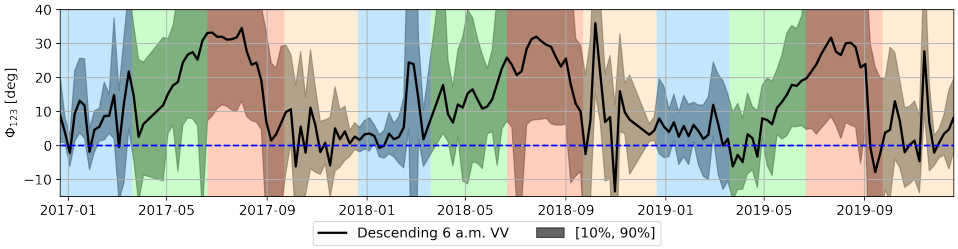

Figure 5.15: Spatial mean and percentiles of observed significant closure phases time series for corn field near Santa Amalia, Spain.

6

VEGETATION DYNAMICS RELATED CLOSURE PHASES

When we look at the closure phase statistics, we find regions with consistently positive mean closure phases. One particularly striking example is the El Ejido greenhouses. This observation prompted a closer inspection of other areas exhibiting similar statistical behavior, leading to the identification of several heavily vegetated regions in southern Spain. To investigate in detail the relationship between positive mean closure phases and vegetation, and to examine how persistent positive closure phases occur during periods of peak biomass growth across different vegetation types, explicit case studies at local scales are essential. Therefore, in this chapter, we examine closure phase observations over specific crop fields under controlled environments and explore potential physical explanations for the observed signatures.

6.1. RESEARCH AREA

To define the case study regions, we focus on areas exhibiting persistent positive closure phases over time. According to the seasonal mean shown in Figure 4.4, several regions show consistent positive closure phases during spring and summer, which correspond to the peak biomass development periods for most vegetation. Zooming in on southern Spain, where multiple clusters of seasonal positive closure phases are observed, and examining the annual mean as shown in Figure 6.1, it is evident that positive closure phases persist in specific regions throughout the year. Using Google Maps imagery and land usage data from the *Sistema de Información Geográfica de Parcelas Agrícolas* (SIGPAC), we identified these regions as agricultural areas, including two open crop field zones and one greenhouse-dominated region. The open crop fields considered include corn fields (39°N, 6°W) located around the town of Santa Amalia and citrus fields (37.7°N, 5.5°W) situated in the upper Guadalquivir valley. The greenhouse region (36.7°N, 2.7°W) is located in the province of Almería where the greenhouse concentration is very high.

Although these three areas are all artificially controlled croplands, they differ in their

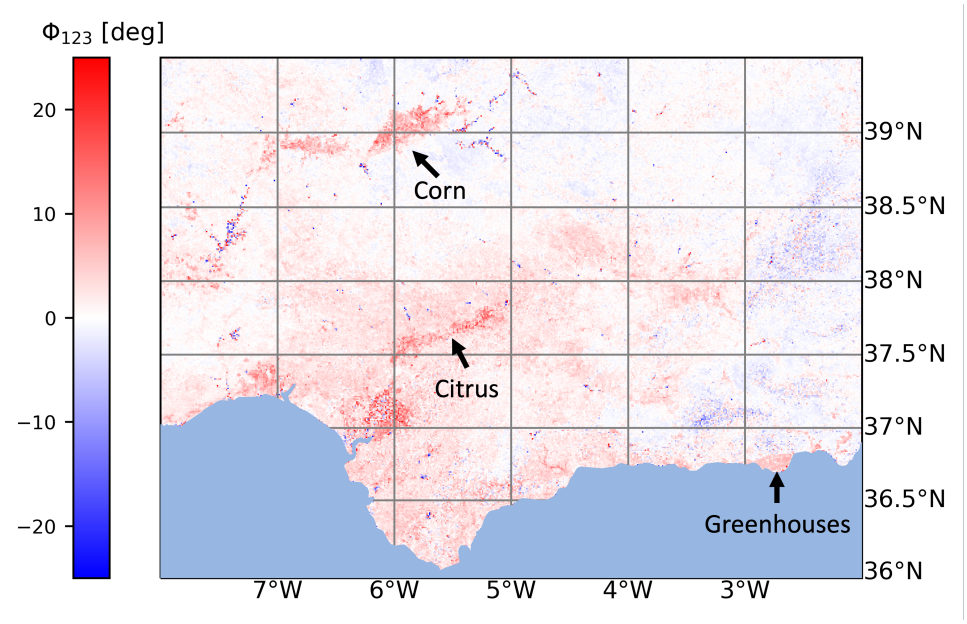

Figure 6.1: VV polarized temporal mean closure phases over southern Spain in 2017

physical properties, not only in terms of crop types but also in the management practice applied. The corn field is an open area where annual crops are planted in spring and harvested in autumn each year. In between growing seasons, the fields go through a rest period during which the soil is left bare. In contrast, citrus orchards consist of evergreen trees that are cultivated over multiple years and were already planted before the study period, 2017. As a result, there is no bare soil phase in these fields. Instead, the observed changes are mainly due to canopy development, particularly the growth of the fruits. Greenhouses are structures designed to support year-round crop cultivation by regulating environmental factors such as temperature, humidity, and light. As a result, within greenhouses, the peak biomass development periods often differ from those of open crop fields. Serving as a special case, the greenhouses study offers valuable insights into the relationship between closure phases and vegetation growth.

6.2. DATA

The goal of the case study shifts from statistical analysis to exploring the relationship between closure phases and geophysical parameters associated with vegetation phenology at local scales. Therefore, based on the identified research areas, we use only a small subset of the Sentinel-1 SAR dataset. We use the 6 p.m. ascending observations from two different tracks, track 1 and track 74, which provide the full coverage for each of our areas of interest, the open crop regions and the greenhouses area. For each region, the corresponding Sentinel-1 track number and the dynamic range of the incident angle, from the near range to far range based on the extend of the region, are summarized in

Table 6.1. Furthermore, in addition to the geophysical datasets introduced in Chapter 3,

Table 6.1: Sentinel-1 Geometry Information for each field.

Crop field	Sentinel-1 pass	Incident angle
Corn fields	Ascending track 74	[34.02°, 38.83°]
Citrus fields	Ascending track 74	[30.57°, 42.13°]
Greenhouses	Ascending track 1	[37.77°, 43.82°]

more geophysical datasets are incorporated to support the interpretation of radar observations. The additional geophysical datasets include detailed land use information, precipitation records, and the Leaf Area Index (LAI) product. Except for the SIGPAC land use shapefiles, which correspond to 2017, the rest of the datasets are from the time window 2016-12-10 to 2018-01-10 with different temporal and spatial resolutions, as summarized in Table 6.2.

As the scale of each research area is small, the effect of biases introduced by mixing cells with different physical properties while multilooking is not negligible. Therefore, more detailed land information is essential to reduce the probabilities of mixing multilooked cells from different land cover conditions. We use SIGPAC shapefiles to aid in the selection of multilooking candidates with polygons for each research region [61]. Compared to the CGLS land cover map, which provides a single class for all cropland across the entire Iberian Peninsula, the SIGPAC land use product registers the up-to-date crop type for each individual field. These detailed land use polygons allow us to further identify multilooking cells within the roughly identified crop fields, which are circled using the positive annual mean closure phases.

Although the focus of this study is on the relationship with vegetation parameters, the contribution from soil moisture variations, which are highly correlated with precipitation events, cannot be ignored. Leaving aside the case where C-band radar can penetrate through vegetation under certain conditions and reach the surface, in croplands, fields often undergo a period of rest before sowing, and crops are typically widely spaced. In both cases, only bare soil remains in the field, with soil moisture variation becoming the main contributor to closure phase variations. Therefore, we include daily precipita-

Table 6.2: Information for each dataset.

Dataset	Temporal resolution	Spatial resolution	Source
Land usage	1-year	-	Junta de Andalucía
Precipitation	1-day	-	Visual Crossing Corporation
Sentinel-3 LAI	10-day	300 m	Copernicus Global Land Service

tion data provided by Visual Crossing Corporation weather records [55] to investigate its effect on radar observables. Due to the limited number of weather stations, precipitation records are only available for certain locations. For each crop field, we select the records from the nearest weather station to the fields.

In order to relate the closure phase signatures to vegetation development, we need a parameter that quantifies the condition of vegetation. Since the most intuitive measure of vegetation development is the growth of plant canopies, we opt to use the Leaf Area Index, a dimensionless quantity that characterizes the plant canopies. As we lack in-situ measurements, we use the LAI product provided by CGLS, which is defined as half the total area of green elements of the canopy per unit horizontal ground area. This LAI product offers estimations at a spatial resolution of 300 m, with updates every 10-day based on Sentinel-3 data. Since LAI is a product derived from optical measurements and the greenhouses are sheltered, preventing optical lights from penetrating, LAI data are only available for open crop fields.

6.3. DATA PROCESSING

As clarified in chapter 4, in multilooking, we want all averaged samples to be realizations of the same random distribution. Moreover, for the local scale research, we have access to more detailed land use information. Therefore, we implement a three-step polygon-based multilooking strategy. We start with box-car multilooked 20 m × 20 m resolution products instead of 5 m × 20 m single-look complex (SLC) images to reduce computational costs. This small degree box-car multilooking process has a negligible effect on the final 1 km × 1 km output. Then, we determine which 20 m × 20 m cells fall within the polygons corresponding to a specific crop field type. This step utilizes SIGPAC geographic information, which offers polygons representing different land uses, along with the latitude and longitude coordinates of each 20 m × 20 m cell. Lastly, to generate our 1 km × 1 km product, we calculate the average intensities and interferograms over the selected 20 m × 20 m cells within the 1 km × 1 km window. For each crop field type, Figure 6.2 illustrates the multilooking processing steps. For each class, the number of averaged

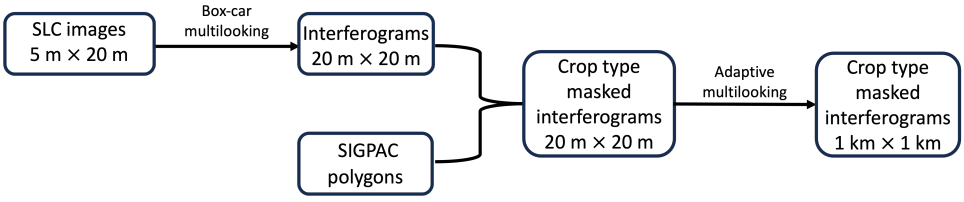

Figure 6.2: Diagram of multilooking data progressing for each crop field type.

1 km × 1 km cells and statistics of ENL are shown in Table 6.3.

For each type of crop field, time series of a specific multilooked quantity behave differently due to differences in the equivalent number of looks (ENL) and other local conditions in each 1 km × 1 km averaged cell. To reduce the risk of having a high noise-level time series, we exclude the 1 km × 1 km cells with ENL smaller than one thousand. Despite differences in ENL and local conditions, we assume that time series of a specific

Table 6.3: Number of averaged 1 km × 1 km cells and ENL information for each field.

Crop field	Cells	Mean ENL	Standard deviation of ENL
Corn fields	1187	$3.8 \cdot 10^3$	$1.3 \cdot 10^3$
Citrus fields	855	$2.3 \cdot 10^3$	$1.1 \cdot 10^3$
Greenhouses	563	$3.2 \cdot 10^3$	$1.4 \cdot 10^3$

multilooked product within fields of a given crop type share a common overall trend. We visualize the mean time series of each multilooked quantity, closure phases Φ_{123}, normalized radar cross-section (NRCS) σ and coherence γ, for three different classes, in Figure 6.5, 6.3, and 6.4, to show their evolution in time. In addition, we visualize the 5th and 95th percentiles of all closure phases time series to reveal the asymmetry in their distribution.

To support the qualitative analysis and interpretation of the observed closure phases, we include the Leaf Area Index as an auxiliary geophysical dataset, which serves as an indicator of crop growth stages throughout the season. To make the LAI dataset comparable to the radar dataset in terms of spatial extent, we apply the same SIGPAC polygons used in SAR multilooking for each open crop field. This allows us to exclude LAI values over crop fields that do not belong to the same class as the target crop type. With the assumption that each cluster of crop fields follow the same schedule for agricultural practices, such as sowing and harvesting, no further spatial operations are applied to match the multilooked SAR grid. Instead, we use only the spatial mean value of the LAI for each crop field in the analysis.

6.4. OBSERVATIONS

6.4.1. OBSERVATIONS OVER CORN FIELDS

Santa Amalia has a large portion of its surrounding fields allocated to corn production. Since SIGPAC does not have a class for corn, we first selected areas labeled as arable land, and then we selected polygons where LAI increases only during the corn crop-growth period from mid-spring to mid-autumn [62]. The mean radar observables time series represented in Figure 6.3 show a clear alignment with the LAI, in particular the peak of the mean closure phase, Φ_{123}, represented by a black solid lines with the corresponding 5th and 95th percentiles indicated by gray shaded regions. Within the time window where the LAI is larger than 0.5 m^2/m^2, the distribution of closure phase time series indicated by their 5th and 95th percentiles shows a large spread from $-10°$ to $55°$ as well as a significant asymmetry around the mean closure phase. The mean NRCS pattern, σ_l, seems to follow that of the LAI with a noisier signature except a 0.6 dB drop around mid-July. However, the mean coherence, γ, which drops significantly from 0.55 to 0.3 around April, increases steadily from late June until it reaches 0.55 again in October. Outside of summertime, the mean closure phase drops to $2.5°$ with variations between $-2°$ and $5°$ except a local maximum around $12°$ in early March, while the mean coherence (between 0.2 and 0.7) and the mean NRCS (between -11.4 dB and -7.0 dB) both have large

variations.

Corn in southern Spain is normally sowed around April. The emergence stage, about two weeks after sowing [63], coincides with a significant increase in the LAI from 0.25 m^2/m^2 to 4.2 m^2/m^2 as well as in the mean NRCS from −11.4 dB to −9.6 dB because of added scattering due to plants growth. As the crop at an early stage grows rapidly, such evolution causes high temporal decorrelation and thus brings the mean coherence down by 0.25. With the development of corn canopies, the LAI, the mean closure phase, and the mean NRCS start decreasing around August until the harvest season finishes and stalks are chopped, around October. However, as canopy conditions stabilize post-LAI peaks, the mean coherence starts increasing from 0.35 to 0.55. The occurrence of post-harvest chopping activities coincides with another 0.3 significant drop in the mean coherence in mid-October. After the corn growth period, fields enter a rest period with catch crops in fields until the next sowing season. In spring, a slight increase in LAI values around March may be associated with the growth of grass in fields, with the subsequent decrease attributed to mowing before planting.

Weather data from Santa Amalia shows frequent precipitation across the year. Such frequent precipitation events provide an explanation for the large fluctuations in the mean coherence and the mean NRCS, while they are less obvious in the mean closure phase.

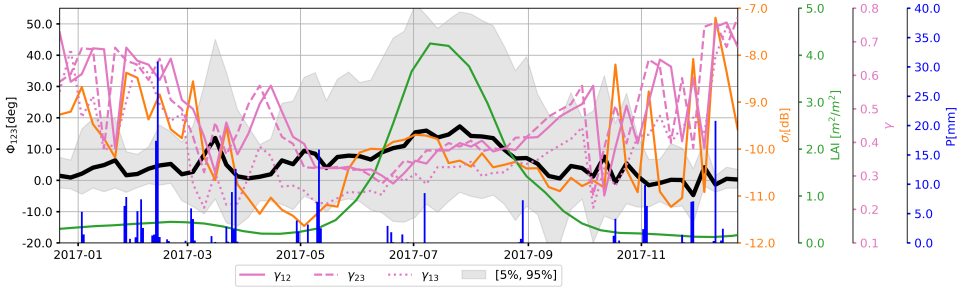

Figure 6.3: Observations over corn fields around Santa Amalia: precipitation records P in Santa Amalia, mean time series of Leaf Area Index (LAI), VV polarized mean time series of closure phases Φ_{123} (black solid line) with corresponding 5th and 95th percentiles, NRCS σ_1 and coherence γ.

6.4.2. OBSERVATIONS OVER CITRUS FIELDS

The Guadalquivir River basin hosts a large number of citrus fields. As shown in Figure 6.4, between spring and early winter, the mean closure phase again presents a consistently positive mean closure phase, Φ_{123}, with 90% of the distribution in the range 0° to 50°. These large positive closure phases are accompanied by reduced mean 6-day coherence values, which decrease from around 0.6 to around 0.3, and a relatively stable mean NRCS (−9.4 dB). Although the harvest season varies with species, most citruses are picked from mid-September till May [64]. This harvest period coincides with a decrease in the mean closure phase from 25° to near 0°. With this information, the increase in the mean closure phase from May can be explained by fruit growth and summer leaf flushes. Summer leaf flushes refer to new leaf growth, and they occur during the period of flow-

ering and fruit development to maintain an adequate photosynthesis level in citrus trees [65].

In contrast to the corn fields, the LAI does not correlate with the radar observables in the citrus fields. There is a drop in the mean satellite-derived LAI values from 1.4 m^2/m^2 to 0.8 m^2/m^2, starting in May and ending before November. Considering citrus trees are evergreen and the plantation frame of citrus fields is about 6 to 7 m × 2.5 m [66], the limited above-ground biomass with wide space between trees makes grass at the ground relevant for the LAI. In the considered location, the hot temperatures ensure that grass usually dries in summer, which contributes to a decrease in LAI. Since LAI is highly affected by grass, the contribution from citrus canopies is hardly discernible in the LAI time series.

The weather record in Brenes (37.55°N, 5.87°W) indicates this area is very windy and has regular precipitation events outside of summertime. Large changes in the SAR-observables time series, especially in the mean coherence and the mean NRCS, are likely caused by these precipitation and gust events.

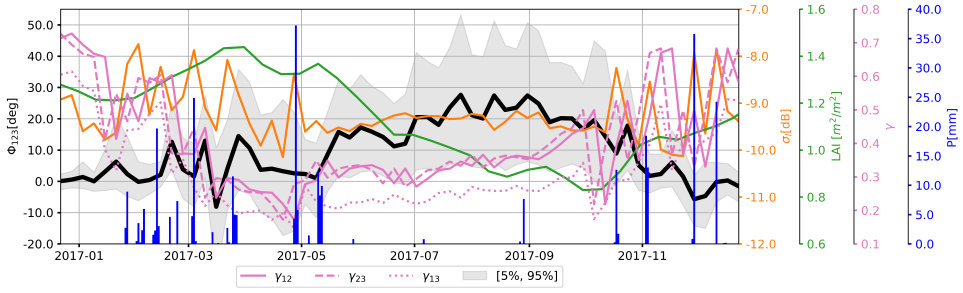

Figure 6.4: Observations over citrus fields in upper Guadalquivir valley: precipitation records P in Brenes, mean time series of Leaf Area Index (LAI), VV polarized mean time series of closure phases Φ_{123} (black solid line) with corresponding 5th and 95th percentiles, NRCS σ_l and coherence γ.

6.4.3. OBSERVATIONS OVER GREENHOUSES

The time series of observables after averaging 1 km × 1 km cells with SIGPAC-designated greenhouses are visualized in Figure 6.5. The mean closure phase, Φ_{123}, is mainly positive across the year, with values ranging from 0° to 10°, and it drops close to zero (1°) during summer from July to September. The mean NRCS, σ_l, shows a similar trend with values as low as −8.8 dB during summer and as high as −7.2 dB out of the season. However, the mean coherence, γ, exhibits an opposite trend where it is significantly higher in summer (0.6) and lower during other seasons (0.4). The spread in the distribution of closure phases, indicated by their 5th and 95th percentiles, correlates with the coherence, the band is narrower when the coherence is higher and vice versa.

Collected field information from El Ejido greenhouses indicates that the majority of greenhouses are dedicated to the growth of everyday vegetables including pepper, cucumber, tomato, and eggplant, and a small portion for fruits like melon and watermelon. According to local farmers[1], they typically plant vegetables at the end of August. This

[1]We obtained this information by visiting thirteen different greenhouses in El Ejido and consulting with

planting season coincides with the emergence of positive mean closure phase, increasing in the mean NRCS from −8.0 dB to −7.2 dB, and decreasing in the mean coherence from 0.5 to 0.3. The mean closure phase peaks in December with 10° when the harvest season starts. After that, there is a gradual decrease in the mean closure phase, while the mean NRCS and the mean coherence remain stable around −7.2 dB and 0.4, respectively. The mean closure phase remains positive until the end of June. From June, the mean coherence exhibits an increasing trend, while the mean NRCS shows a significant decreasing trend. These tendencies coincide with the end of harvest season for most crops. After harvesting, greenhouses typically undergo a period of rest and preparation for days to weeks. During the rest, only bare soil is left inside of greenhouses which explains the high mean coherence (0.6) and the lower mean NRCS (−8.8 dB) during summertime. Overall, a lower mean coherence, a higher mean NRCS, and a positive mean closure phase coincide with the crop growth period within the greenhouses.

Weather records in El Ejido show multiple precipitation events occurred throughout the year, especially outside of the summer season. Precipitation in spring and late autumn coincided with local minima in the mean coherence and the mean closure phase time series, followed by subsequent increases. Two events in October and November correlate with local peaks in the mean NRCS. Apparently, even though the plants are inside greenhouses, the return signal is affected by precipitation. One explanation could be water accumulation on plastic roofs.

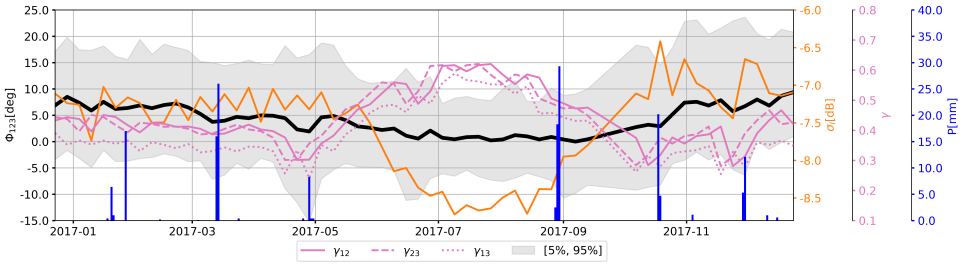

Figure 6.5: Observations over Almería greenhouses: precipitation records P in El Ejido, VV polarized mean time series of closure phases Φ_{123} (black solid line) with corresponding 5th and 95th percentiles, NRCS σ_l and coherence γ.

6.4.4. DISCUSSION

The nature of each radar observable determines its role in conveying information. The NRCS reflects the state of the observed object at the acquisition time. In contrast, the coherence and closure phases, formed with two and three acquisitions, respectively, provide information about the variation in the state of the object over time. In conditions of dense vegetation, variations in radar observables highlight their varying sensitivity to detect changes in biomass.

their owners. These greenhouses are situated across various locations around El Ejido: (36.74°N, 2.82°W), (36.78°N, 2.79°W), (36.77°N, 2.72°W) and (36.76°N, 2.71°W). Despite gathering field information from diverse locations, the information regarding growing season remains consistent. The authors would like to thank the owners of El Ejido greenhouses for providing field information to help us explain observed signals.

Dense vegetation limits the C-band microwave penetration depth in the crop canopy, implying that the radar return corresponds primarily to vegetation and not to the underlying surface. This limited penetration also results in a relatively quick saturation of the NRCS time series, implying that the biophysical information content in the NRCS after this saturation is reached is limited. Although interferometric coherence is an indicator of change and has been studied as a vegetation index [67], it also tends to saturate at low values. Moreover, the magnitude of the coherence cannot be easily linked to a particular cause. All the observations discussed strongly suggest that the closure phase has the potential to serve as an indicator of plant growth or plant productivity. Although the signal is noisy, its mean varies smoothly during the crop-growth cycle, suggesting that a quantitative link may be established between the closure phase and the evolution of crop parameters.

6.5. EXISTING MODELS VERIFICATION

Positive closure phase observations in agricultural areas indicate a relation to plant development. We try to interpret such signatures by modeling the contributions of different mechanisms to the closure phases using existing models, the soil moisture model and the interferometric model for volume scattering.

6.5.1. EXISTING SOIL MOISTURE MODEL

Since soil moisture data within the greenhouses is not available, we only study the soil moisture variation mechanism in open crop fields. Predicting the closure phases related to soil moisture changes consists of three steps. First, we interpolate hourly ERA5 volumetric soil moisture products in soil layers 0-7 cm with the acquisition time of radar observables (Figure 6.6 (a) and Figure 6.7 (a)). Second, we use the dielectric mixing model [50] in combination with Sentinel-1 frequency (5.405 GHz), ERA-5 volumetric soil moisture products, and soil texture in Seville, southern Spain (57.4% sand and 19.6% clay) [68] to model the dielectric constant of the soil. Third, we feed the 2.27 with the modeled dielectric constant and predict the soil moisture-related closure phases. The simulations are compared with the observations in Figure 6.6 (b) and Figure 6.7 (b).

Results over both corn fields and citrus orchards show that most time of the year there is no correlation between closure phases induced by soil moisture variations and observed closure phases (Figure 6.6 and Figure 6.7). This lack of correlation is particularly evident during the corn crop growth period from April to October and the development period of citrus canopies from May to mid-September. The reliability of the comparison may be affected by the heterogeneity in soil moisture variation that the 9 km resolution ERA5 product does not capture. However, the distribution of the modeled time series, as indicated by their 5% and 95% percentiles, suggests that soil moisture in these research areas exhibits limited spatial dynamics. Therefore, each ERA5 data point represents soil moisture across a sizable area. Consequently, it can be deduced that, when vegetation significantly contributes to the scattered radar signal, the soil moisture model cannot explain the observed closure phases. Therefore, during the canopy development period under lush vegetation conditions, we can confidently discard soil moisture variation as being the main source of the observed signatures.

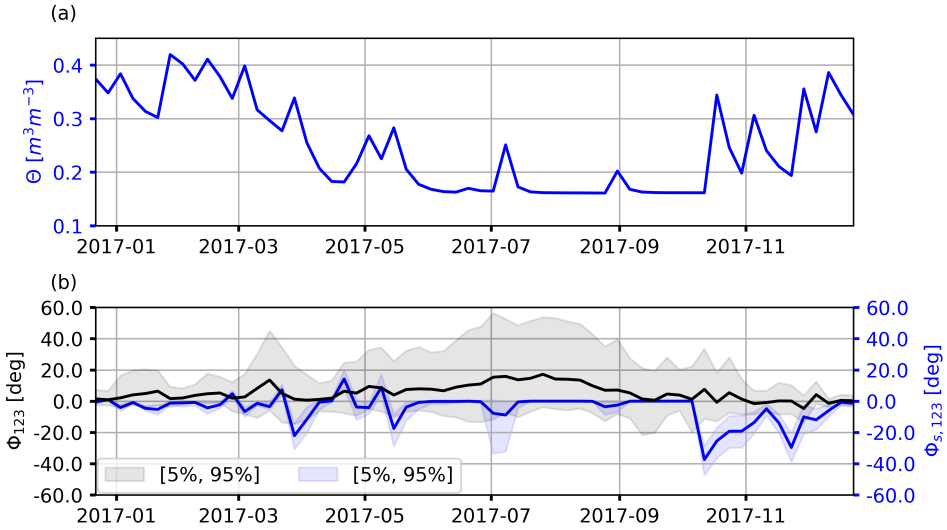

Figure 6.6: Comparison between observed closure phases and closure phases modeled by the soil moisture model over corn fields: (a) mean ERA5 volumetric soil moisture products in soil layer 0-7 cm (blue) Θ, (b) closure phase observations Φ_{123} (black) and simulations $\Phi_{s,123}$ (blue) with corresponding 5th and 95th percentiles.

6

6.5.2. EXISTING INTERFEROMETRIC MODEL FOR VOLUME SCATTERING

Volume scattering in combination with perpendicular baselines is considered as one contributor to closure phases. We simulate its contribution using (2.30). As the scattering profile remains unknown lacking tomographic measurements, we only take the differential vertical wavenumbers κ as inputs to calculate closure phases resulting from this mechanism. The modeled time series in Figure 6.8 exhibit closure phases with fluctuation in signs over all fields. Since Sentinel-1 acquisitions over corn and citrus fields are from the same ascending pass, apart from negligible differences induced by variations in locations, the modeled closure phase time series show comparable behavior. In addition, as the contributions from the triplets of vertical wavenumbers are very small (in the order of $1e-5$), a large height difference within the product resolution would be required to cause closure phases with magnitudes in the same order as the observations. Therefore, the perpendicular baseline-related mechanism can also be excluded in explaining the observed consistent positive closure phases.

6.6. VEGETATION GROWTH MODEL

In previous chapter, we demonstrate that neither of existing models produces positive closure phases that align with plant growth. During vegetation development, the dielectric constant in the vegetation canopy changes because the growth of vegetation elements, meanwhile, the vertical growth introduces a motion in line-of-sight direction. Therefore, considering canopy developments only, we formulate and discuss two novel conceptual models that account for each of these mechanisms by considering an

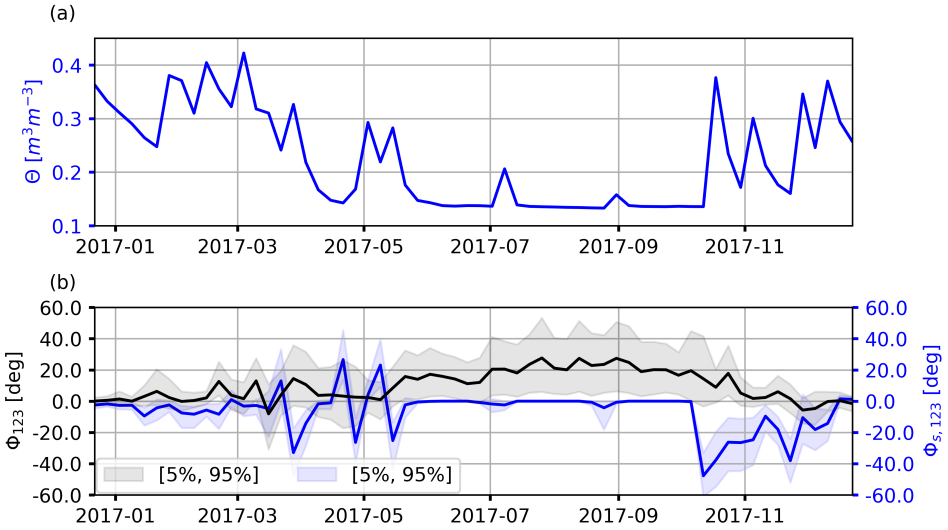

Figure 6.7: Comparison between observed closure phases and closure phases modeled by the soil moisture model over citrus fields: (a) mean ERA5 volumetric soil moisture products in soil layer 0-7 cm (blue) Θ, (b) closure phase observations Φ_{123} (black) and simulations $\Phi_{s,123}$ (blue) with corresponding 5th and 95th percentiles.

equivalent-medium and a skewed distributed vertical velocity profile respectively.

6.6.1. EQUIVALENT-MEDIUM PROPAGATION MODEL

Developments in crop canopies, including leaf and stalk growth, affect closure phase observations by altering the propagation of electromagnetic waves within the canopies. To establish a connection between observed closure phases and the evolution of crop parameters, we developed a propagation closure phase model for canopies with vertical stalks, excluding ground contribution. This propagation model is analogous to the existing soil moisture model [2], retaining the assumptions of isotropic and linear media. However, we substitute the dielectric constant of soil with that of the vegetation canopies and introduce a finite depth for the media based on plant height.

We assume the canopies are a dielectric mixture of stalks and leaves in the air, and describe it as a uniform equivalent lossy medium where stalks and leaves are represented by identical vertically oriented cylinders and randomly oriented thin circular discs [69]. A sketch in Figure 6.9 illustrates the wave propagation on the equivalent medium in a two-dimensional incidence plane xz. The interface between air and the canopies is parallel to the x-axis at $z = 0$. Modeling the dielectric constant of the equivalent medium consists of three steps. First, we compute the dielectric constant of each element in canopies (leaf and stalk) with Ulaby and El-Rayes' linear model which takes frequency f_0, salinity S, and gravimetric moisture m_g as inputs [70]. Second, we consider stalks in the air as a background dielectric medium. According to Ulaby et al., the dielectric

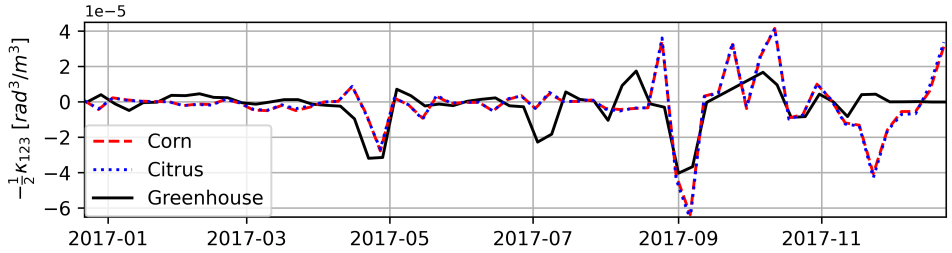

Figure 6.8: Closure phase time series simulations from Sentinel-1 perpendicular baselines of ascending pass 1 (black solid line) and pass 74 (red and blue dotted lines).

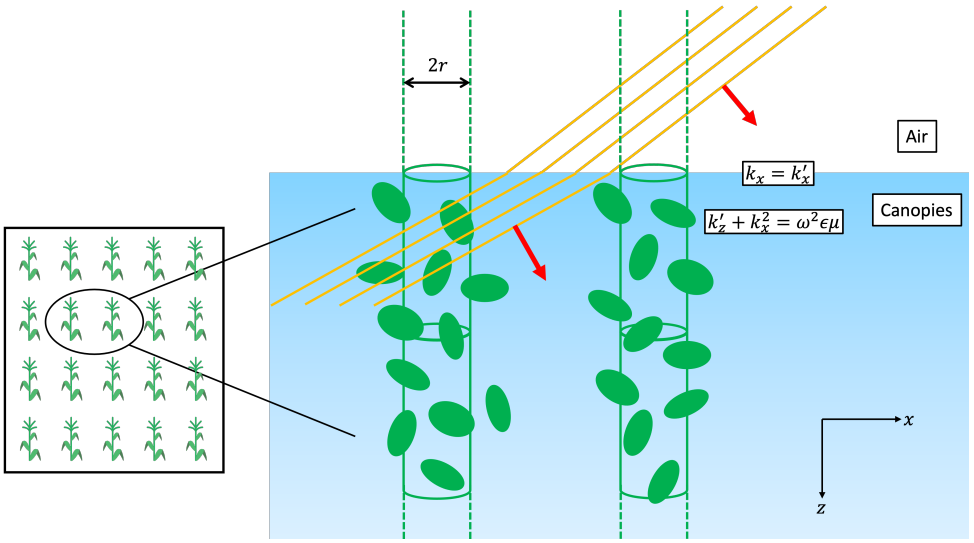

Figure 6.9: Illustration of wave incidence and refraction on an equivalent medium model with a 2D geometry.

constant of this background, ϵ_{rb}, relates to the complex refraction index n_p as,

$$\epsilon_{\mathrm{rb}} = (n_p^{'} + j n_p^{''})^2, \tag{6.1}$$

where n_p is a function of incident angle θ_{i}, radius of stalks r, dielectric constant of stalks ϵ_{rs}, and number of cylinders per unit area N [71]. Last, we add leaves, small in size relative to wavelength, to the background material, the dielectric constant of the full canopies can be written as

$$\epsilon_{\mathrm{r}} = \epsilon_{\mathrm{rb}} + \frac{\upsilon_{\mathrm{l}}}{3}(\epsilon_{\mathrm{rl}} - \epsilon_{\mathrm{rb}})(2 + \frac{\epsilon_{\mathrm{rb}}}{\epsilon_{\mathrm{rl}}}), \tag{6.2}$$

where υ_{l} and ϵ_{rl} are the volume fraction and dielectric constant of leaves, respectively [69].

Taking the modeled dielectric constant of the equivalent medium as input, the expected value of an interferogram of two images with different dielectric constants can

be written as

$$I(\epsilon_{r1},\epsilon_{r2}) = \int_0^{\infty} f(z) e^{-j2k_{z1}^{'}z} (e^{-j2k_{z2}^{'}z})^* \, dz, \tag{6.3}$$

where $f(z)$ is the volumetric scattering coefficient which we assume to be constant, $k_{z1}^{'}$ and $k_{z2}^{'}$ are complex-valued vertical wavenumbers in canopies of each acquisition [2]. According to the wave equation, the vertical wavenumber within the equivalent medium is computed as

$$k_z^{'}(\epsilon_r) = \sqrt{\omega^2 \epsilon \mu - k_x^2}, \tag{6.4}$$

where $\epsilon = \epsilon_r \epsilon_0$ is the permittivity of the medium, and $k_x = \frac{2\pi}{\lambda} \sin\theta_{\mathrm{i}}$ is the horizontal wavenumber, which satisfies the boundary condition that $k_x^{'} = k_x$. As we neglect the contribution from the ground and consider the vegetation canopies only in the model, the propagation of waves is limited by a finite depth of vegetation. In addition, since only the variations in the same group of scatterers contribute to the interferogram, we set the upper limit of the integral in (6.3) as the shorter plant height h between two acquisitions and rewrite the integral as

$$I(\epsilon_{r1},\epsilon_{r2}) = \int_0^{h} f(z) e^{-j2k_{z1}^{'}z} (e^{-j2k_{z2}^{'}z})^* \, dz. \tag{6.5}$$

This integral gives

$$I(k_{z1}^{'}, k_{z2}^{'}, h) = \frac{1 - e^{-2jh(k_{z1}^{'} - k_{z2}^{'*})}}{2jk_{z1}^{'} - 2jk_{z2}^{'*}}. \tag{6.6}$$

At the stage when the plant grows taller, the plant height h in (6.6) is the height at the earlier acquisition. Then the canopies' development-related closure phases can be computed as

$$\Phi_{123} = \angle\Big(I(k_{z1}^{'}, k_{z2}^{'}, h_1) I(k_{z2}^{'}, k_{z3}^{'}, h_2) I(k_{z3}^{'}, k_{z1}^{'}, h_1)\Big). \tag{6.7}$$

The flowchart in Figure 6.10 illustrates the input parameters we need and the steps we followed to derive the final equivalent-medium propagation model in (6.7).

We assume the crop type is the primary factor in affecting the evolution of vegetation parameters regardless of location. To qualitatively evaluate the outputs of our proposed model, we use in-situ measurements made in corn fields near Citra, Florida, USA in 2018 [72]. Vegetation parameters are measured in the cultivated field every 2 - 3 day, starting from the corn crops' planting on 13th April until their harvest on 18th June. Considering the revisit time of Sentinel-1, and discarding the first two weeks of measurements when the soil contribution is dominant as the ground is sparsely vegetated, we resample measurements to a 6-day sampling between 2nd May and 13th June. Following Ulaby et al. [73], with the measured vegetation water content (VWC) and dry biomass m_d, one can compute the gravimetric moisture m_g as

$$m_g = \frac{\mathrm{VWC}}{\mathrm{VWC} + m_d}. \tag{6.8}$$

The calculated values are visualized in Figure 6.11 (a). Using the C-band frequency of

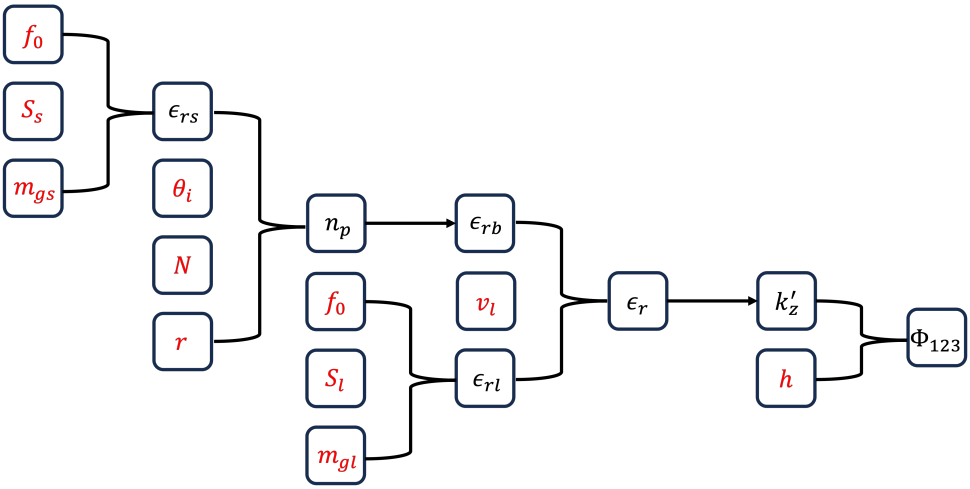

Figure 6.10: Equivalent medium propagation model derivation flowchart with input parameters: frequency f_0, incident angle θ_i, salinity of stalks S_s and leaves S_l, gravimetric moisture of stalks m_{gs} and leaves m_{gl}, number of cylinders per unit area N, volume fraction of leaves v_l, radius of stalks r, and plant height h.

Sentinel-1 $f_0 = 5.405$ GHz, an incident angle $\theta_i = 40°$ and vegetation parameters, such as the stalk radius r, volume fraction of leaves v_l (approximated as 20% of stalk volume) and a constant salinity 10 psu for both stalk and leaf, we estimate the dielectric constant of full canopy ϵ_r with (6.2) (Figure 6.11 (b)). Taking the plant height as the last input (Figure 6.11 (c)), we can then model the corresponding closure phases.

The modeled closure phases in Figure 6.12, where the x-axis represents the first date of three acquisitions, exhibit positive values. Their magnitudes are comparable to observations in corn fields, particularly in May because the planting time in southern Spain is similar to that in the Florida research site. From the modeled results, we can infer the following: first, the rate of change in both the dielectric constant of the full canopy and the plant height correlates to the magnitude of closure phases. This signature suggests the sensitivity of the model outputs to the first and the second derivative of the input parameters. Second, when the variations in the dielectric constant and the plant height are relatively small in June, the modeled closure phases drop to zero. However, observations still show positive closure phases. This disparity suggests we need a more complete and complex equivalent-medium propagation model.

Our propagation model captures the propagation of the incident wave in the canopies under assumptions of an isotropic and linear equivalent medium with a finite depth and a uniform vertical scattering profile. The main value of the model is that, despite the oversimplifications made, it provides a biogeophysical explanation of the observed phase closures. It is clear that simplification of the canopy elements and the lack of other scattering contributions (e.g. surface and double bounce scattering) limit the predictive performance and applicability of the model.

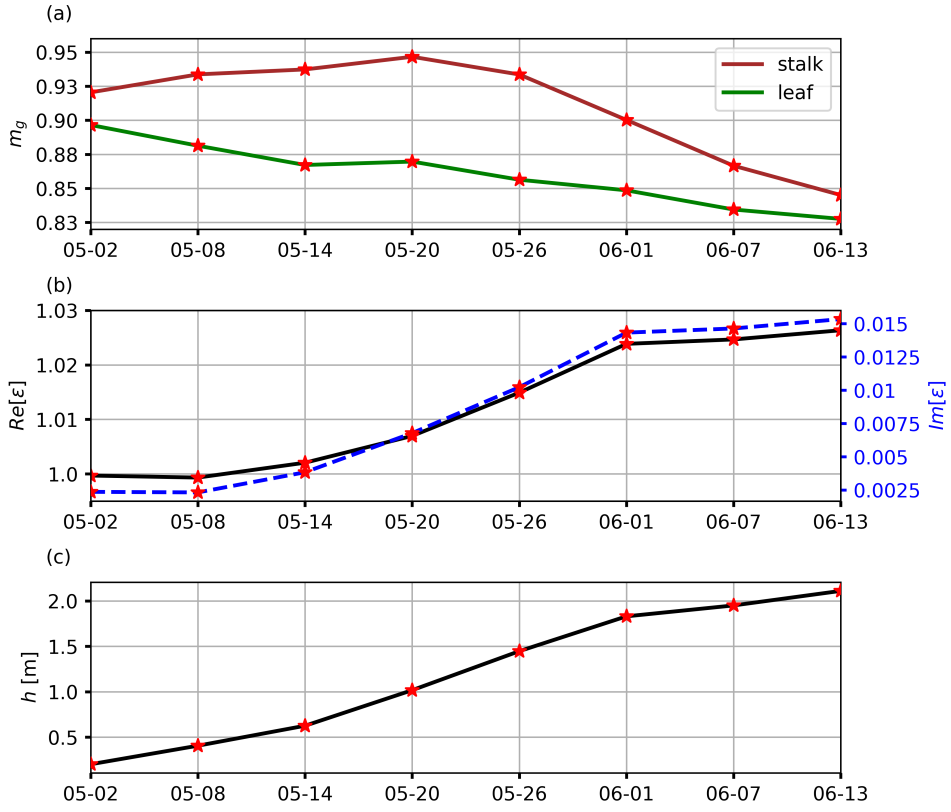

Figure 6.11: Inputs and intermediate results of propagation closure phase model with red stars represent samples: (a) gravimetric moisture of stalk and leaf, (b) the dielectric constant of the equivalent medium which describe the full canopy condition, (c) measured plant height in corn crop fields near Citra, Florida, USA in 2018.

6.6.2. SKEWED MOTION MODEL

Throughout the crop development, in addition to dielectric variations, plants exhibit growth in height from the emergence stage. Growth rates can be very high, as in the case of corn, where it is as high as 5 cm/day after emergence and gradually decreases after approximately two months (Figure 6.11 (c)) [74]. For other crops, such as citrus trees, growth rates are much slower. Crop growth will undoubtedly lead to decorrelation of the *scatterers*. However, we expect that some scattering centers will remain partially coherent as their position changes due to the growth process.

We consider a small magnitude of the LoS projection of velocity (in the order of 0.001 m/day) and develop a motion-induced closure phase model. We start our derivation by writing a conceptual model of the received radar signal at time t as a summation of the

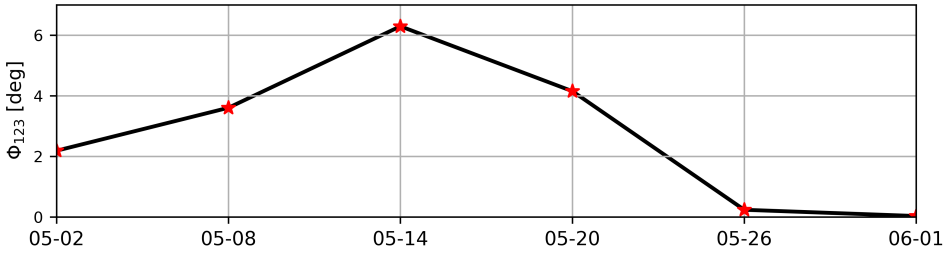

Figure 6.12: Modeled closure phases with vegetation parameters in Figure 6.11 at C-band $f_0 = 5.405$ GHz and incident angle $\theta_i = 40°$.

reflection from a collection of scatterers

$$s(t) = \sum_{m=1}^{N_s} s_m(t), \tag{6.9}$$

where s_m represents complex signals from individual scatterers, N_s is the number of scatterers. For each scatterer, we can write the reflected signal as a combination of phase and amplitude,

$$\begin{aligned} s_m(t) &= A_m(t) e^{j\phi_{0,m}(t)} e^{-2jk_0 r_m(t)} \\ &= s_{0,m}(t) e^{-2jk_0 r_m(t)}, \end{aligned} \tag{6.10}$$

where A_m is the amplitude of scatterers, $\phi_{0,m}$ is the phase of the scattering coefficient, $k_0 = \frac{2\pi}{\lambda}$ is the radar wave number, and r_m is the position of the scatterers in the line-of-sight direction. With another inteferometric compatible acquisition at time $t+\tau$, we can construct the expected value of the interferogram, $I(\tau)$, as

$$\begin{aligned} I(\tau) &= E\left[s(t)s^*(t+\tau)\right] \\ &= E\left[\sum_{m=1}^{N_s}\sum_{n=1}^{N_s} s_m(t)s_n^*(t+\tau)\right] \\ &= \sum_{m=1}^{N_s}\sum_{n=1}^{N_s} E[s_m(t)s_n^*(t+\tau)] \\ &= \sum_{m=1}^{N_s}\sum_{n=1}^{N_s} E[s_{0,m}(t)s_{0,n}^*(t+\tau)e^{2jk_0(r_n(t+\tau)-r_m(t))}], \end{aligned} \tag{6.11}$$

where τ is the time lag. Assuming that the complex backscatter $s_{0,m}(t)$ and the term related to the position of the scatterer, $e^{-2jk_0 r_m(t)}$, are independent from each other, we can write $I(\tau)$ as

$$\begin{aligned} I(\tau) &= \sum_{m=1}^{N_s}\sum_{n=1}^{N_s} R_s(\tau)\delta_{mn} E[e^{2jk_0(r_n(t+\tau)-r_m(t))}] \\ &= N_s R_s(\tau) E[e^{2jk_0(r(t+\tau)-r(t))}] \\ &= N_s R_s(\tau) E[e^{2jk_0\Delta r}], \end{aligned} \tag{6.12}$$

where $R_s(\tau)$ represents the autocorrelation of $s_0(t)$ between t and $t+\tau$, the Kronecker delta, δ_{mn}, reflects the assumption that the scattering coefficients $s_{0,m}$ are zero-mean independent identically distributed random variables, and $\Delta r = r(t+\tau) - r(t)$ is the differential motion of scatterers between two acquisitions.

To simplify the expected value of interferogram (6.12) in an integral form, we make three assumptions. First, we consider the LoS differential motion Δr as a function of velocity v and time lag τ,

$$\Delta r = v\tau. \tag{6.13}$$

Second, we treat N_s as a scaling factor. Third, we assume the temporal decorrelation within the term $R_s(\tau)$ does not influence the closure phases. Focusing solely on the phase information, and normalizing the signal so that it has unit power, we define $I(\tau)$ as

$$\begin{aligned} I(\tau) &= \int f(\Delta r(\tau)) e^{2jk_0\Delta r(\tau)} d\Delta r(\tau) \\ &= \int f(v) e^{j2k_0 v\tau} dv, \end{aligned} \tag{6.14}$$

where $f(\Delta r(\tau))$ is the probability density function (PDF) of the differential LoS motion, $f(v)$ is the PDF of the LoS velocity.

Following the same approach adopted by De Zan et al. [1], we equate (6.14) with the complex interferogram expression, $I(\tau) = A(\tau)e^{j\phi(\tau)}$. Then by taking the first to the fourth order derivatives for both sides, we derive the following relations:

$$\begin{aligned} A(0) &= 1 \\ \phi'(0) &= 2k_0\mu_v \\ A''(0) &= -4k_0^2 E[(v-\mu_v)^2] \\ \phi'''(0) &= -8k_0^3 E[(v-\mu_v)^3] \\ A^{\mathrm{IV}}(0) &= 16k_0^4 E[(v-\mu_v)^4]. \end{aligned} \tag{6.15}$$

To construct an approximation for closure phases, we expand each interferometric phase up to the fourth-order Taylor series with relations in (6.15). Since $\phi''(0) = 0$ and $\phi^{\mathrm{IV}}(0) = 0$, by summing three interferometric phases in a circular way, we get

$$\begin{aligned} \Phi_{123} &= \phi_{12} + \phi_{23} + \phi_{31} \\ &\approx \phi'(0)(\tau_{12} + \tau_{23} + \tau_{31}) + \frac{1}{6}\phi'''(0)(\tau_{12}^3 + \tau_{23}^3 + \tau_{31}^3) \\ &= 2k_0\mu_v(\tau_{12} + \tau_{23} + \tau_{31}) \\ &\quad - \frac{4}{3}k_0^3 E[(v-\mu_v)^3](\tau_{12}^3 + \tau_{23}^3 + \tau_{31}^3), \end{aligned} \tag{6.16}$$

where $E[(v-\mu_v)^3]$ is the third order central moment of the velocity profile. In the case of closure-phase construction with continuous Sentinel-1 acquisitions, $\tau_{12} + \tau_{23} + \tau_{31} = 0$ and $-\tau_{12} = -\tau_{23} = \frac{1}{2}\tau_{31} = \tau$. Therefore, (6.16) becomes

$$\Phi_{123} = -8k_0^3 E[(v-\mu_v)^3]\tau^3, \tag{6.17}$$

where $E[(v-\mu_v)^3]$ is the third order central moment of the velocity profile. This derivation of the model is largely analogous to the volumetric scattering model reflected in (2.30). This model implies that under a small motion approximation, a skewed velocity distribution will lead to non-zero closure phases.

We employed a simple approach by assuming a skewed-normal distribution for LoS velocity to generate closure phases with numerical simulations. According to the maximum likelihood estimation, the skewness γ_1 of a skewed-norm distribution can be written as a function of shape parameter α_1,

$$\gamma_1 = \frac{4-\pi}{2}\frac{(\delta\sqrt{2/\pi})^3}{(1-2\delta^2/\pi)^2}, \tag{6.18}$$

where $\delta = \frac{\alpha_1}{\sqrt{1+\alpha_1^2}}$. When $\alpha_1 = 0$, the skewness $\gamma_1 = 0$ and thus the distribution becomes a normal distribution. Assuming the shape parameter α_1 follows a uniform distribution within the range of -28 to 28, corresponding to a theoretically derived skewness (6.18) in the range of -0.99 to 0.99, and considering 6-day revisit time of Sentinel-1, we simulated closure phases using (6.17) for different skewness inputs. The closure phases results, range from $-30°$ to $30°$, are visualized against the estimated skewness from the shape parameter in Figure 6.13. These results confirm that as long as the velocity distribution

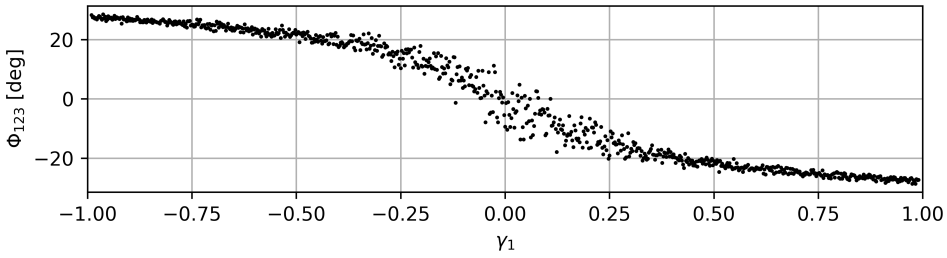

Figure 6.13: Numerically simulated closure phases with the skewed motion model when the estimated skewness γ_1 ranges from -1 to 1.

is skewed, the motion in LoS will result in a non-zero closure phase. Additionally, a larger degree of skewness produces larger closure phases.

In the absence of ground truth measurements, we are currently unable to directly link the model to closure phase observations. Nevertheless, under the assumption that some scatterers will remain coherent while being subjected to crop-growth-related motion, we can expect that a skewed motion distribution will introduce closure phases. On the one hand, as crops within a 1 km resolution cell exhibit diverse and non-uniform developmental characteristics, non-zero closure phases will manifest when there is a skewed distribution in their LoS motion. This phenomenon holds across different crop types. On the other hand, the level of skewness can be expected to vary with the stage of vegetation development, potentially resulting in closure phases that align with the crop growth cycle.

6.7. A COMPOSITE MODEL

In typical scenarios, the radar signal received from an imaging cell contains contributions from vegetation, ground surface scattering, and soil. We propose a composite model that accounts for dielectric variations in a three-layered medium by combining soil and vegetation propagation models with a surface scattering model. Using the same geometry as applied in the soil moisture and canopy equivalent medium models, Figure 6.14 illustrates the wave propagation through a three-component equivalent medium within a two-dimensional incidence plane (xz-plane).

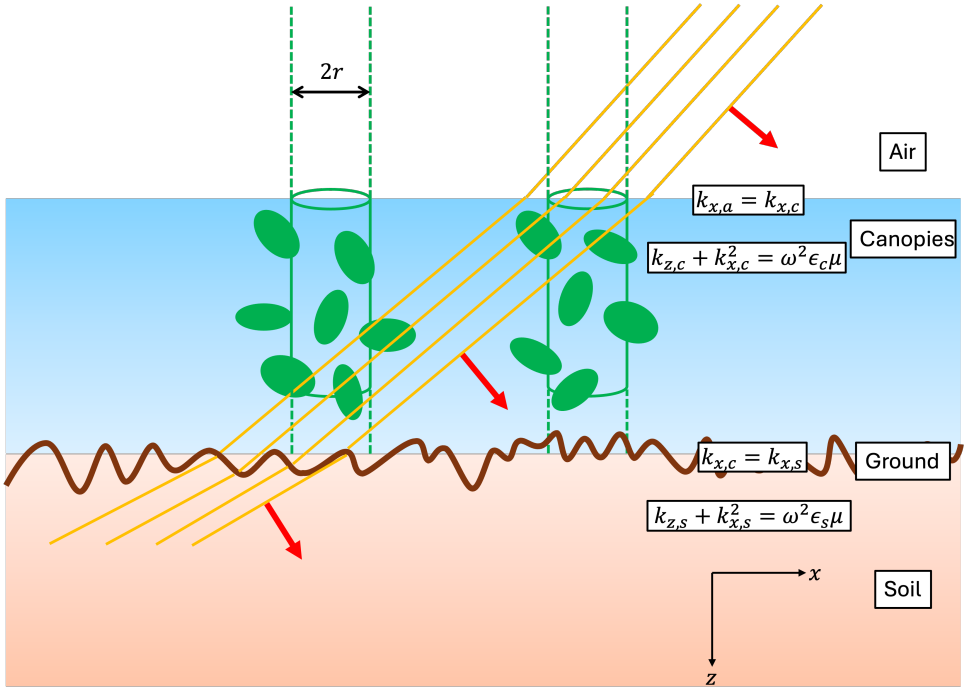

Figure 6.14: Illustration of wave incidence and refraction on a composited equivalent medium propagation model, with the z-axis origin at the canopy top and positive direction downward.

For each medium, we consider both propagation and scattering contributions. In line with previous propagation models, the backscattered signal at a focused pixel located at range r_0 and azimuth y_0 is expressed as an integral, accounting for contributions from all elementary scatterers within it. To model the surface scattering, we adopt the Advanced Integral Equation Model (AIEM) [75]. As a physical model, AIEM describes electromagnetic scattering from rough surfaces by incorporating observation geometry, surface roughness statistics (such as surface correlation function), and dielectric properties of the medium.

To model the total signal response from interactions with all components, we consider both attenuation and phase alterations of the traveling wave through a lossy medium, the vegetation canopy. We treat the canopy as a homogeneous medium with a constant

effective dielectric constant. Under this assumption, the electric field amplitude within the canopy decreases exponentially with depth due to absorption and scattering. This propagation is modeled using a factor $e^{-jk_z z}$, where the complex vertical wavenumber k_z accounts for the effects of both phase delay and signal attenuation.

Retaining the same geometric approximation as in the previous propagation models, the signal corresponding to a point at range r_0 and azimuth y_0 can be expressed as

$$\begin{aligned} p(r_0, y_0, t) = &\int_0^h \xi_v(z,t) e^{-2jk_{z,v}z} dz + e^{-2jk_{z,v}h} \int_0^\infty \xi_s(z,t) e^{-2jk_{z,s}z} dz \\ &+ e^{-2jk_{z,v}h} \xi_g(t) p_g(r_0, y_0, t), \end{aligned} \tag{6.19}$$

where $\xi(z,t)$ is a complex-valued volumetric scattering profile, which we treat as a random process, and $p_g(r_0, y_0, t)$ represents the contribution of surface scattering. Assuming that the scattering behaves as a stationary random process, a height-dependent coherence term, $\rho(t - t_0, z)$, can be incorporated into the second order characteristics of the scattering distribution:

$$\boldsymbol{E}[\xi(z,t)\xi^*(z_0,t_0)] = f(z)\delta(z - z_0)\rho(t - t_0, z), \tag{6.20}$$

6

where $f(z)$ is the vertical scattering density profile. We assume that $\rho(t - t_0, z)$ is monotonically decreasing with increasing temporal lag, $t - t_0$, and satisfies $\rho(0, z) = 1$. Assuming that the scattering components are mutually uncorrelated and that the ground surface has the same dielectric properties as the underlying soil, the expected value of interferogram product between two acquisitions with different vegetation and soil dielectric constants is given by:

$$\begin{aligned} I_{12} = &\int_0^h f_v(z)\rho_v(t - t_0, z) e^{-2j(k_{z1,v} - k^*_{z2,v})z} dz \\ &+ e^{-2j(k_{z1,v}h_1 - k^*_{z2,v}h_2)} \Big(\int_0^\infty f_s(z)\rho_s(t - t_0, z) e^{-2j(k_{z1,s} - k^*_{z2,s})z} dz \\ &+ \rho_g(t - t_0) I_{z,g} \Big), \end{aligned} \tag{6.21}$$

where ρ_g is the surface scattering coherence function and $I_{z,g}$ represents the expected value of the interferometric phase contribution estimated using the AIEM.

In the bare soil and vegetation-only models, the phase and, consequently the closure phase, depends on the vertical scattering profile but not on the total NRCS. In contrast, in the composite model, the phase will depend on the relative strength of the different scattering contributions. Estimating a representative backscattering coefficient for each component is a challenging task. To avoid developing a comprehensive backscatter model, we adopt a water cloud model [76]. We assume that this model provides a reasonable estimate of the backscatter contributions from the soil and vegetation canopy , thereby simplifying both the model formulation and the subsequent simulations.

6.7.1. BACKSCATTER REPRESENTATION USING A WATER CLOUD MODEL

According to the water cloud model [76], the NRCS, representing the combined contribution of volume scattering from vegetation and soil, is expressed as:

$$\begin{aligned}\sigma_l &= \sigma_{l,v} + \sigma_{l,s} \\ &= [C(1-e^{-4\alpha r}) + A^{'} m_s e^{-4\alpha r}]\cos\theta_r.\end{aligned} \tag{6.22}$$

the attenuation constant α is computed as $\alpha = \mathrm{Re}[jk]$. The propagation distance $r = h/\cos\theta_r$, where the refraction angle θ_r is calculated using the proportion of the real part of wavenumbers

$$\theta_r = \arccos\frac{\mathrm{Re}[k_z]}{\mathrm{Re}[k]}. \tag{6.23}$$

The parameter m_s is the volumetric soil moisture content. The coefficients C and $A^{'}$ are constants that depend on the radar frequency, polarization, observation geometry and relevant geophysical properties.

Estimating the model coefficients requires in-situ measurements, therefore, we conduct a case study over the corn field described in section 6.4.1. Feeding model (6.22) with geophysical measurements and radar observations yields $C \approx 0.14$ and $A^{'} \approx 0.35$. The backscatter contribution from vegetation and from the soil can then be computed as

$$\hat{\sigma}_{l,v} = 0.14(1-e^{-4\alpha r})\cos\theta_r \tag{6.24}$$

and

$$\hat{\sigma}_{l,s} = 0.35 m_s e^{-4\alpha r}\cos\theta_r, \tag{6.25}$$

respectively.

To integrate the backscatter terms into (6.21) and represent the intensity of each component, three adjustments are made:

1. reprojection of the backscatter terms onto the vertical (z) direction, where the phase is defined,
2. removal of attenuation factors already included in both backscatter terms,
3. and removal of the ground contribution already included in the estimation of the C and $A^{'}$ coefficients.

Assuming a uniform vertical scattering profile, the scattering profile dependent propagation distance $\eta(r)$ reduces to a constant η_0. With these adjustments, the projected intensity can be expressed as

$$\sigma = \cos\theta_r \int \eta(r) e^{-4\alpha(r)r}\, dr = \eta_0 \int e^{-4\alpha_z z}\, dz. \tag{6.26}$$

Using the predicted backscatter coefficients and applying the integration range for each medium, η_0 of each layer can be computed. For the vegetation component, combining (6.24) with (6.26), and including the limits of the integral, yields

$$\hat{\sigma}_{l,v} = \eta_{0,v} \int_0^h e^{-4\alpha_{z,v} z}\, dz. \tag{6.27}$$

From this expression, the constant, $\eta_{0,v}$, can be derived as

$$\eta_{0,v} = \frac{4\hat{\sigma}_{l,v}\alpha_{z,v}}{1 - e^{-4\alpha_{z,v}h}} \tag{6.28}$$

for the vegetation. For the soil component, the attenuation caused by the vegetation layer must be taken into account. Therefore,

$$\hat{\sigma}_{l,s} = \eta_{0,s} e^{-4\alpha_{z,v}h} \int_0^{\infty} e^{-4\alpha_{z,s}z} dz. \tag{6.29}$$

Accordingly, the constant, $\eta_{0,s}$, is given as

$$\eta_{0,s} = \frac{4\hat{\sigma}_{l,s}\alpha_{z,s}}{e^{-4\alpha_{z,v}h}}, \tag{6.30}$$

for the soil. Since this term partially represents the contribution from ground scattering, the ground component, give by $|I_{z,g}|$, needs to be subtracted to avoid the redundancy. Finally, the expected value of the interferogram can be reformulated as:

$$\begin{aligned} I_{12} = C_{v,12} \int_0^h \rho_v(t - t_0, z) e^{-2j(k_{z1,v} - k^*_{z2,v})z} dz \\ + C_{a,12}\Big(C_{s,12} \int_0^{\infty} \rho_s(t - t_0, z) e^{-2j(k_{z1,s} - k^*_{z2,s})z} dz \\ + \rho_g(t - t_0) I_{z,g}\Big), \end{aligned} \tag{6.31}$$

where $C_{v,12} = \eta_{0,v12}$, $C_{s,12} = \eta_{0,s12} - |I_{z,g}|$ and $C_{a,12} = e^{-2j(k_{z1,v}h_1 - k^*_{z2,v}h_2)}$.

6.7.2. GENERALIZED SIMULATION UNDER SIMPLIFICATIONS

To examine a general case and assess the influence of each component on the resulting closure phases, we simulate the composite model under a set of simplifying assumptions. Most bio-geophysical parameters are fixed, while soil and leave moisture as treated as the main drivers of phase variations and are assumed to vary simultaneously. In addition, decorrelation is neglect, and the contribution from ground scattering is assumed to be negligible.

Using the previously adopted ground truth information, we fix the stalk gravimetric moisture at 0.8, the stalk radius at 0.0081 m, and the plant height at 1.5 m. The leaf and soil moisture content are varied over the range 0.02 to 0.98 $m^3 m^{-3}$. These values are chosen to ensure that the penetration depth exceeds the plant height, allowing contributions from both the vegetation and the soil.

Before simulating the combined effects of soil and leave moisture variations, we first examine the influence of each moisture component individually. Figure 6.15 shows that, for selected moisture values of 0.3, 0.6, and 0.9 $m^3 m^{-3}$ in one component, increasing the moisture of the other component decreases the magnitude of the composite closure phase. However, for the same increase in moisture, the composite-model closure phase is less sensitive to changes in leave moisture than to changes in soil moisture. Additionally, we examine the effect of the multilayer configuration by simultaneously varying the

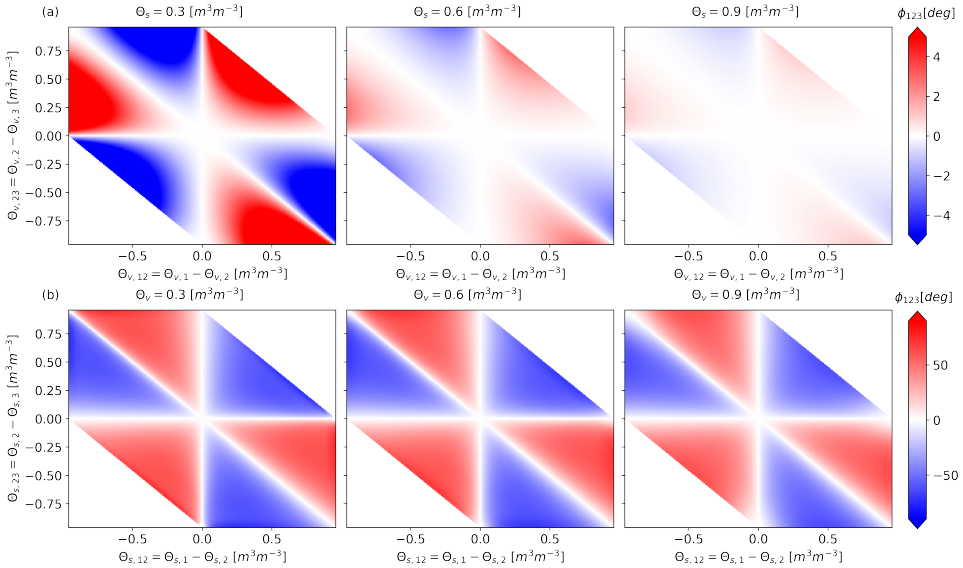

Figure 6.15: Effects of (a) soil and (b) leave moisture variations on composite model closure phases. From left to right, the fixed moisture values are 0.3, 0.6, and 0.9 m^3m^{-3}, respectively.

soil and leave moisture content over the range 0.02 to 0.98 m^3m^{-3}. We isolate this effect by assuming phases consistency for the soil and vegetation layers, as well as for the vegetation related attenuation. That is achieved by enforcing

$$\angle(I(\epsilon_1^{'},\epsilon_3^{'})) = \angle(I(\epsilon_1^{'},\epsilon_2^{'})I(\epsilon_2^{'},\epsilon_3^{'})) \tag{6.32}$$

for each component. Figure 6.16 illustrates phase consistency enforced for each layer and the resulting closure phases arising from the multilayer configuration. It is clear that even with phase consistent layers, the composite model can produce non-zero closure phases due to the multilayer structure.

Including contributions from all individual components, Figure 6.17 presents the closure phases generated by the individual soil and vegetation components, as well as by their combined contribution. As shown in the simulated results, combining the two closure phase components in the composite model does not necessarily lead to larger closure phases, even when the individual components have the same sign. In some cases, sufficiently large moisture differences can cause the resulting closure phase to reverse sign. This behavior arises because the composite closure phase is governed not only by the individual components but also by the complex interactions among the multiple scattering layers.

6.7.3. NO DECORRELATION CASE

To assess the behavior of the composite model relative to previous propagation models, we retain the same assumptions and begin with the simplest scenario, in which temporal decorrelation is neglected. Under these assumptions, the expected value of the

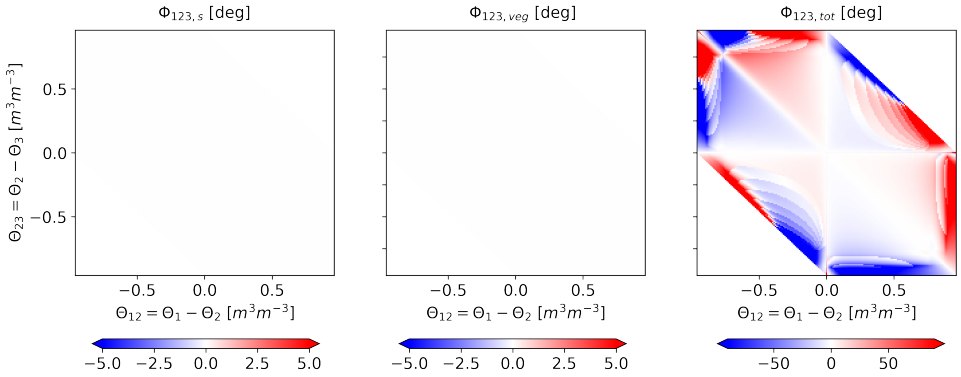

Figure 6.16: From left to right: closure phases generated by soil moisture variation, leave moisture variation, and the final closure phases predicted by the composite model when the phases are consistent for each layer.

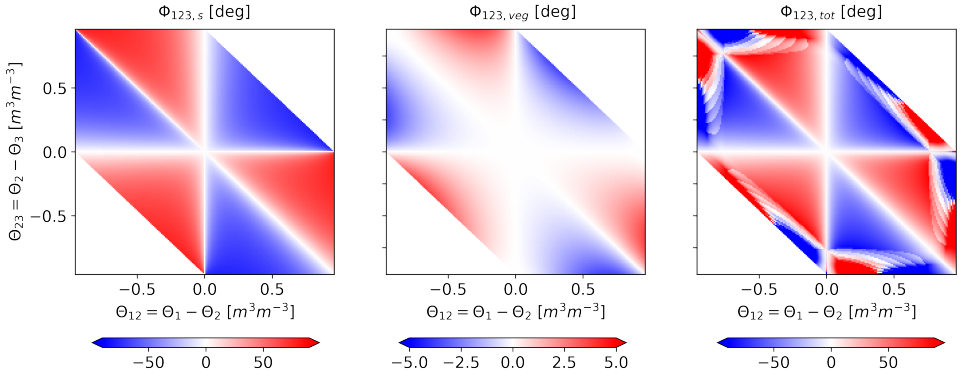

Figure 6.17: From left to right: closure phases generated by soil moisture variation, leave moisture variation, and the final closure phases predicted by the composite model.

interferogram in (6.31) can be expressed in a simplified form:

$$\begin{aligned} I_{12} &= C_{v,12}\int_0^h e^{-2j(k_{z1,v}-k^*_{z2,v})z}dz + C_{a,12}\Big(C_{s,12}\int_0^\infty e^{-2j(k_{z1,s}-k^*_{z2,s})z}dz + I_{z,g}\Big) \\ &= C_{v,12}\frac{1-e^{-2jh(k_{z1,v}-k^*_{z2,v})}}{2j(k_{z1,v}-k^*_{z2,v})} + C_{a,12}\Big(C_{s,12}\frac{1}{2j(k_{z1,s}-k^*_{z2,s})} + I_{z,g}\Big). \end{aligned} \tag{6.33}$$

We consider the same research area, the corn field around Santa Amalia, used to validate the vegetation equivalent-medium propagation model in section 6.6.1. Therefore, the composite model is parameterized using ISRIC soil texture information (48.8% sand and 18.1% clay), ERA5 soil moisture measurements for the 0-7 cm layer (Figure 6.18) [51], and the vegetation parameters adopted in section 6.6.1.

The predicted closure phases for each individual component, as well as those of the composite model, are illustrated in Figure 6.19. According to the computed results,

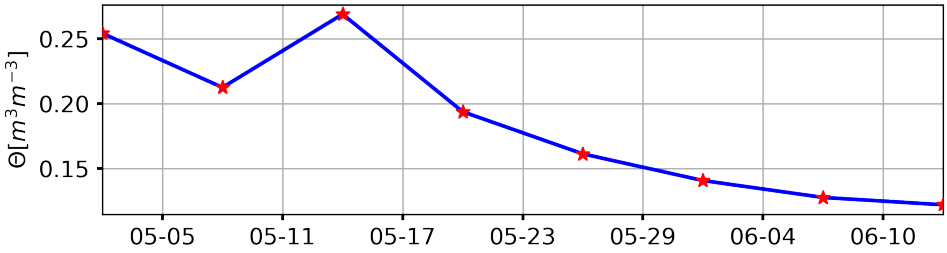

Figure 6.18: ERA5 soil moisture measurements for corn fields around Santa Amalia.

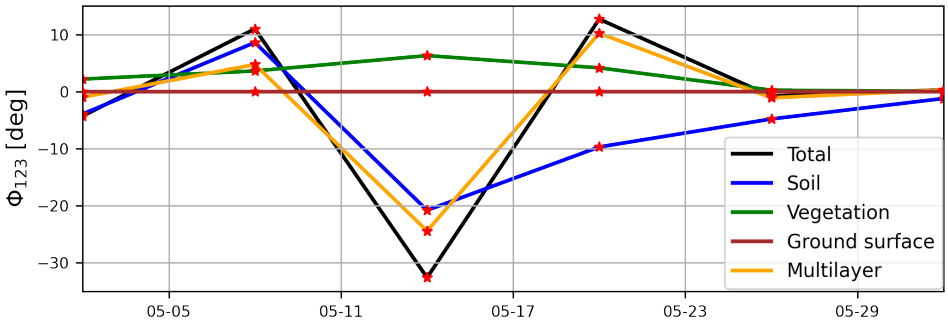

Figure 6.19: The predicted closure phases obtained for each individual component and the composite model prediction under the assumption of no decorrelation effects.

ground surface scattering contributes negligibly to the observations, the vegetation component produces positive closure phases with a magnitude of about 5°, and subsurface propagation within the soil and the multilayer structure produce closure phases ranging from −20° to 10°. When the contributions from each layer are scaled by their respective amplitudes and the propagation factor associated with wave propagation through vegetation is included, the resulting three-component model predicts closure phases ranging from −30° to 15°. Compared with the results produced by considering only propagation within vegetation, adding the effects of backscatter and the contributions from soil and ground surface scattering does not always lead to larger closure phases. This behavior arises from three main factors: soil moisture variation induced closure phases are not consistently positive, and the effects of vegetation layer attenuation and the relative scaling of backscattering contributions are not negligible. Additionally, the final results exhibit the same trend as the multilayer closure phases generated by enforcing phase consistency in each layer, although the latter exhibits magnitudes closer to 0°. This similarity highlights the important role of the multilayer structure in the closure phases predicted by the composite model. Moreover, similar to the vegetation-only propagation model, the predicted closure phases in late May remain close to zero because models are mainly sensitive to changes in bio-geophysical parameters, such as vegetation water content and soil moisture, which vary little during this period.

6.7.4. EFFECT OF DECORRELATION

Since representative two-dimensional coherence density profiles are unavailable, we employ a simplified model for the coherence density distribution to assess the impact of decorrelation on the interferometric model. We begin with the temporal decorrelation model proposed in [77]

$$\gamma(t-t_0) = (\gamma_0 - \gamma_\infty)e^{-\frac{t-t_0}{\tau}} + \gamma_\infty, \tag{6.34}$$

τ is the time constant, γ_0 and γ_∞ represent the minimum and maximum coherence, respectively. For mathematical convenience, we introduced an exponential depth dependency into the decorrelation model and obtain the coherence density function as:

$$\rho(t-t_0, z) = (\gamma_0 - \gamma_\infty)e^{-\frac{t-t_0}{\tau}} \frac{1-e^{-z}}{1-e^{-h_{\max}}} + \gamma_\infty, \tag{6.35}$$

where $h_{\max}$ is the maximum penetration depth.

The model is parameterized using C-band observations over vegetated and bare soil surfaces [78–80] for the corresponding media. The maximum plant height in the observations is approximately 2.11 m, and the maximum soil penetration depth is estimated to be 6 cm based on the soil moisture observations. The resulting temporal decorrelation for vegetation and soil are expressed as

$$\rho(t-t_0, z) = \Gamma_t(t-t_0)(1-e^{-z}) + 0.2, \tag{6.36}$$

where

$$\Gamma_{t,v}(t-t_0) = \frac{0.5e^{-\frac{t-t_0}{36}}}{1-e^{-2.11}} \tag{6.37}$$

for vegetation, and

$$\Gamma_{t,s}(t-t_0) = \frac{0.6e^{-\frac{t-t_0}{36}}}{1-e^{-0.06}} \tag{6.38}$$

for soil. For surface scattering, there is no depth dependence, therefore, the coherence density function is expressed as

$$\rho_g(t-t_0) = 0.6e^{-\frac{t-t_0}{36}} + 0.2. \tag{6.39}$$

For illustration purpose, the coherence density functions are computed by varying the penetration depth from 0 to 2 m for vegetation and from 0 to 5 cm for soil, while varying the temporal lag from 0 to 100 days. The resulting coherence density functions and their contour lines are shown in Figure 6.20. The two main function features are that coherence decreases with increasing temporal lag and increases with penetration depth. In addition, soil coherence generally remains higher than vegetation coherence because vegetation experiences stronger decorrelation due to its dynamic nature and sensitivity to environmental disturbances such as wind.

To investigate the effect of decorrelation on each component, Figure 6.21 compares the vegetation, soil, multilayer, and composite model predictions before and after including decorrelation. According to the predictions, introducing decorrelation into the

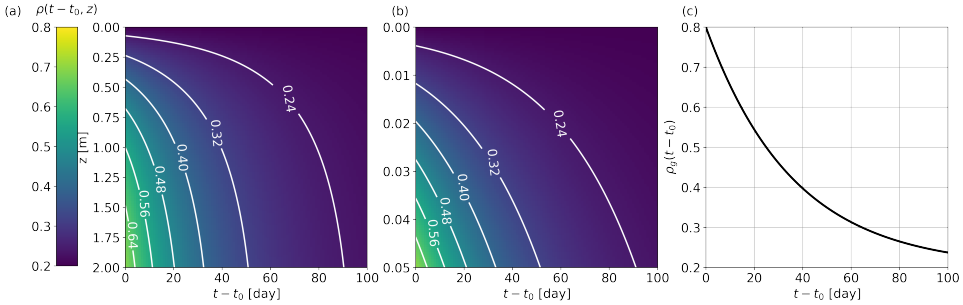

Figure 6.20: Illustration of coherence density functions corresponding to (a) the vegetation with contour lines, (b) the soil with contour lines, and (c) the ground surface.

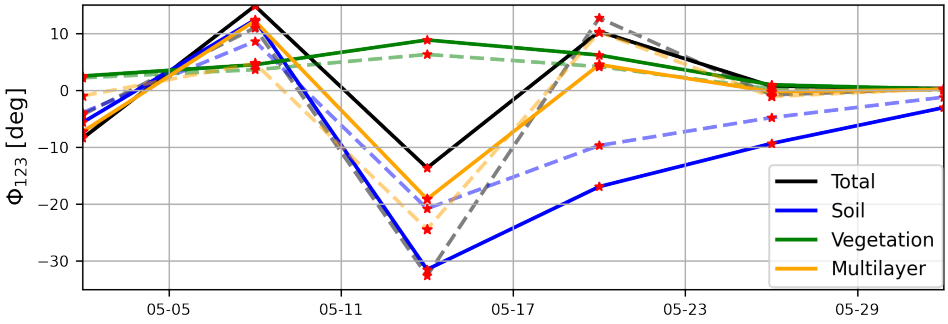

Figure 6.21: Comparison of predicted closure phases before (dashed lines) and after (solid lines) including decorrelation for vegetation, soil and (c) composite models.

vegetation and soil components results in closure phases with larger magnitudes. This behavior arises because the decorrelation term modifies the effective phase center within the medium. Such a signature highlights a limitation of the original propagation models, which do not explicitly account for the spatio-temporal decorrelation effects within the media. The inclusion of decorrelation also improves the agreement between the closure phases predicted by the multilayer component and those predicted by the composite model. However, it does not consistently increase or decrease the predicted closure phase magnitudes. This non-linear variation is linked to the dominant contributing component in the composite model, which depends on the relative changes in plant height and the penetration depth in vegetation, $\delta_{s,v} = \frac{1}{\sqrt{\alpha_{z,v}}}$, as shown in Figure 6.22. When the vegetation penetration depth exceeds the plant height, as in the first four timestamps, the received signal is dominated by the soil contribution. Therefore, the decorrelation effect on the first two phase triplets mainly reflects the behavior of the soil component, resulting in slightly larger closure phase magnitudes. As vegetation develops and the penetration depth decreases, the relative contribution of the vegetation component increases, causing the predicted closure phases to approach those of the vegetation component.

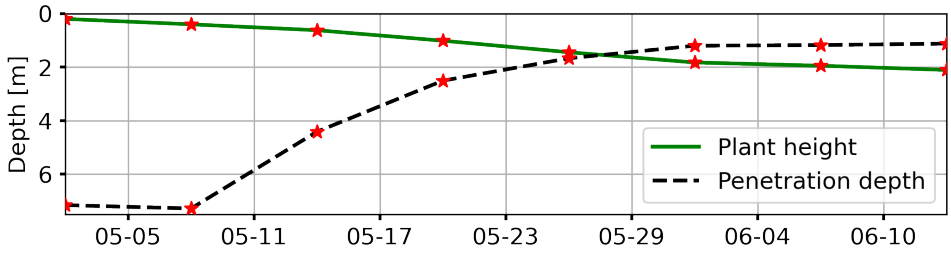

Figure 6.22: Variation of the plant height and the penetration depth in vegetation.

6.7.5. DISCUSSION

Compared with previous single-layer propagation models, the composite model is physically more comprehensive, as it integrates multiple layers and accounts for both propagation and scattering effects. It provides valuable insight into the origin of non-zero closure phases, showing that multilayer interactions can generate additional phase responses even when individual layer phases are consistent. When vegetation and soil both contribute to the signal, their effects are not simply additive but are modulated by relative backscatter and attenuation from overlying layers.

Despite being more physically comprehensive, the model does not clearly improve the agreement with observations and fails to resolve the major discrepancies, particularly in late May (Figure 6.3). This indicates that dielectric variations alone are insufficient to reproduce the observed closure phase behavior. Incorporating additional mechanisms, such as LoS motion, may provide a more complete physical representation, although the increasing number of unknown parameters makes their benefits difficult to assess. The complexity of the model and the remaining discrepancies also highlight the inherent limitations of purely physical models in capturing the complexity of real-world processes.

7

CONCLUSIONS AND RECOMMENDATIONS

The search for closure in InSAR closure phases has motivated this research. Three sequential research questions were formulated, each building upon the findings of the previous stage, to progressively advance our understanding of closure phases. In Chapter 4, we investigated the spatiotemporal signatures of Sentinel-1 observed closure phases and provided statistical analyses highlighting the presence of a geophysical component beyond phase noise. This finding established the foundation for an exploration of the relationship between observed closure phases and geophysical processes. Subsequently, in Chapter 5, we examined the capability of existing models to explain the observed signals, while quantitatively assessing the unexplained portion of the observations. The analysis revealed that a substantial fraction, approximately 50%, of the closure phase variance in vegetated regions remains unaccounted for. Guided by this finding, Chapter 6 focused on detailed analyses of crop fields at the local scale, supported by in-situ and auxiliary geophysical measurements. Through this investigation, we partially resolved the unexplained component by attributing it to vegetation growth dynamics and proposed models to support this interpretation.

7.1. CONCLUSIONS

Question 1: *How prevalent are statistically significant non-zero closure phases?*

We addressed this question by analyzing closure phases generated from one year of Sentinel-1 acquisitions, widely distributed across the Iberian Peninsula and including both morning and afternoon viewing geometries. Returning to our starting hypothesis, one of the important conclusions we draw is that statistically significant closure phases with a geophysical origin are indeed very common, with between 30% and 50% of all cells considered exhibiting a significant closure phase with a 95% confidence, depending on the time of the day and season of the acquisition. As expected, the temporal statistics of these closure phases are highly dependent on geophysical conditions, in-

cluding land cover type and climate zone. In general, the closure phase signal contains high-frequency components driven by short-term weather variations and low-frequency components associated with seasonal dynamics.

The widespread presence of geophysical closure phases has implications for exploiting InSAR time series for deformation analyses over distributed areas. Our focus, however, lies in the non-geometric information in the InSAR phase and manifested through the closure phases. The observation that even small closure phases are often quite significant, i.e., they exhibit a high *signal to noise ratio*, suggests that these signals can be exploited for the retrieval of bio-geophysical parameters.

Question 2: *To what extent do current models explain the observed closure phases?*

We investigated this question by quantifying the extent to which observed closure phases could be explained by known mechanisms, in particular by soil moisture variations and volume scattering in combination with perpendicular baselines, using the coefficient of determination. As expected, given the narrow orbital tube of Sentinel-1 during the period of the analyzed data, the contribution of perpendicular baseline variation to observed closure phases is minimal, as indicated by the weighted Pearson correlation. However, exceptions were found in regions with high missing topography in the digital elevation model used to flatten the interferometric phase. For the soil moisture variation mechanism, we observed a positive but low correlation (mean around 0.20) between the modeled closure phases and observations across the Iberian Peninsula, including forested areas where C-band signals typically do not penetrate down to the surface below the canopy. This correlation likely arises from the simultaneous response of canopy water content and subsurface moisture to precipitation and temperature changes, as well as from the coupling between canopy water content and subsurface water content variations [58, 59]. Sub-regions classified by climate zones display varying statistical patterns, highlighting that local geophysical conditions play an important role in modulating the contributions of soil moisture variation to closure phases.

Focusing on the geophysical component, our analysis accounts for approximately one-sixth of the geophysical variance, leaving the remaining five-sixths of the signal unexplained. It is quite certain that part of the missing signal would be explained by more accurate soil moisture models, which is consistent with the good performance of phase-driven soil moisture retrieval reported in the literature [11, 46]. A substantial part of the remaining signal appears to be associated with short-term and seasonal vegetation dynamics.

Our results provide a characterization of closure phase signatures across diverse geophysical settings, despite the limited spatial coverage of this study relative to global scales and the coarse classification of geophysical conditions. In low-coherence regions, such as vegetated mountainous areas, approximately 70% of the total variance in observed closure phases can be attributed to phase noise. In areas with seasonal vegetation, such as croplands, the relative contribution of soil moisture variation and vegetation phenology exhibit seasonal patterns. In other vegetated regions, vegetation-related signals become more pronounced during periods of rapid biomass development.

Question 3: *What are possible explanations for the unexplained signals in closure phases?*

To answer this question, we examined closure phase observations over agricultural

areas, where the annual mean closure phases display clear and consistent deviations from zero. Supported qualitatively by geophysical measurements, Sentinel-1 observations exhibit consistent positive closure phases throughout the crop development cycle in agricultural regions. The magnitude of these closure phases varies over the growth season, being clearly aligned with crop-growth rates. This analysis clearly points to the existence of a crop-development-related signature within the unexplained signal. To interpret the observed signatures, we proposed two potential mechanisms and developed corresponding conceptual models: one based on variations in the effective dielectric properties of the canopy, and the other on line-of-sight motion of the *scatterers* during vegetation development. These two new models provide plausible explanations for the observed positive closure phases. In addition, we extended the dielectric-based propagation model to a composite framework that integrates contributions from soil moisture variations and ground surface scattering, thereby improving the physical completeness of the model.

Our propagation model for vegetation is developed under the assumptions of an isotropic and linear medium to account for the modifications in electromagnetic wave propagation caused by crop canopy development. This equivalent-medium propagation model is able to relate temporal variations of biophysical parameters to closure phases and produce closure phases in comparable sign and magnitude to those observed in corn fields in southern Spain. Some disparities remain between modeled closure phases and observations in corn fields, indicating that the model remains incomplete.

The skewed-motion model established a connection between the distribution of the line-of-sight motion and closure phases within the framework of a small-motion approximation. Validation of the model is challenging without knowledge of the motion rate. While initially tailored for vegetation growth, this model is also applicable to scenarios involving random slow motion components with a skewed distribution, such as ice dynamics that produce skewed deformation within a resolution cell. In instances where the velocity is large, fast-evolving parts of plants are less likely to contribute to closure phases due to decorrelation.

By combining the dielectric variation contributions from both vegetation and soil, we introduce a composite model explicitly accounting for a three-layered medium that consists of vegetation, the ground surface, and subsurface soil. This model demonstrates that each layer contributes to non-zero closure phases and that multilayer interactions can generate additional phase responses with phase consistent individual layers. Unlike single-layer cases, where closure phase signs remain invariant under cyclic permutations of monotonic moisture variations, this property can be violated in multilayer configurations with large moisture differences. The predicted closure phase time series using in-situ measurements indicate that the dominant contribution varies with ground conditions, with the resulting closure phases governed by both the number of contributing layers and their relative scattering strengths. Furthermore, incorporating decorrelation modifies the effective phase center within each layer, thereby modifying the relative scattering contributions.

7.2. CONTRIBUTIONS

This research has provided the following contributions to the field:

- A statistical characterization of non-zero closure phases across wide spatiotemporal scales;
- A quantitative assessment of the explainable portion of non-zero closure phases based on current theoretical understanding;
- Identification of clear vegetation growth–related signals in Sentinel-1 data, providing strong evidence for a new physical interpretation of the geophysical origins of closure phases;
- Development of analytical closure phase models for vegetation growth, particularly incorporating the associated dielectric variation and skewed motion in the line-of-sight (LoS) direction, to interpret the geophysical origins of closure phases;
- Closure phase analysis tools, *Triplet* and *Triplet-plant*, featuring adaptive multi-looking methodologies that adapt to the spatial scale of the research area.

7.3. RECOMMENDATIONS

This study represents a journey of exploration, guided by the theme *in search of closure in InSAR closure phases*. Although not all questions related to this theme have been fully resolved, our findings open new opportunities for future research and provide a foundation upon which this work can be continued and expanded.

This study provides extensive analyses of non-zero closure phases, however, our current results do not yet support strong causal conclusions. Nevertheless, our findings point to a clear direction for future research: efforts should prioritize areas where closure phases are most significant and where extensive ground truth measurements of soil and vegetation parameters are available. Such areas are particularly valuable for elucidating the origins of closure phases, as high signal-to-noise ratio closure phase observations, together with the ground truth measurements, can help constrain and validate the underlying mechanisms.

For practical reasons, our study is limited to a one-year period. The seasonality observed in the statistics implies that the signal is non-stationary, which impairs some of the analysis performed. Considering longer time series in future studies would enable a more season-bond analysis. When working with longer time series, we also recommend constructing closure phases using different temporal baselines, which have the potential to reveal additional mechanisms underlying closure phase behavior, as different scattering processes may operate on different timescales.

The high prevalence of significant closure phases demonstrated in this dissertation emphasizes the importance of treating closure phases explicitly in SAR stack processing of distributed targets. However, tailored analyses should be conducted for individual applications, as the relevance and impact of closure phases may vary depending on the study context. For instance, in InSAR applications such as deformation analysis, the statistical properties of closure phases over longer temporal baselines are of particular

importance. Moreover, since the statistics of closure phases are affected by factors such as the wavelength of the SAR sensors [1, 11] and the degree of multilooking, a dedicated statistical analysis of closure phases should be conducted for each specific interferometric dataset to accurately quantify their impact on interferometric phase interpretation.

There is an opportunity for future research to explore the development of a unified model that integrates multiple contributing mechanisms, including dielectric variation, scattering processes, and line-of-sight (LoS) motion, to achieve a more comprehensive representation of the mechanisms underlying observed closure phases. At the same time, the inherent limitations of purely physical models, stemming from necessary simplifications, should be acknowledged. Rather than aiming for complete realism, these models should be used primarily as tools for geophysical interpretation and for identifying system sensitivities. For inversion applications, it is therefore recommended to adopt parametric modeling approaches that balance physical interpretability with practical robustness.

We are not yet able to quantitatively exploit the full observed signal. On the one hand, Sentinel-1-derived closure phases in agricultural regions are inherently noisy, requiring us to work at relatively low product resolution, which also limits the scope of how the closure phases can be investigated and exploited. This limitation is expected to be mitigated with higher-resolution SAR systems operating at different frequency bands, such as NISAR, and missions offering tomographic capabilities, such as Biomass, which will enable the investigation of scattering contributions from different canopy layers and subsurface depths. On the other hand, further development of the model requires extensive ground-truth data and, ideally, dedicated experiments. Tower-based tomographic experiments, such as the BorealScat campaigns, which provide radar observations across multiple frequencies alongside detailed meteorological and vegetation parameter measurements, will be valuable for characterizing and quantifying the relationship between closure phases and bio-geophysical variations across timescales ranging from seconds to years.

ACKNOWLEDGEMENTS

Since I began my Ph.D., I have often found myself thinking about what I would one day write in these acknowledgements. Whenever a thought, a memory, or a moment of gratitude came to me, I would write it down. And now, at last, the time has come to gather all those scattered thoughts and memories together.

Dear Shifu, Paco, you have been my hero throughout these years. When I had just started my Ph.D., you once asked me, "What do you like most about the Netherlands?" Without thinking, I answered, "You." Honestly, that answer wavered a little over the years, when work and life became crowded with stressful things, sometimes even soaked in tears. But in the end, it remains unchanged. After almost a decade of working with you, beginning with my master's thesis, I am still enjoying this journey and still learning from you every day, mostly about science, but also about life. You often say that it is unfortunate that I did my Ph.D. with you, because with our similar personalities, I may have learned less than I would have from someone very different from me. I would say that even if it was a mistake, I have made it a wonderfully enjoyable one. I love our scientific journey, from the ocean to land, back to the ocean, and, soon, to glaciers. Thank you for always being willing to explore the unknown together with me. I am deeply grateful for the freedom you have given me to explore the SAR world, and for all the opportunities you have opened up for me to learn, to wander, and to discover new things. Whenever I began to doubt myself, you were always there to give me the affirmation I needed. Your words have given me some of the greatest courage to gather myself, stand back up, and keep going. More than a supervisor, you have been a constant source of trust, encouragement, and inspiration. In China, we have a saying that a *Shifu* is a father figure for life. Thank you for being the best Shifu I could have asked for.

Dear Ramon, thank you for always showing such great interest in my research and for helping promote my work within the InSAR community. I still remember my very first radar group meeting presentation, when you introduced my work through the Fibonacci sequence. I was deeply impressed by the way you connected complex ideas to simple concepts, making the science accessible to an audience with diverse backgrounds. I learned a great deal from that experience, and it has shaped the way I think about scientific communication and presentations. Dear Susan, I have to admit that I was a little intimidated when I first met you. Then, through many conversations and many questions from me about plants, I gradually got to know you better. I have always been amazed that whenever I sent you an email, you would reply almost immediately, always with thoughtful and detailed answers. Thank you for being so generous with your knowledge and your time.

Dear Francesco, I started my journey by reading your papers on phase inconsistency over and over again, trying to put my hands on the work without any background in InSAR. Over the years, I have returned to them every now and then, and each time I find some detail that I had missed before. Thank you for inspiring me through your papers,

and also through our conversations about the interpretation of closure phase signals. Thank you also for being real, and for being willing to share with me your opinions about the topic and about people. I have always appreciated that openness, and I am grateful for all the conversations we have had along the way. Dear Lars, when I wanted to explore the TomoSAR data, you generously offered your help, together with the amazing technician Albert. I had so much fun playing with the data and reading through the BorealScat reports, and, of course, I had a wonderful time in Göteborg for the BorealScat workshop. I was also deeply impressed by the amazing team across Sweden working together on the tower campaign. Although, given the limited time and the scope of this study, it was difficult to bring the results together into a publication, I truly hope we will have the chance to play science together again in the future. Dear Juanma, I got to know you through an attempt to look at the HydroSoil campaign data. Thank you for always being so kind to me, and for all the constructive advice, encouragement, and compliments you have given me along the way. Muchas gracias! Dear Andy, although we have not had many interactions through work, I still remember that you came to my very first presentation at LPS and told me that I was brave to present something that did not work. Four years and a lot of work later, I looked back at that work again, and I think I can now say that I have made some good progress. I am really glad to have you on my committee and to be able to share this follow-up work with you. I hope you will like it a little more than you did in 2022.

Dear Marcel, I have always thought of you as my big brother, even though you were always taking my candies and cookies. You are my first friend in this country, and I actually started my radar journey with you. It was such a great pleasure to have you as my co-supervisor during my master's thesis and to continue discussing my Ph.D. work with you afterwards. Your passion for science and for Spain led me to my first publication, and I will always be grateful for that. Thank you very much for everything over all these years, and for being there from the very beginning of this journey. I cannot forget to mention Andreas and Owen whenever I talk about my radar family. Andreas, having almost completely opposite personalities, I am amazed that we still get along so well. I feel really proud to have you as my friend, especially when you are always there to help me fix my computer and remember my passwords. Thank you for being so tolerant of me most of the time. Owen, although you are younger than me, you always manage to inspire me with your simple words whenever I come to you for advice. Thank you for listening to me, for knowing when to take me away before I became aggressive towards others, and for standing beside me on the big day as my paranymph. Thank you both for always being there whenever I needed support.

Dear Philip, my first friend and first collaborator during my Ph.D., my paranymph, my conference travel partner, and my best friend. I am so glad to have you as my bestie, and to share the mutual understanding that we would never leave each other behind, whether the days bring fun or hard times. I always miss your "let me break this down for you" whenever you are away. Thank you for being my friend through it all, all the time I spend with you is basically amazing. Julia, my sister, my comfort zone in this foreign country. This short page is nowhere near enough to express all my love for you. Thank you for reminding me, whenever I feel lost, that I am my own anchor.

Dear Simon, you have always been so willing to lend a hand whenever I needed help

with my work. Thank you very much for doing me the great favor of helping with data processing and with my Dutch. Dear Ale and Benny, although I am always annoyed by you when we are all together, I cannot stop missing our trips every now and then. Thank you for all the homemade pasta, risotto, and tiramisu, and all the laughter and long hugs during the hard times. Dear Shafi, I never thought that you would become my first foreign friend to come with me to my hometown for Chinese New Year. It was such a wonderful time together! Thank you for being so flexible when we traveled together, and also for all your timely help when I was learning Dutch. Dear Dita, my occasional roommate, thank you for all the trips we took together and for sharing so much of your wisdom with me about dealing with people. Dear Mahmoud, thank you so much for all the time we spent together in the gym. You are such a kind and generous person. Thank you for helping me build a healthier lifestyle by going to the gym and by eating clean. Dear Daan, thank you for your timely hugs and support whenever I was struggling with my workstation and sinking into sorrow. And thank you also for helping me keep the candies away from me.

My dear Spanish gang, muchas gracias! Arturo, thank you for always being honest, patient, and generous with me, even when I keep annoying you with my long text messages and dragging you around Spain. I am always happy when you are around. Lucas, cycling with you in search of white kangaroos has always been so much fun! Thank you for always being available whenever I want to do sports together, and also for introducing me to the sweet Zuska! Carlos, thank you for all the serious conversations and the terrible jokes. Thank you for trusting me and for sharing your doubts with me when you have them at work.

鱼鱼，白白，雨晴，卷卷，殷宝，陈宝。感谢这些年来，我们一起度过的时光，一起经历的冒险，一起翻山越岭、追逐过的星星。感谢你们陪伴我一路成长，也感谢你们始终肯定着那个不断成长的我，更感谢你们总是愿意陪我去做那些我想做的事情。最要感谢的是你们总能让身在异国他乡的我感受到家的温暖。山水一程，三生有幸。愿我们前程似锦，友谊地久天长。

I would also like to thank those who were once close to me, but with whom I may no longer keep in touch, or whose stories with me may have ended with a sour taste. A part of me changed because of you, and that part has stayed with me as I continue my journey through life. Thank you for helping me understand who I am, define my boundaries, and realise how much I value integrity and sincerity in building connections with people. Thank you for the beautiful memories that continue to nourish me, and also for the painful ones that have become lessons I carry with me, helping me avoid stepping into the same mud again in the future.

感谢我的爸爸妈妈，感谢你们给我坚定的支持和绝对的自由，让我去追求自己想要的人生。感谢爸爸从小就告诉我，我唯一的敌人就是我自己，让我在遇到困难时不会轻易退缩。感谢妈妈教会我如何成为一个独立的人，肯定自己的价值，也学会享受人生每个阶段的美好。感谢我的哥哥，虽然你不善于表达，却一直让我感受到被爱，也一直是我最坚强的后盾。感谢你从小到大对我的保护，以及始终坚定地支持我去做让自己快乐的事情。感谢我的嫂子，从认识你开始，你就一直给予我无微不至的关怀，也渐渐成为了如今可以无话不谈的人。感谢你和哥哥，在我远离家乡的时候照顾好全家，让我可以无后顾之忧地继续向前走。感谢我的家人们，在我每一次难过、觉得坚持不下去的时候，你们总是告诉我：“没事，大不了你就回

来。”正是这样毫无条件的支持，给了我继续走下去的勇气。感谢我的侄子们，晨晨和嘉一。能够陪伴你们成长，让我觉得无比幸福。我总能在你们身上看到自己的影子，也从你们身上学着如何成为一个更好的榜样。即使我们不能经常见面，每次见面时紧紧的拥抱，依然总能让我觉得心都融化了。希望你们健康快乐地长大，也希望在未来的某一天，你们都能找到自己真正热爱、也愿意为之奋斗的事情。

In the end, I would like to thank all the people who, during the gloomiest times of my life, lit a light for me. Thank you to all those who saw my imperfections and still chose to love me. Thank you to all those whom I once regarded as my heroes, and who helped me become my own. I also want to thank myself. Thank you for always being ready for adventures, for keeping going through the difficult times, and for making it all the way here. This is the end of my Ph.D., but also the bright beginning of a new chapter. As I step into this new journey and face all the uncertainties that lie ahead, may I always remember the words of Alfred Tennyson in Ulysses: “To strive, to seek, to find, and not to yield.”

Dear readers, thank you for your patience and for taking the time to read these acknowledgements. Many names are mentioned in this tiny piece of the mosaic of my life, and many more are not, though they are no less important in other pieces of it. Getting along with people is a learning process, and all the people we meet and all the things we experience shape who we become. I am not sure what more I can tell you about them, or whether I am telling the story of my scientific career or simply the story of my twenties. Perhaps it is a little bit of both. The last thing I want to say is that the world is just one big amusement park. I wish you all a lot of fun.

Yan Yuan
Delft, August 2026

BIBLIOGRAPHY

[1] Francesco De Zan, Mariantonietta Zonno, and Paco Lopez-Dekker. "Phase inconsistencies and multiple scattering in SAR interferometry". In: *IEEE Transactions on Geoscience and Remote Sensing* 53.12 (2015), pp. 6608–6616.

[2] Francesco De Zan et al. "A SAR interferometric model for soil moisture". In: *IEEE Transactions on Geoscience and Remote Sensing* 52.1 (2013), pp. 418–425.

[3] Francesco De Zan et al. "Comments on "Influence of the Statistical Properties of Phase and Intensity on Closure Phase"". In: *IEEE Transactions on Geoscience and Remote Sensing* 59.7 (2020), pp. 6277–6278.

[4] Yusuf Eshqi Molan and Zhong Lu. "Can InSAR coherence and closure phase be used to estimate soil moisture changes?" In: *Remote Sensing* 12.9 (2020), p. 1511.

[5] Yujie Zheng et al. "On closure phase and systematic bias in multilooked SAR interferometry". In: *IEEE Transactions on Geoscience and Remote Sensing* 60 (2022), pp. 1–11.

[6] Simon Zwieback et al. "A statistical test of phase closure to detect influences on DInSAR deformation estimates besides displacements and decorrelation noise: Two case studies in high-latitude regions". In: *IEEE Transactions on Geoscience and Remote Sensing* 54.9 (2016), pp. 5588–5601.

[7] Simon Zwieback, Scott Hensley, and Irena Hajnsek. "Assessment of soil moisture effects on L-band radar interferometry". In: *Remote Sensing of Environment* 164 (2015), pp. 77–89.

[8] Francesco De Zan, Paloma Saporta, and Giorgio Gomba. "Spatiotemporal analysis of C-band interferometric phase anomalies over Sicily". In: *EUSAR 2022; 14th European Conference on Synthetic Aperture Radar*. VDE. 2022, pp. 1–4.

[9] Homa Ansari, Francesco De Zan, and Alessandro Parizzi. "Study of systematic bias in measuring surface deformation with SAR interferometry". In: *IEEE Transactions on Geoscience and Remote Sensing* 59.2 (2020), pp. 1285–1301.

[10] Francesco Falabella and Antonio Pepe. "On the Phase Nonclosure of Multilook SAR Interferogram Triplets." In: *IEEE Transactions on Geoscience and Remote Sensing* 60 (2022), pp. 1–17.

[11] Francesco De Zan and Giorgio Gomba. "Vegetation and soil moisture inversion from SAR closure phases: First experiments and results". In: *Remote Sensing of Environment* 217 (2018), pp. 562–572.

[12] Simon Zwieback, Scott Hensley, and Irena Hajnsek. "A polarimetric first-order model of soil moisture effects on the DInSAR coherence". In: *Remote Sensing* 7.6 (2015), pp. 7571–7596.

[13] Charles Elachi. “Spaceborne imaging radar: geologic and oceanographic applications”. In: *Science* 209.4461 (1980), pp. 1073–1082.

[14] Charles Elachi et al. “Spaceborne synthetic-aperture imaging radars: Applications, techniques, and technology”. In: *Proceedings of the IEEE* 70.10 (1982), pp. 1174–1209.

[15] Guang Zheng and L Monika Moskal. “Retrieving leaf area index (LAI) using remote sensing: theories, methods and sensors”. In: *Sensors* 9.4 (2009), pp. 2719–2745.

[16] Armin W Doerry. “Atmospheric loss considerations for synthetic aperture radar design and operation”. In: *Radar Sensor Technology VIII and Passive Millimeter-Wave Imaging Technology VII*. Vol. 5410. SPIE. 2004, pp. 17–27.

[17] Andreas Danklmayer et al. “Assessment of atmospheric propagation effects in SAR images”. In: *IEEE Transactions on Geoscience and Remote Sensing* 47.10 (2009), pp. 3507–3518.

[18] GH Born, JA Dunne, and DB Lame. “Seasat mission overview”. In: *Science* 204.4400 (1979), pp. 1405–1406.

[19] Shaun Quegan et al. “The European Space Agency BIOMASS mission: Measuring forest above-ground biomass from space”. In: *Remote Sensing of Environment* 227 (2019), pp. 44–60.

[20] Giorgio Franceschetti and Riccardo Lanari. *Synthetic aperture radar processing*. CRC press, 2018.

[21] Francesco De Zan and A Monti Guarnieri. “TOPSAR: Terrain observation by progressive scans”. In: *IEEE Transactions on Geoscience and Remote Sensing* 44.9 (2006), pp. 2352–2360.

[22] Roland Romeiser. “The future of SAR-based oceanography: High-resolution current measurements by along-track interferometry”. In: *Oceanography* 26.2 (2013), pp. 92–99.

[23] Ridha Touzi et al. “Coherence estimation for SAR imagery”. In: *IEEE Transactions on Geoscience and Remote Sensing* 37.1 (1999), pp. 135–149.

[24] DPS Bekaert et al. “Statistical comparison of InSAR tropospheric correction techniques”. In: *Remote Sensing of Environment* 170 (2015), pp. 40–47.

[25] Keya Desai et al. “Analysis of performance of flat earth phase removal methods”. In: *The International Archives of the Photogrammetry, Remote Sensing and Spatial Information Sciences* 42 (2018), pp. 207–209.

[26] Paul A Rosen et al. “Synthetic aperture radar interferometry”. In: *Proceedings of the IEEE* 88.3 (2000), pp. 333–382.

[27] Alessandro Parizzi and Ramon Brcic. “Adaptive InSAR stack multilooking exploiting amplitude statistics: A comparison between different techniques and practical results”. In: *IEEE Geoscience and Remote Sensing Letters* 8.3 (2010), pp. 441–445.

[28] Alberto Moreira et al. “A tutorial on synthetic aperture radar”. In: *IEEE Geoscience and Remote Sensing Magazine* 1.1 (2013), pp. 6–43.

[29] Curtis W Chen and Howard A Zebker. “Two-dimensional phase unwrapping with use of statistical models for cost functions in nonlinear optimization”. In: *Journal of the Optical Society of America A* 18.2 (2001), pp. 338–351.

[30] David Long and Fawwaz Ulaby. *Microwave radar and radiometric remote sensing*. Artech, 2015.

[31] Fabio Gatelli et al. “The wavenumber shift in SAR interferometry”. In: *IEEE Transactions on Geoscience and Remote Sensing* 32.4 (1994), pp. 855–865.

[32] Richard Bamler and Philipp Hartl. “Synthetic aperture radar interferometry”. In: *Inverse Problems* 14.4 (1998), R1.

[33] Alessandro Ferretti et al. *InSAR principles-guidelines for SAR interferometry processing and interpretation*. Vol. 19. 2007.

[34] Ulrich Steinbrecher et al. “TanDEM-X Mission: Overview, Current Situation and Future Prospects”. In: (2013).

[35] G Perrin, F Malbet, and JD Monnier. “Astrophysics with closure phases”. In: *European Astronomical Society Publications Series* 6 (2003), pp. 213–213.

[36] Yusuf Eshqi Molan, Zhong Lu, and Jin-Woo Kim. “Influence of the statistical properties of phase and intensity on closure phase”. In: *IEEE Transactions on Geoscience and Remote Sensing* 58.10 (2020), pp. 7346–7354.

[37] Francesco De Zan et al. “Letters Comments on“Influence of the Statistical Properties of Phase and Intensity on Closure Phase””. In: *IEEE Transactions on Geoscience and Remote Sensing* (2020).

[38] Andrew K Gabriel, Richard M Goldstein, and Howard A Zebker. “Mapping small elevation changes over large areas: Differential radar interferometry”. In: *Journal of Geophysical Research: Solid Earth* 94.B7 (1989), pp. 9183–9191.

[39] Simon Zwieback, Scott Hensley, and Irena Hajnsek. “Soil moisture estimation using differential radar interferometry: Toward separating soil moisture and displacements”. In: *IEEE Transactions on Geoscience and Remote Sensing* 55.9 (2017), pp. 5069–5083.

[40] Matt Nolan, Dennis R Fatland, and Larry Hinzman. “DInSAR measurement of soil moisture”. In: *IEEE Transactions on Geoscience and Remote Sensing* 41.12 (2003), pp. 2802–2813.

[41] Scott Hensley et al. “Effect of soil moisture on polarimetric-interferometric repeat pass observations by UAVSAR during 2010 Canadian soil moisture campaign”. In: *2011 IEEE International Geoscience and Remote Sensing Symposium*. IEEE. 2011, pp. 1063–1066.

[42] Keith Morrison et al. “Laboratory measurement of the DInSAR response to spatiotemporal variations in soil moisture”. In: *IEEE Transactions on Geoscience and Remote Sensing* 49.10 (2011), pp. 3815–3823.

[43] Bernhard Rabus, Hans Wehn, and Matt Nolan. “The importance of soil moisture and soil structure for InSAR phase and backscatter, as determined by FDTD modeling”. In: *IEEE Transactions on Geoscience and Remote Sensing* 48.5 (2010), pp. 2421–2429.

[44] Francesco De Zan, Alessandro Parizzi, and Pau Prats. “A proposal for a SAR interferometric model of soil moisture”. In: *2012 IEEE International Geoscience and Remote Sensing Symposium*. IEEE. 2012, pp. 630–633.

[45] Francesco De Zan. “An InSAR-based Soil Moisture Product for Arid Regions”. In: *EGU General Assembly Conference Abstracts*. 2023, EGU–6773.

[46] Francesco De Zan. “InSAR contributions to water status retrieval”. In: *EUSAR 2024; 15th European Conference on Synthetic Aperture Radar*. VDE. 2024, pp. 15–17.

[47] Marcel Buchhorn et al. “Copernicus Global Land Service: Land Cover 100m: Version 3 Globe 2015-2019: Product User Manual”. In: (2020).

[48] Murray C Peel, Brian L Finlayson, and Thomas A McMahon. “Updated world map of the Köppen-Geiger climate classification”. In: *Hydrology and Earth System Sciences* 11.5 (2007), pp. 1633–1644.

[49] N-E Tsendbazar et al. “Copernicus global land service: land cover 100m: Version 3 Globe 2015-2019: validation report”. In: (2021).

[50] Martti T Hallikainen et al. “Microwave dielectric behavior of wet soil-part 1: Empirical models and experimental observations”. In: *IEEE Transactions on Geoscience and Remote Sensing* 1 (1985), pp. 25–34.

[51] J. (2019) Muñoz Sabater. *ERA5-Land hourly data from 1950 to present. Copernicus Climate Change Service (C3S) Climate Data Store (CDS)*. https://cds.climate.copernicus.eu/datasets/reanalysis-era5-land. Accessed on 15-02-2023.

[52] G Mulder et al. “RIPPL, a Python-based InSAR stack and tropospheric delay software package”. In: *Computers & Geosciences* (2025), p. 106069.

[53] Lorenzo Bruzzone et al. “An advanced system for the automatic classification of multitemporal SAR images”. In: *IEEE Transactions on Geoscience and Remote Sensing* 42.6 (2004), pp. 1321–1334.

[54] Sami Samiei Esfahany. “Exploitation of distributed scatterers in synthetic aperture radar interferometry”. PhD thesis. 2017.

[55] Visual Crossing. *Visual Crossing Weather*. https://www.visualcrossing.com/. Accessed on 30-06-2023.

[56] Aiguo Dai. “The diurnal cycle from observations and ERA5 in surface pressure, temperature, humidity, and winds”. In: *Climate Dynamics* 61.5 (2023), pp. 2965–2990.

[57] Dora Matzke et al. “Bayesian inference for correlations in the presence of measurement error and estimation uncertainty”. In: *Collabra: Psychology* 3.1 (2017), p. 25.

[58] Kimberly A Novick et al. “The increasing importance of atmospheric demand for ecosystem water and carbon fluxes”. In: *Nature Climate Change* 6.11 (2016), pp. 1023–1027.

[59] Drew S Lyons et al. “Soil moisture variation drives canopy water content dynamics across the western US”. In: *Remote Sensing of Environment* 253 (2021), p. 112233.

[60] Lei Xu et al. “In-situ and triple-collocation based evaluations of eight global root zone soil moisture products”. In: *Remote Sensing of Environment* 254 (2021), p. 112248.

[61] The Institute of Statistics and Cartography of Andalusia. *Sistema de Información Geográfica de Parcelas Agrícolas*. https://www.juntadeandalucia.es/. Accessed on 11-05-2023.

[62] U.S. Department of Agriculture. *USDA Foreign Agricultural Service*. https://fas.usda.gov/. Accessed on 31-08-2023.

[63] Gemma Clemente-Orta et al. “Planting period is the main factor for controlling maize rough dwarf disease”. In: *Scientific Reports* 11.1 (2021), p. 977.

[64] Jesus M Ortiz, Salvador Zaragoza, and Rafael Bono. “The major citrus cultivars in Spain”. In: *HortScience* 23.4 (1988), pp. 691–693.

[65] JP Syvertsen, ML Smith Jr, and JC Allen. “Growth rate and water relations of citrus leaf flushes”. In: *Annals of Botany* 47.1 (1981), pp. 97–105.

[66] C Ortiz and A Torregrosa. “Determining adequate vibration frequency, amplitude, and time for mechanical harvesting of fresh mandarins”. In: *Transactions of the ASABE* 56.1 (2013), pp. 15–22.

[67] Arturo Villarroya-Carpio, Juan M Lopez-Sanchez, and Marcus E Engdahl. “Sentinel-1 interferometric coherence as a vegetation index for agriculture”. In: *Remote Sensing of Environment* 280 (2022), p. 113208.

[68] Francisca López-Granados et al. “Spatial variability of agricultural soil parameters in southern Spain”. In: *Plant and Soil* 246 (2002), pp. 97–105.

[69] Fawwaz T Ulaby, Ahad Tavakoli, and BA Thomas. “Microwave propagation constant for a vegetation canopy with vertical stalks”. In: *IEEE Transactions on Geoscience and Remote Sensing* 6 (1987), pp. 714–725.

[70] Fawwaz T Ulaby and MOHAMED A El-Rayes. “Microwave dielectric spectrum of vegetation-Part II: Dual-dispersion model”. In: *IEEE Transactions on Geoscience and Remote Sensing* 5 (1987), pp. 550–557.

[71] Fawwaz T Ulaby et al. “Relating polaization phase difference of SAR signals to scene properties”. In: *IEEE Transactions on Geoscience and Remote Sensing* 1 (1987), pp. 83–92.

[72] Saeed Khabbazan et al. “The influence of surface canopy water on the relationship between L-band backscatter and biophysical variables in agricultural monitoring”. In: *Remote Sensing of Environment* 268 (2022), p. 112789.

[73] Fawwaz T Ulaby and RP Jedlicka. “Microwave dielectric properties of plant materials”. In: *IEEE Transactions on Geoscience and Remote Sensing* 4 (1984), pp. 406–415.

[74] Martin M Williams and John L Lindquist. “Influence of planting date and weed interference on sweet corn growth and development”. In: *Agronomy Journal* 99.4 (2007), pp. 1066–1072.

[75] Kun-Shan Chen et al. “Emission of rough surfaces calculated by the integral equation method with comparison to three-dimensional moment method simulations”. In: *IEEE Transactions on Geoscience and Remote Sensing* 41.1 (2003), pp. 90–101.

[76] EPW Attema and Fawwaz T Ulaby. “Vegetation modeled as a water cloud”. In: *Radio Science* 13.2 (1978), pp. 357–364.

[77] Alessandro Parizzi, Xiaoying Cong, and Michael Eineder. “First Results from Multi-frequency Interferometry. A comparison of different decorrelation time constants at L, C, and X Band”. In: *ESA Scientific Publications* SP-677 (2009), pp. 1–5.

[78] Narayanarao Bhogapurapu, Paul Siqueira, and John Armston. “A new InSAR temporal decorrelation model for seasonal vegetation change with dense time-series data”. In: *IEEE Geoscience and Remote Sensing Letters* 21 (2024), pp. 1–5.

[79] Davide Palmisano et al. “Coherent and incoherent change detection for soil moisture retrieval from Sentinel-1 data”. In: *IEEE Geoscience and Remote Sensing Letters* 19 (2022), pp. 1–5.

[80] Andrea Monti-Guarnieri et al. “Vegetated target decorrelation in SAR and interferometry: models, simulation, and performance evaluation”. In: *Remote Sensing* 12.16 (2020), p. 2545.

LIST OF PUBLICATIONS

PUBLISHED

1. **Y. Yuan**, M. Kleinherenbrink, and P. López-Dekker, 'On Crop Growth and InSAR Closure Phases,' IEEE Transactions on Geoscience and Remote Sensing, 2024.

2. **Y. Yuan**, and P. López-Dekker, 'Statitical Properties of Closure Phases in SAR Interferometry,' IEEE Transactions on Geoscience and Remote Sensing, 2026.

3. M. Kleinherenbrink, P. Conroy, A. Theodosiou, **Y. Yuan**, L. Gaultier, F. Collard, B. Chapron, B. Rommen, and P. López-Dekker, 'The Harmony scientific workbench part 1: Modeling high-resolution multistatic radar observations of the ocean,' IEEE Transactions on Geoscience and Remote Sensing, 2026.

4. P. Conroy, M. Kleinherenbrink, A. Theodosiou, **Y. Yuan**, L. Gaultier, F. Collard, B. Chapron, B. Rommen, and P. López-Dekker, 'The Harmony scientific workbench part 2: High-resolution ocean wind stress and surface current retrieval,' IEEE Transactions on Geoscience and Remote Sensing, 2026.

IN REVIEW

1. **Y. Yuan**, and P. López-Dekker, 'A Composite Model for InSAR Closure Phases,' IEEE Geoscience and Remote Sensing Letters, 2026.

